Science Advances
AAAS

This manuscript is under second review in Science Advances

Seafloor Geodesy Unveils Seismogenesis of Large Subduction Earthquakes in México

Short title: **Seismogenesis uncovered by seafloor geodesy**

Víctor M. Cruz-Atienza[1*], Josué Tago[2], Luis A. Domínguez[1], Vladimir Kostoglodov[1], Yoshihiro Ito[3], Efraín Ovando-Shelley[4], Tonatiuh Rodríguez-Nikl[5], Renata González[4], Sara Franco[1], Darío Solano-Rojas[2], Joel Beltrán-Gracia[2], Paulina Miranda-García[2], Frédérick Boudin[6], Luis Rivera[7], Anne Bécel[8], Carlos Villafuerte[1], Jorge Real[1], Ekaterina Kazachkina[1] and Arturo Ronquillo[9]

[1] Instituto de Geofísica, Universidad Nacional Autónoma de México, Mexico.
[2] Facultad de Ingeniería, Universidad Nacional Autónoma de México, Mexico.
[3] Disaster Prevention Research Institute, Kyoto University, Japan.
[4] Instituto de Ingeniería, Universidad Nacional Autónoma de México, Mexico.
[5] Department of Civil Engineering, California State University, Los Angeles, USA.
[6] Laboratoire de Géologie, École Normale Supérieur de Paris, France.
[7] Institut Terre et Environnement, Université de Strasbourg, France.
[8] Lamont Doherty Earth Observatory, Columbia University, USA.
[9] Instituto de Ciencias del Mar y Limnología, Universidad Nacional Autónoma de México, Mexico.

*Corresponding author: cruz@igeofisica.unam.mx

March, 2025

Abstract

Seafloor geodesy may lead to deep understanding of subduction systems and seismogenesis. Based on measurements of near-trench deformations of the oceanic and overriding plates, in this investigation we elucidate the tectonic and mechanical processes leading to the Mw7.0 Acapulco, Mexico, earthquake in 2021 at the heart of the Guerrero seismic gap. We exploit unprecedented ocean-bottom observations using new *ultra-long-period 'tilt mechanical amplifiers'*, along with hydrostatic pressure, GNSS, and satellite InSAR data. The joint inversion of all these geodetic data, template matching seismicity and repeating earthquakes, revealed the first two shallow slow slip events (SSEs) observed in Mexico. The first one migrated from the trench to the earthquake hypocenter before rupture, and the second one occurred following an Mw7.7 long-term deeper SSE induced by the earthquake. Near-trench oceanic-crust episodic deformations (i.e., tilt transients) associated with shallow and deep synchronous decoupling of the plate interface reveal the occurrence of *'slab-pull surges'* across the subduction channel prior to three M7+ regional earthquakes including the Acapulco event.

1. Introduction

Seafloor geodesy in subduction zones has gained remarkable importance in the last decade. Looking for transient deformations caused by tectonic processes such as slow slip events (SSE), several groups have instrumented the seafloor down to the oceanic trench. An emblematic case is the Eastern Japan and Nankai subduction zones, where the world's largest seafloor observatories, S-net and DONET, were deployed in the aftermath of the 2011 Tohoku-Oki megathrust earthquake[1]. Further efforts have been made in these [2] and other regions such as the Costa Rica [3], New Zealand [4], Mexico [5], Cascadia [6], Alaska [7] and Chile [8] margins to gain insight into the plate interface processes that generate large earthquakes and tsunamis.

The evidence of SSEs from seismological analysis is well documented and encompasses a wide range of slow earthquakes, from tectonic tremor to very-low-frequency events. Seismic records have yielded significant insights into the strain evolution in the megathrusts, both in the deep and shallow transition zones that flank the locked interface depths [9–16]. The migration and sensitivity of tremor sources are closely linked to overpressured fluids at the interface, which can vary in space and time depending on the amount of water embedded in subducted sediments, the oceanic crust, and the upper mantle [17–21]. The inherent heterogeneity of the plate contact and the irregularity of the interface result in the segmentation of seismic behavior along the megathrusts [22–24]. This is illustrated by the Guerrero subduction zone in south-central Mexico, which is the location of the world's largest SSEs [25,26] and a major seismic gap that has long been feared [27,28]. Should an earthquake with a magnitude greater than 8 break through the gap, the strong motions in Mexico City could be threefold those registered during the catastrophic 1985 Michoacán earthquake [29,30] , which resulted in the deaths of at least 10,000 people in the country's capital.

The potential for large earthquakes is closely related to the occurrence of SSEs [2,31–34]. Continuous monitoring of seafloor crustal deformations and seismicity using frontline observatories is a crucial step in the development of predictive models aimed at identifying potential locations and timing for future devastating earthquakes and tsunamis. The development of GPS-acoustic measurements of seafloor transponder arrays has a long history [35,36], leading to the advent of high-tech, lower-cost observational protocols employing autonomous devices such as wave gliders [37–39].

Nevertheless, understanding the tectonic processes occurring at time scales that are crucial for comprehending the short-term dynamics that precede major earthquakes remains elusive using these devices. Ocean bottom pressure (OBP) gauges (also referred to as absolute pressure gauges or APG) are more appropriate instruments and the most easily deployed and commonly used for measuring SSE-induced vertical deformations [2,4,6,40]. However, in addition to the intrinsic drift they suffer [41], these single-component sensors are so sensitive that both tidal and non-tidal oceanographic signals often mask tectonic deformation [6,42–44]. Long-base tiltmeters onshore [45] and borehole tiltmeters offshore [46,47] suffer similar problems where noise could potentially overwhelm these highly sensitive and costly devices.

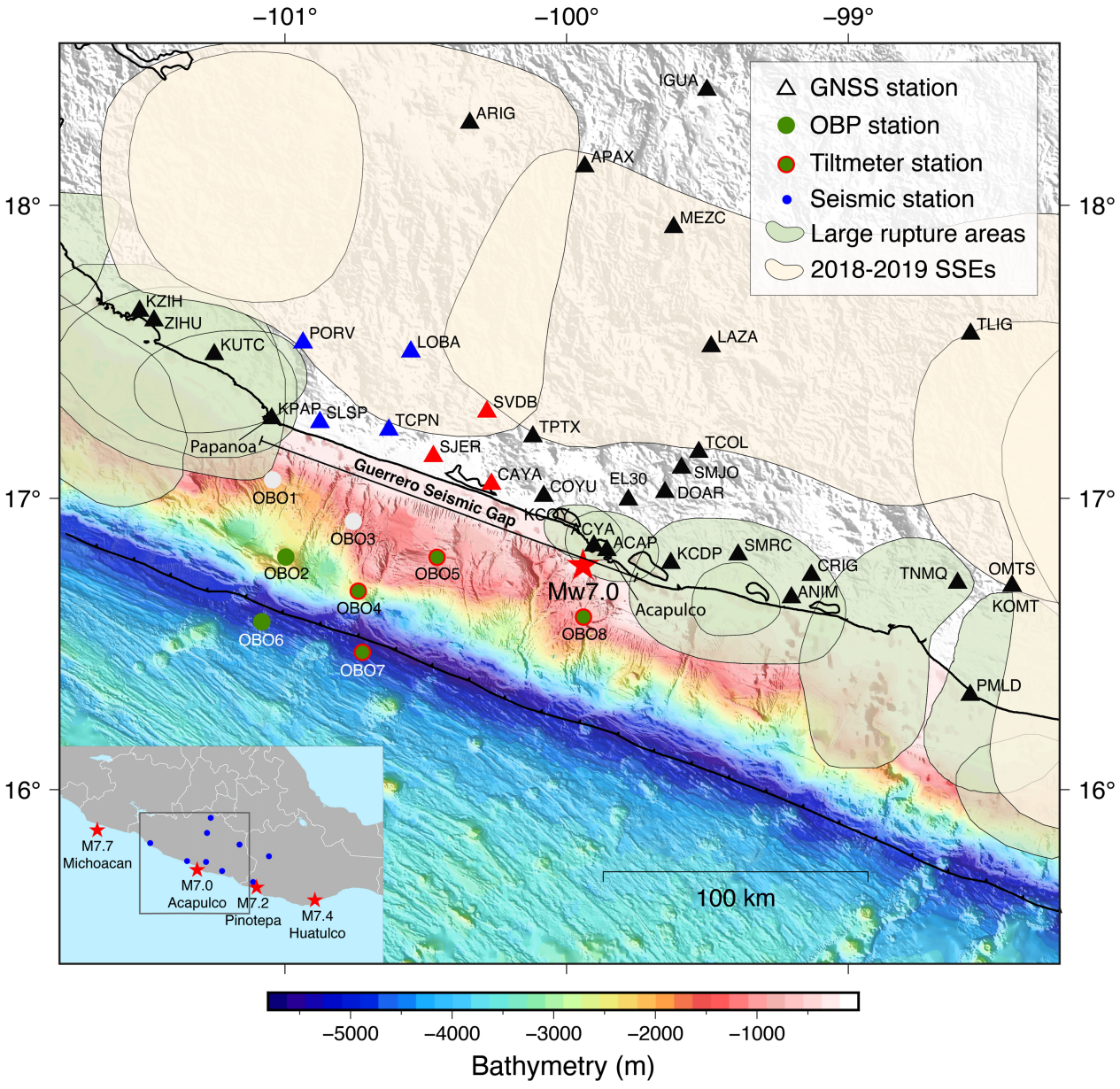

Figure 1 Geographical location of the geodetic and seismic stations used in this work. In addition, the epicenter of the 8 September 2021 Acapulco earthquake (red star), the high-resolution

bathymetry of the Guerrero seismic gap detached from subsequent campaigns, the rupture areas of the historical earthquakes and the most recent SSE of 2018 and 2019 prior to this research are also shown.

The present study investigates the seismogenesis of the Guerrero Seismic Gap (GGap) through an analysis of a comprehensive set of seafloor instruments and observations. These include newly developed low-cost, virtually noise-free ocean bottom tiltmeters (OBT) and OBP sensors with continuous records spanning 5.4 years, during which four M7+ regional earthquakes have occurred. These observations are complemented by measurements from a dense GNSS network and satellite interferometric SAR onshore. One of the tiltmeters was deployed over the incoming Cocos plate, situated only 10 km from the Middle America trench, while the remainder were distributed inside the gap on the overriding North American plate. All instruments, including broadband seismometers on land, recorded tectonic activity both before and after the 2021 Mw7.0 Acapulco earthquake [48,49]. Collectively, the data offer a distinctive perspective on the seismogenesis of this event and that of the other regional earthquakes. A scenario that could potentially shed light on the origin of future major ruptures in the seismic gap and other regions of the globe.

2. Results

In November 2017, we deployed the first Mexican seismogeodetic amphibious network across the GGap [5]. In addition to the onshore installation and/or maintenance of 34 GNSS stations and eight broadband seismometers in the state of Guerrero, 43 ocean bottom instruments (geodetic and seismic) were installed and maintained, and data were acquired until April 2024. This objective was achieved through eight oceanographic expeditions conducted aboard the R/V El Puma, operated by the National Autonomous University of Mexico (UNAM), in addition to an associated campaign undertaken in 2022 aboard the R/V Marcus G. Langseth, operated by Columbia University.

Except for one (OBO8 installed in March 2022), all other ocean bottom observatories (OBO) were installed in November 2017 between ~1,000 and 4,992 m depth (Fig. 1). The eight OBOs were equipped with a Digiquartz® pressure sensor (OBP) developed by Paroscientific Inc and a thermometer. Instruments OBO3, OBO4, OBO5, OBO7, and OBO8 correspond to Fetch units manufactured by Sonardyne Inc and were also equipped with a high-precision dual-axis digital tiltmeter (OBT) incorporated into a microelectromechanical device within the glass sphere, manufactured by Analog Devices Inc. These units had an acoustic transducer/transponder for data transmission and GPS-Acoustic measurements using a Waveglider in two instrument arrays at OBO4 and OBO5 sites [5]. OBO1 never responded one year after its deployment and OBO3 had a transmission failure, so no data are available from either site. Covering the whole period 2017-2024, the 34 GNSS stations were operational onshore either continuously or partially.

During the 5.4 years of continuous data acquisition, at least two previously documented M7+ SSEs occurred in Guerrero in 2018 and 2019 [33] and four M7+ thrust earthquakes happened in south-central Mexico (see Fig. 1 for event locations). Epicentral distances of the earthquakes to the seafloor stations ranged from 490 km for the 2020 Mw7.4 Huatulco earthquake to 55 km for the 2021 Mw7.0 Acapulco earthquake. This provides an exceptional opportunity to study the effects at the plate interface within the GGap caused by significant regional slow- and fast-slip events.

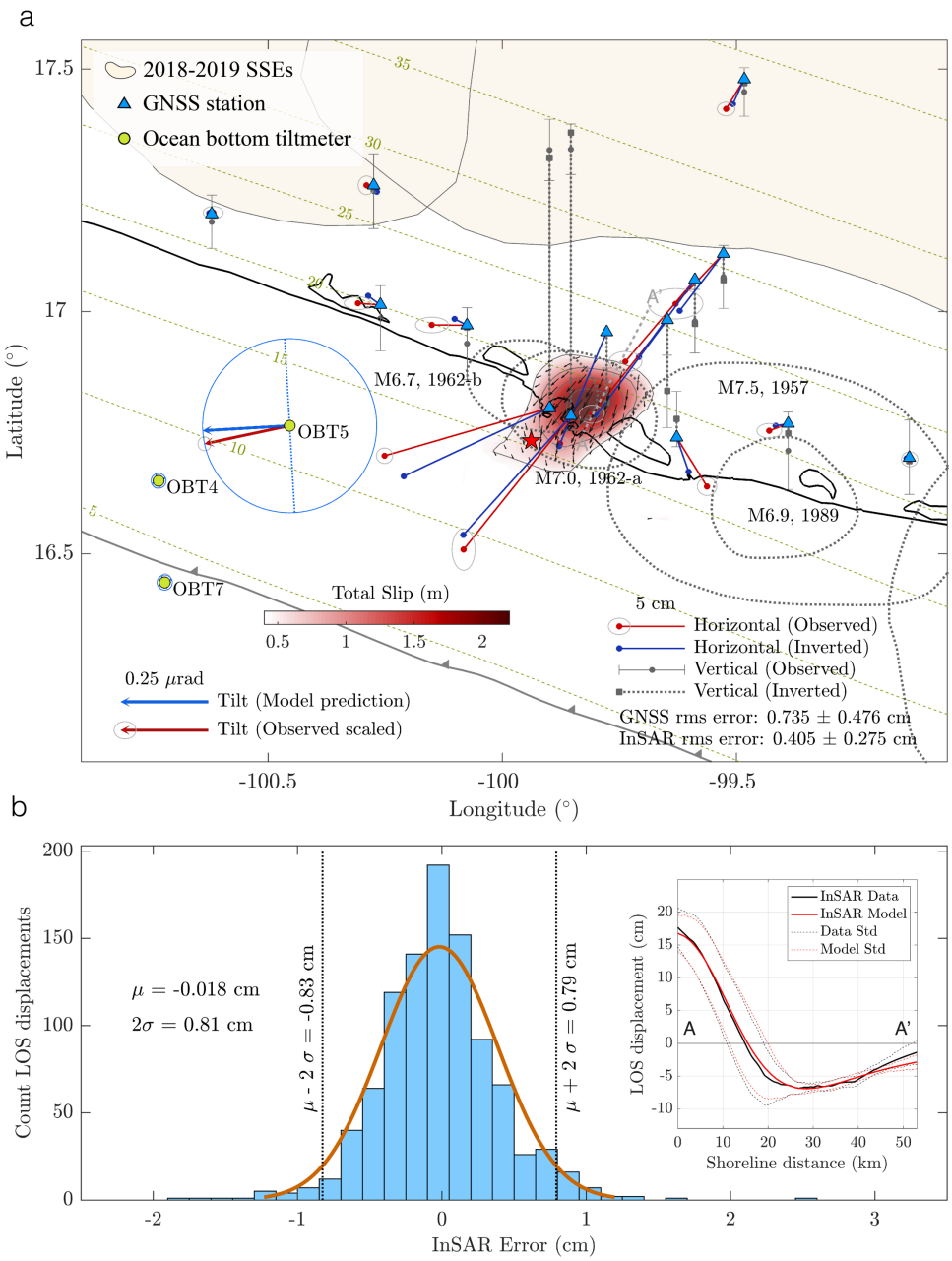

Figure 2 Joint co-seismic inversion of GNSS and InSAR data from the 8 September 2021 earthquake beneath Acapulco (Mw7.0). (a) Slip distribution accompanied by fit of displacements at GNSS stations, rupture areas of historical earthquakes, and comparison of model-associated theoretical tilt with observed tilt (scaled) at three ocean bottom tiltmeters. The blue circles and dotted lines represent the tilt amplitude and tilting axis, respectively. (b) Distribution of InSAR errors and average fit of observed data along the profile shown in (a) within a vicinity of 10 km around the profile (inset).

2.1. The Mw7.0 Acapulco earthquake

On September 8, 2021, an Mw7.0 thrust earthquake occurred beneath Acapulco right in the heart of the Guerrero seismic gap [48,49] (hereinafter "Acapulco earthquake"), with epicenter 55 km east of

station OBO5 (Fig. 1). Without a doubt, this earthquake is the best near-field ever recorded in Mexico both seismically and geodetically. Fig. 2 shows the co-seismic slip distribution derived from the joint inversion of 15 GNSS displacements, first used here (Figs. S1, S2 and S3b), and a saliency-based quad-tree-sampled Sentinel-satellite interferogram (Fig. S3) [50] by means of the ELADIN (ELastostatic ADjoint INversion) method [51,52]. Section 4.1 of Materials and Methods provide details about this inversion. The slip distribution features a main, well-localized asperity with maximum slip of 2.3 m located within the rupture area of the May 11, 1962 earthquake (see dotted ellipse on Fig. 2a), and confirms a northeast (i.e., downdip) rupture directivity from the hypocenter [48], located offshore about 20 km southwest of the asperity. This rupture is a repeat of the Mw7.0 1962 event [53] that was followed by a Mw6.7 doublet nine days later next to the Ms7.5 Acapulco-San Marcos rupture of 1957, which toppled the Angel of Independence emblematic monument at the country's capital, and gave birth to earthquake engineering in Mexico.

The Guerrero gap is well known for its large SSEs that may propagate to shallow, seismogenic depths between Acapulco (100°W) and Papanoa (101°W) [25,33,51] (Fig. 1). This 130-km-long segment defines the oldest part of the seismic gap, where the last M7+ rupture took place 113 years ago, on December 16, 1911 (Ms7.6) [28]. Thus, the 2021 Acapulco earthquake occurred where the gap extends southeastward in a 110-km-long segment that hosted the Ms7.5 Acapulco-San Marcos earthquake 67 years ago, on July 28, 1957 (Fig. 2a). It is known that SSEs can play an important role in the initiation of large ruptures [2,31–34] and the recent record from Mexico shows that the last four M7+ thrust earthquakes preceding the 2021 Acapulco event in the states of Guerrero and Oaxaca were triggered, or at least preceded, by an SSE downdip from and near their hypocenters. These events include the Mw7.5 2012 Ometepec [54], the Mw7.3 2014 Papanoa [34], the Mw7.2 2018 Pinotepa [33] and the Mw7.4 2020 Huatulco [52] earthquakes. Whether a similar phenomenon happened in the Acapulco rupture is one of the questions we will explore below, using unprecedented data.

2.2. Transient forearc deformation: offshore and onshore data

Available hydrostatic pressure records until March 2023 with a sampling rate of 30 minutes are shown in Fig. 3a along with the timing of the SSEs in Guerrero mentioned earlier and the M7+ thrust earthquakes in south-central Mexico (see Fig. 1 for event locations). An effective way to reduce noise associated with tidal and non-tidal oceanographic components is correcting pressure from collocated temperatures, which are often correlated at sites lying on the continental shelf (Fig. S7) [43]. Common noise across the station array associated with long-wavelength signals can also be reduced by subtracting a reference site minimally affected by the tectonic effects under study [2,4]. Section 4.2 of Materials and Methods provide details of the noise reduction procedure we applied.

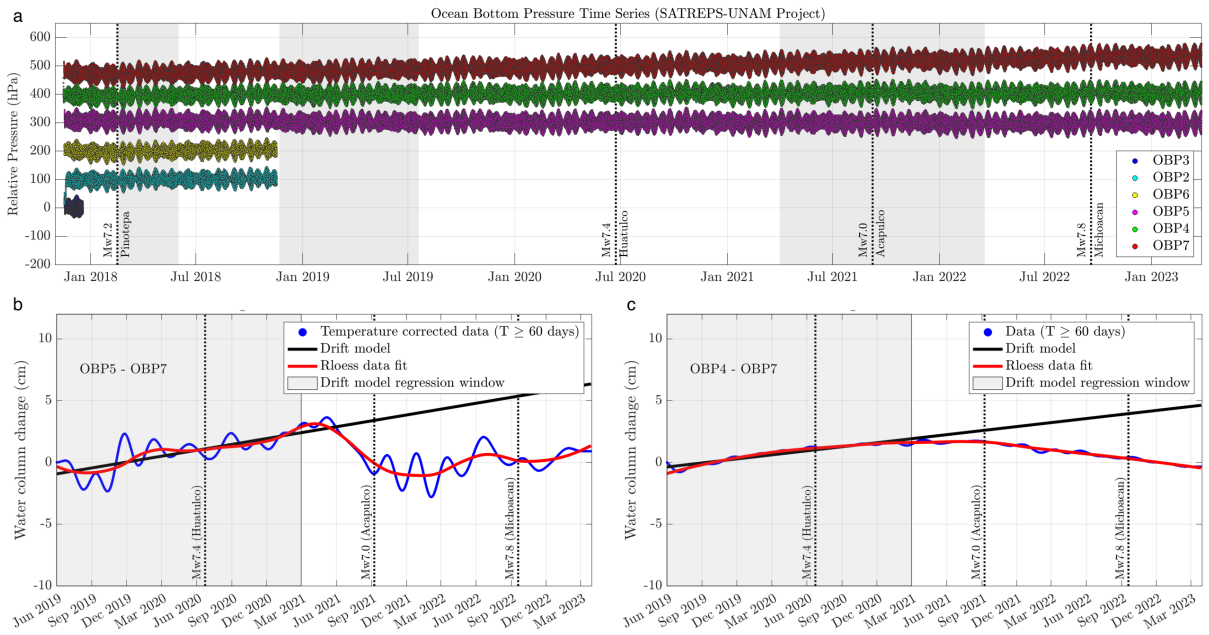

Figure 3 Continuous hydrostatic pressure records at ocean bottom pressure (OBP) stations for 5.4 years. (a) Raw data along with timing of significant regional earthquakes (dotted lines) and duration of deep SSE in the Guerrero gap (grey shaded). (b and c) Temperature-corrected seafloor pressures at OBT5 and OBT4 relative to OBT7 (Cocos Plate) in the period surrounding the Acapulco earthquake. The gray shades depict the regression window to fit the drift model (black lines).

Inspection of the temperature-corrected pressure at OBP5 relative to the Cocos plate (Fig. 3b) (i.e., relative to OBP7) reveals that three months before the 2021 Acapulco earthquake, the water column began shrinking to about 3 cm at the time of the earthquake. Also remarkable is the permanent deviation of pressure from the drift model during the year and a half following the event. Although uncertain because the linear drift model does not fully capture the data in the regression window, the relative water column at OBP4, the site closest to the trench in the overriding North American plate, may also have decreased by approximately 1 cm (Fig. 3c). Since (1) pressure evolution at both sites relative to the same reference (OBP7) are substantially different and (2) the pressure time series at OBP4 and OBP7 are very similar to each other (Fig. S7c), then the prominent pressure drop in OBP5 responds to a local phenomenon producing a progressive seafloor lifting during the three months preceding the earthquake. This is our first evidence pointing to the occurrence of an SSE somewhere below the seafloor in that period. OBP5 is about 30 km from the coast, therefore, we analyzed its closest GNSS time series as follows.

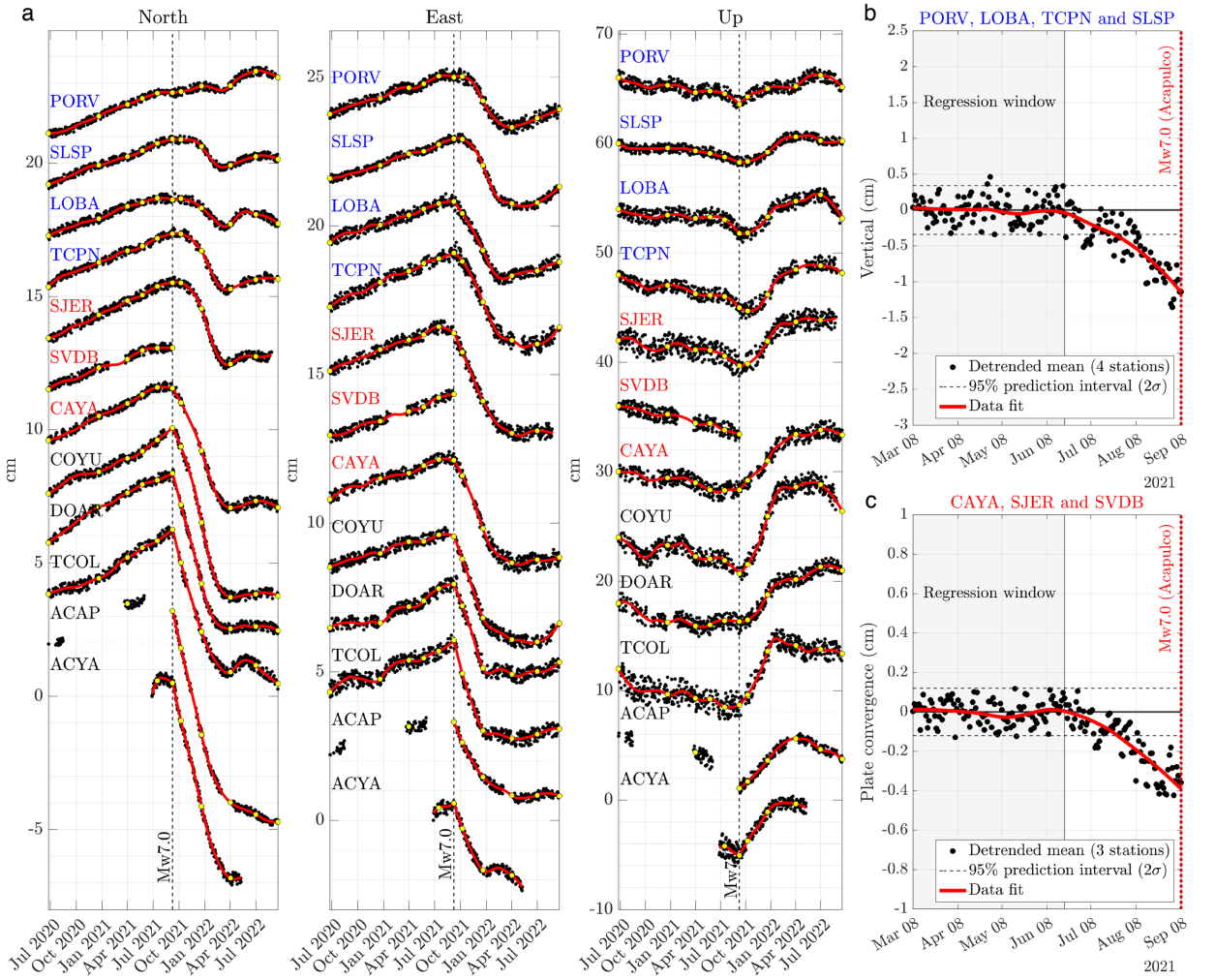

Figure 4 GNSS displacement time series surrounding the Acapulco earthquake after outlier and seasonal noise reduction. (a) Yellow dots indicate the bounding dates of the inverted time windows. Blue and red fonts are associated with panels (b) and (c), respectively (and color-coded stations in Fig. 1). (b) Average detrended vertical displacements at sites marked with blue fonts. (c) Average detrended displacements parallel to the plate convergence direction at sites marked with red fonts. The gray shades in (b) and (c) depict the regression windows used for detraining the signals.

Onshore, seasonal noise-reduced displacements [52] (Fig. S9) in four GNSS sites approximately 60 km northwest of OBP5 indicate that, during the same three-month period preceding the earthquake, the coastal subsidence rate characteristic of interseismic periods in Guerrero was prominently increased (blue sites in Figs. 1 and 4a). This can be better appreciated in the detrended mean of the vertical components (Fig. 4b) and possibly related to a slip transient updip in the plate interface (possibly an offshore SSE). Although the mean horizontal displacements along the plate-convergence direction shows no significant rate change prior to the Acapulco earthquake (not shown), it does at the three closest GNSS sites about 30 km north-northeast of OBP5 (red sites, Figs. 1 and 4c). A visual inspection of the north and east components at these sites (Fig. 4a) reveals

that such rate change corresponds to a slowdown of the interseismic deformation during the three months prior to the earthquake. At CAYA station, the closest site to OBP5, the vertical displacement rate tends to changed its polarity from subsidence to incipient uplift in the same period that OBP5 experienced the uplift referred to above (Figs. 4a and 3b). Selected GNSS displacements in Fig. 4a also show the large post-seismic release during the nine months following the earthquake which as we shall see, primarily correspond to a large, long-term SSE induced by the rupture.

2.3. Ocean bottom ultra-long-period Tilt Mechanical Amplifiers

Non-harmonic noise could dominate the bandwidth of interest in ocean bottom tiltmeters and pressure gauges data. Non-tidal oceanographic fluctuations of the water column can seriously obscure the information [42–44,46,47]. This indicate that the stillness of the deep ocean and the extreme sensitivity of some geophysical instruments do not necessarily facilitate the detection of tectonic deformation. An alternative to alleviate this problem might come from noise-insensitive devices that amplify potentially useful signals over a known bandwidth. As demonstrated below, low-cost tiltmeters housed within a glass sphere mounted on a steel tripod over highly compressible marine sediments act as ultra-long-period tilt mechanical amplifiers (TMA) that see slow tectonic deformations and are blind to most oceanographic noise.

Ocean bottom Fetch units OBO4, OBO5, OBO7 and OBO8 (Fig. 1) are equipped with two-component high-precision tiltmeters within a glass sphere that are mainly designed for unit control. According to the manufacturer, the sensitivity of these sensors is 436 μrad, so at first sight, they should be blind to expected secular or transient tectonic deformations on the order of units of microradian per year[45,46]. As a proof of concept to assess whether the TMAs could detect tectonic deformations, we will develop a simplified, two-dimensional model under conditions close to those expected in our ocean bottom instruments.

Neglecting any possible oceanographic effects, the instrument tilt depends on (1) the tectonic tilt (i.e. the hard-rock basement tilt) and (2) the response of the highly compressible fluid-saturated seafloor sediments to the differential forces applied by the instrument legs as the basement tilts (Fig. 5a). The problem thus reduces to estimating these forces for a given basement tilt and then quantifying the differential settlements of the sediments surrounding each leg. With these elements, the effective instrument tilt can be estimated and compared to the basement tilt. The detailed model description to address this problem in found in Section 4.3 of Materials and Methods.

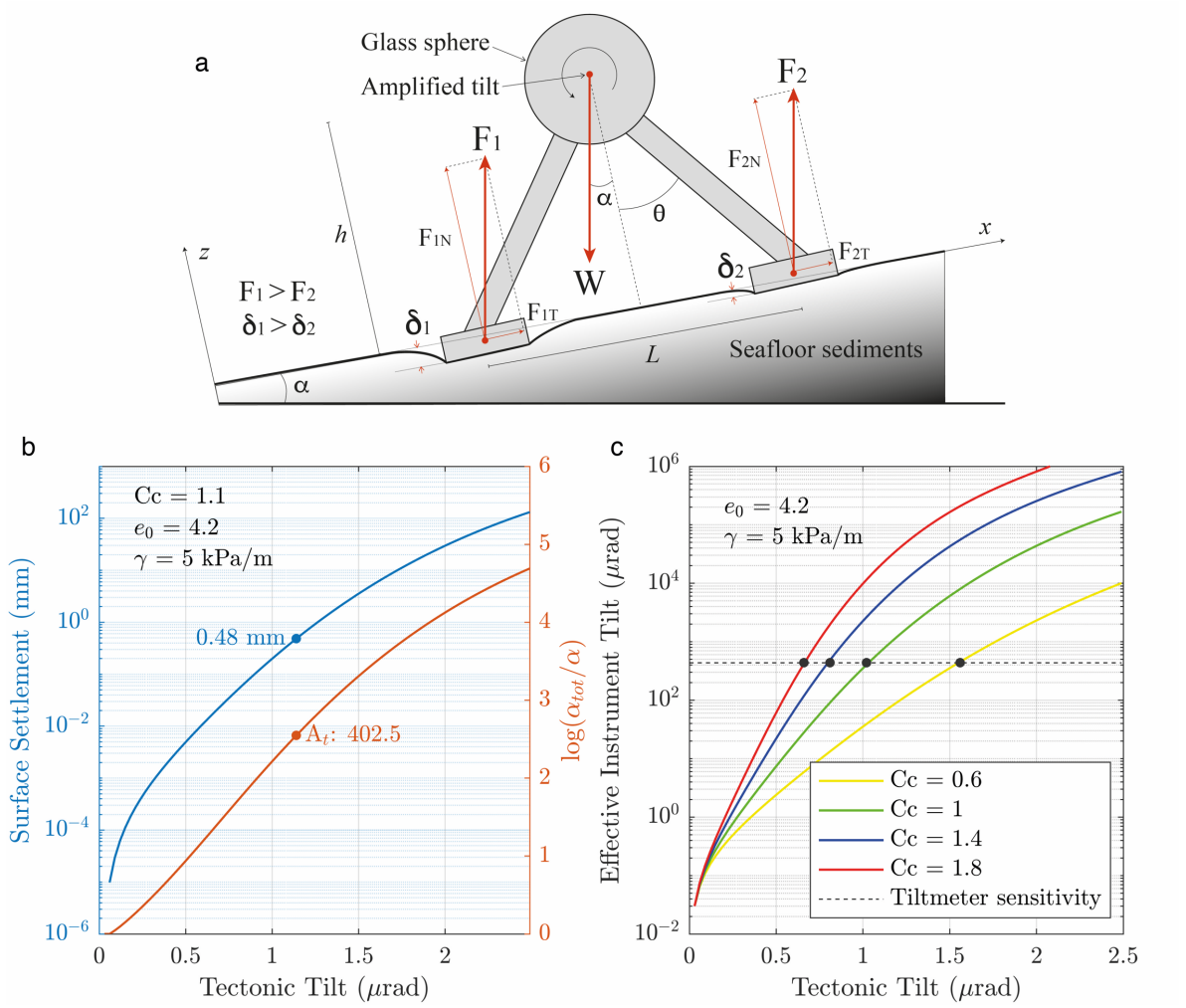

Figure 5 Performance of an Ultra-Long-Period Tilt Mechanical Amplifier (TMA). (a) Simplified body diagram of a Fetch unit upon highly compressible seafloor sediments after a basement tilt α. (b) Sediment settlement (left axis) and tilt amplification (right axis) as a function of basement tilt incorporating the highly non-linear sediments response to the differential Fetch-unit leg forces. Dots indicate when tilt amplification reaches the instrument sensitivity threshold for the given sediment properties, where Cc stands for the compressibility index, e_0 for the void ratio and γ for the effective stress gradient. (c) Effective instrument tilt within the glass sphere as a function of basement tilt for different sediment compressibility (Cc).

From our model, we can thus distinguish between α, the slow tectonic (basement) tilt, and α_s, the settlement-induced tilt due to the differential settlements underneath the unit legs (because $\delta_1 > \delta_2$, Fig. 5a). The effective (or total) instrument tilt, which is the observable measured by the tiltmeter within the glass sphere, is then given by $\alpha_{tot} = \alpha + \alpha_s$, and we define $A_t = \alpha_{tot}/\alpha$ as the tilt amplification factor that we expect to be larger than one.

Fig. 5b shows the evolution of α_{tot} as α increase linearly from 0 to 2.5 μrad. The simulation results are shown in terms of the settlement at the surface (left axis) and A_t (right axis), both as a function of α, for the indicated typical values of sediment compressibility index, C_c, void ratio, e_0, and

effective stress gradient, γ. The blue and orange dots correspond to the values of each function when α_{tot} exceeds the tiltmeter sensitivity threshold of 436 μrad. At that moment, sediments under leg 1 have settled 0.48 mm and α has been amplified 402.5 times. It is also clear that settlement and thus tilt amplification grow exponentially with α. However, we will see later that since the expected transient change of the actual tectonic tilt is within ~0.5 μrad, the variation of the amplification factor in that range should not exceed one order of magnitude. Fig. 5c and S11c show the evolution of α_{tot} and δ as the basement tilts, respectively, for a wide range of compressibility indexes covering most of the values determined for marine sediments [57,58], as illustrated in Fig. S11d. The black dots indicate again the moments when α_{tot} overcomes the tiltmeter sensitivity threshold. Given the chosen values for e_0 and γ, the instrument threshold is reached in all instances for tectonic tilts smaller than about 1.5 μrad. The black curve of Fig. S11d depicts the α values reaching the instrument sensitivity as a function of C_c for the chosen conservative parameters and a compressibility range for different types of marine sediments after Davie et al.[57] and Hampton[58].

Base on this analysis, we conclude that Fetch units act as seafloor TMAs that can measure basement tilts within the expected range for tectonic plate interaction-induced deformations. Different values for e_0 and γ were also explored with even more favorable results, for example, when considering smaller void ratios observed in marine environments, which can be as small as 1.6, or considering lower stress gradients up to 2.5 kPa/m that have also been measured in seabed clays. It should therefore be noted that uncertainties in the properties of the sediments mean that the model developed here should only serve to provide confidence in the interpretation of the tilting data presented next.

2.4. SSE-induced seafloor tilt

Available tilt raw data from stations OBT4, OBT5, OBT7 and OBT8 with 24 h sampling rate are shown in the left column of Fig. S12. Among the discontinuities found, the most prominent in both components is from the Mw7.0 Acapulco earthquake at station OBT5 (Fig. S12), located 55 km west of the epicenter (Fig. 1). To estimate the orientation of the tiltmeters, we used baselines from the outliers-free time series shown in the right column of Fig. S12. The procedures for both this estimation and outlier removal are described in the Section 4.4 of Materials and Methods. If the hypothesis underlying the orientation of the tilt sensors is correct, i.e., that the baselines tilt rates are dominated by the long-term interplate interaction, then we would expect the tilt discontinuity observed in OBT5 from the 2021 Acapulco earthquake to be close to the theoretically expected direction. Fig. 2a shows the comparison of such observed discontinuity with the co-seismic tilt predicted by Okada's [59] model associated with our co-seismic slip distribution. This calculation considers the site bathymetric elevation. The dotted line in the tilt representation depicts the basement tilt axis and the arrow, the theoretical tilt vector. Although the magnitude of the observed discontinuity has been normalized to the theoretical value, the consistency in the direction of both quantities is remarkable and gives confidence in both, the TMA model and the procedure introduced for the orientation of sensors.

To remove the sediment-induced tilt amplification from the data, following Cruz-Atienza et al. [33], we first inverted GNSS data for the inter-SSE deformation period between September 1, 2019, and April 1, 2021 (Fig. 4) to retrieve the plate interface coupling, defined as $1 - v/v_{pl}$, where v is the interplate slip rate, v_{pl} is the plate convergence rate equal to 6.6 cm/yr in Acapulco[60] and $v \leq v_{pl}$.

To this purpose, we used the same ELADIN method [51] as for the co-seismic slip inversion, which honors physically consistent restrictions at the plate interface (i.e., slip rake angle, tectonically admissible backslip and von Karman slip distributions) via a gradient projection strategy [33,52]. Details of the inversion and [51]resolution analysis can be found in Section 4.5 of Materials and Methods. The benefit of using offshore data including tilt in the inversions will be discussed in Section 3.5 and can be appreciated in Fig. S17 for a checkerboard inversion test.

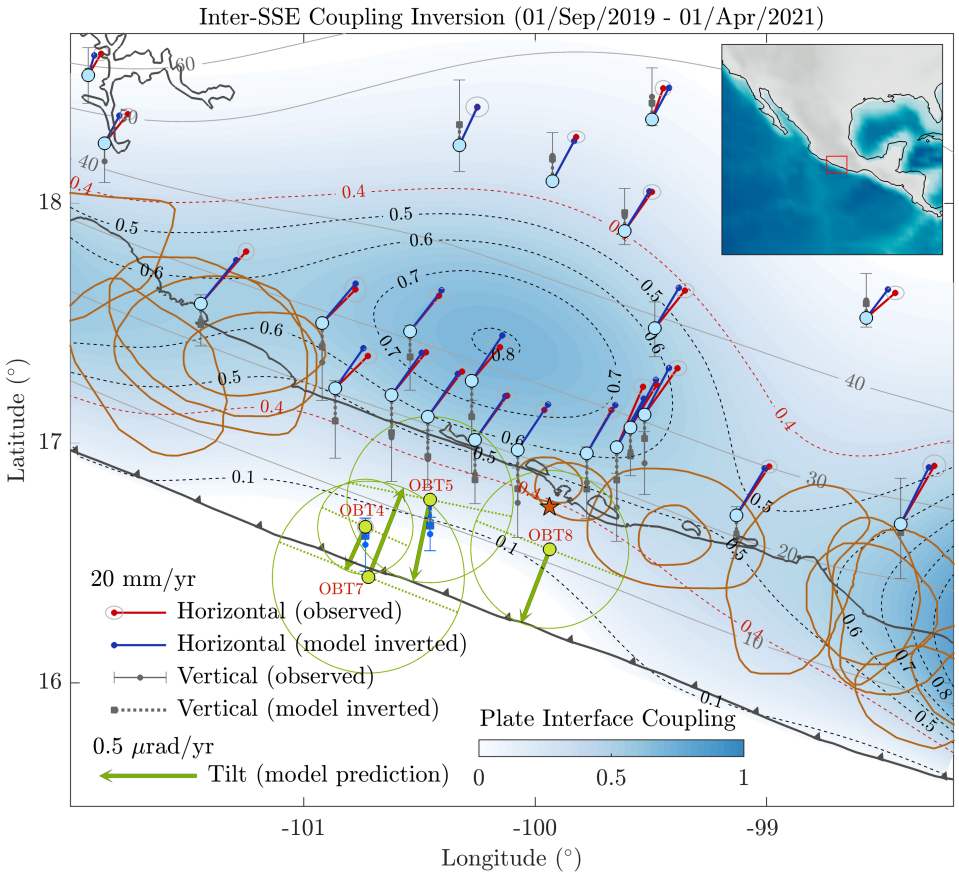

Figure 6 Inter-SSE plate interface coupling inversion from GNSS displacements. Tilt model predictions at our forearc seafloor tiltmeters OBT4, OBT5 and OBT8 are shown with green arrows, where the dotted green lines indicate the tilting axis. Tilt at OBT7 upon the Cocos plate was estimated independently (see text). Predictions for the vertical displacement at OBO4 and OBO5 are compared with drift models shown in Fig. 3b and c. Brown shapes delineate historical rupture areas.

Fig. 6 presents the inter-SSE coupling inversion of three-component GNSS data along with the aftershock areas of all historical earthquakes in the region (brown shapes). Although we believe that our long-standing pressure records are devoid of significant instrumental drift and thus that they are useful for the inversion, we did not include in the inversion the secular vertical displacements at OBP4 and OBP5 referred to the Cocos plate (i.e. to OBP7) (Figs. 3b and 3c). However, when comparing these displacements with the theoretical prediction derived from the

coupling model (blue vertical bars), we find that they are consistent, which points to the validity of our drift conjecture.

As previously found by Radiguet et al. [25] during short-term inter-SSE deformation periods, the interface coupling between Papanoa (101°W) and Acapulco (100°W), i.e. within the oldest segment of the seismic gap, is significantly deeper (about 10-15 km) and greater (reaching values of 0.8) than in the adjacent segments. Note, for instance, that the 0.4 coupling contour (red dotted) is deflected into deeper regions along the gap and encloses the shallower rupture zones of earlier earthquakes. Also interesting is the offshore rapid decrease of coupling when approaching the trench in the gap, with values below 0.1 for depths smaller than 10 km (i.e., along a ~25 km wide and ~150 km long trench-parallel interface strip). Although this coupling pattern suggests a very particular mechanical behavior of the interface that could partially explain the existence of the seismic gap, we note that it does not reflect the effective long-term stressing rate since deep SSEs periodically occur in Guerrero, releasing a large part of the accumulated strain energy where coupling is the largest around 35 km depth[25].

From our inter-SSE coupling inversion, we can calculate the theoretical tilt rates at the tiltmeter locations using Okada's [59] model to compare with the observed rates determined from the baselines used to orient the sensors, reported in Table S2. Fig. 6 shows those model predictions (green arrows), with magnitudes of 0.245 μrad/yr at OBT4 about 9 km from the trench, 0.427 μrad/yr at OBT5 and 0.406 μrad/yr at OBT8, both sites about 30 km from the trench. The estimated long-term rate of -0.494 μrad/yr on the Cocos Plate (i.e. at OBT7, which sits on the footwall) was derived independently from the geometry of the Cocos Plate and its absolute convergence rate to the North American Plate. Based on a 50 m resolution bathymetric map, the convex geometry of the Cocos plate in the vicinity of the trench was described by fitting a polynomial, so that by multiplying the spatial derivative of this function at the OBT7 location by the plate convergence velocity, the secular tilt rate can be estimated (Kostoglodov et al., in preparation, 2025). Note that tilt rates away from the trench (in OBT5 and OBT8, Fig. 6) are about 15% smaller than in the Cocos plate and twice as high as predicted near the trench in the overriding plate (OBT4). From these theoretical tilt magnitudes and those determined from the data baselines, we can estimate the tilt amplification factors, A_t, at each site as reported in Table S2, which range from 849 on the Cocos plate to 5,757 on the overriding North American plate. The much higher amplification at OBT8 is certainly related to two factors: a much higher tilting rate in the baseline due to the ongoing SSEs throughout the recording period, and the sediment properties in the continental slope down from Acapulco Bay, where several submarine canyons surround the station (unlike OBT5, Fig. 1) and thus where sediment compressibility may be higher than 1.8 [57]. On the other hand, since OBT4 is characterized by a steady, secular deformation with no clear trend, we assumed the same amplification for this site as for OBT5, which led to very consistent results, as discussed later.

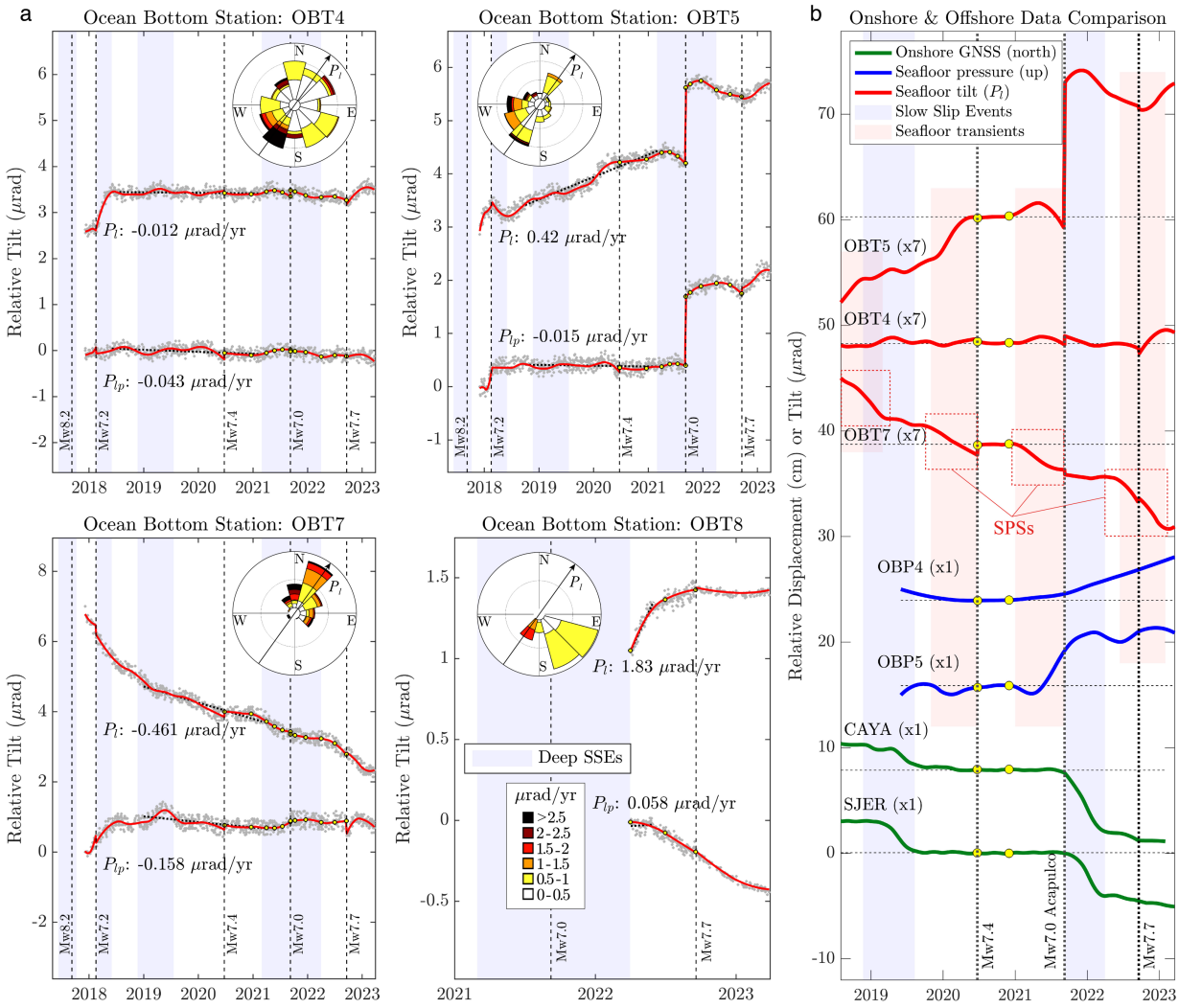

Figure 7 Observed seafloor tilt and comparison with independent data. (a) Tilt data along the plate convergence (P_l) and its perpendicular (P_{lp}) directions at our four tiltmeters after sensors orientation and calibration from theoretical predictions during an inter-SSE period. The windrose histograms indicate tilting directions and rates from 30 days moving windows with five days overlap, where the arrows indicate the plate convergence direction. Reported tilting rates detach from the linear regressions shown with dotted black lines. Yellow dots indicate the boundary dates of the 10 inverted time windows. (b) Comparison of tilt data in the long-standing stations (red) with collocated vertical displacements at OBP4 and OBP5 (blue, Fig. 3b and c) and two selected GNSS sites near the coast (green, see Fig. 1). All data were detrended from linear regressions between the yellow dots for comparison. The red dotted rectangles indicate the occurrence of *slab-pull surges* (SPSs).

To correct the tilt data from the sediment-induced amplification, we simply divided the time series by the corresponding amplification factor A_t (Table S2). This procedure neglects possible amplification variations with α predicted by our TMA model (Fig. 5b). However, as explained earlier, this assumption is a reasonable proxy since tectonic tilt changes are within fractions of micro-radians. Fig. 7a displays the amplification-corrected tilt data in the four sites. Because the

corrections are based on theoretical predictions, reported long-term tilt rates should only be taken as self-consistent approximations of the actual plate deformation, useful for the joint interpretation of onshore and offshore data. As we will see, the most valuable information relies on the short-term tilt variations, which often correlate in time between the stations (red curves, Fig. 7b). The windrose diagrams of Fig. 7a show the tilt rate histograms for 30-day moving windows with five-day overlap, except for OBP8 where we took 15-day windows. Arrows within the histograms indicate the plate convergence direction, which allows to see how the tilt directions vary throughout the whole data window compared to that reference direction. For instance, while station OBT7 on the incoming Cocos plate always tilts in the plate convergence direction (northeast quadrant), station OBT5, which is seated on the overriding North American plate, does in the opposite direction (southwest quadrant) except for some tilt reversals that correspond, as we will see later, to transient rebounds associated with SSEs within the blue and red background shades (Fig. 7b). On the other hand, station OBT4, which is close to the trench upon the forearc, features a much steadier behavior with tilt episodes covering all azimuths. The most rapid tilting period occurred at OBT4 during the 2018 Guerrero SSE just after the Pinotepa earthquake [33].

Fig. 7b shows an onshore-offshore multiple data comparison. For a better inspection, all time series were detrended from linear regressions between the yellow dots covering a six-month quiescent period and GNSS co-seismic discontinuities removed. Positive tilt increments will from now on represent seaward tilt opposite to the Cocos plate convergence, while negative increments will represent tilt in the Cocos plate convergence direction. The two selected GNSS time series (green curves) essentially show the 2019 and 2021 deep SSE in Guerrero (blue shades), with some variability around them. With a clear delay compared to the GNSS signals, transient tilt variations are also present in the three tiltmeters for the 2019 and 2021 SSEs. Nonetheless, the seafloor data further features very rich, potentially meaningful transients absent or barely present at the onshore sites (red shades). To assess whether such data fluctuations correspond to tectonic deformations, consistency between different sites and types of data is important. For instance, within the red shade preceding the Acapulco earthquake, the three tiltmeters and the two pressure sensors detected significant to large variations. As discussed in Section 2.2, during that period only the stack of GNSS data allowed to clearly see the onshore elastic rebound prior to the earthquake (Fig. 4b).

A noteworthy and meaningful observation emerges when the tilt history at OBT5 is compared with that at OBT7 on the Cocos plate (Fig. 7b). With the exception of the post-seismic period following the Acapulco earthquake, which may be regarded as exceptional in terms of the dynamic and mechanical consequences associated with the rupture, there is a consistent pattern whereby, when the Cocos plate accelerates tilting, OBT5 also experiences a tilt acceleration towards the trench (positive slopes) before stabilizing or reversing the sign if, for example, an offshore SSE occurs as discussed later in Section 3.2. This can be clearly observed in Fig. 7b during the first three seafloor transients and the latter part of the fourth, red shaded.

This multiple-data correlation further suggests that tilt fluctuations actually correspond to offshore tilt due to tectonic activity preceding the Acapulco earthquake and point towards the same conclusion for other transients such as those depicted by the other red shades around the Mw7.4 Huatulco and Mw7.7 Michoacan earthquakes. Another way to assess whether tilt variations are of tectonic origin is to confront the offshore and onshore data together with a physically consistent plate interface slip model, as discussed in the next section.

2.5. Joint inversion of seafloor tilt, hydrostatic pressure and GNSS data

Because tilt depends on the spatial derivatives of vertical displacement, tilt records are much more sensitive to changes in slip than GNSS and OBP data. Unlike the classical linear inversion of displacement, the joint inversion of displacement and tilt is an optimization problem that requires careful treatment. One way to address this challenge is through regularization of the model parameters. We use the ELADIN method for this inversion because it provides a robust regularization that excludes unrealistic solutions while taking advantage of the tilt sensitivity to slip. Important considerations for properly performing the joint inversion and resolution analysis are detailed in Section 4.6 of Materials and Methods.

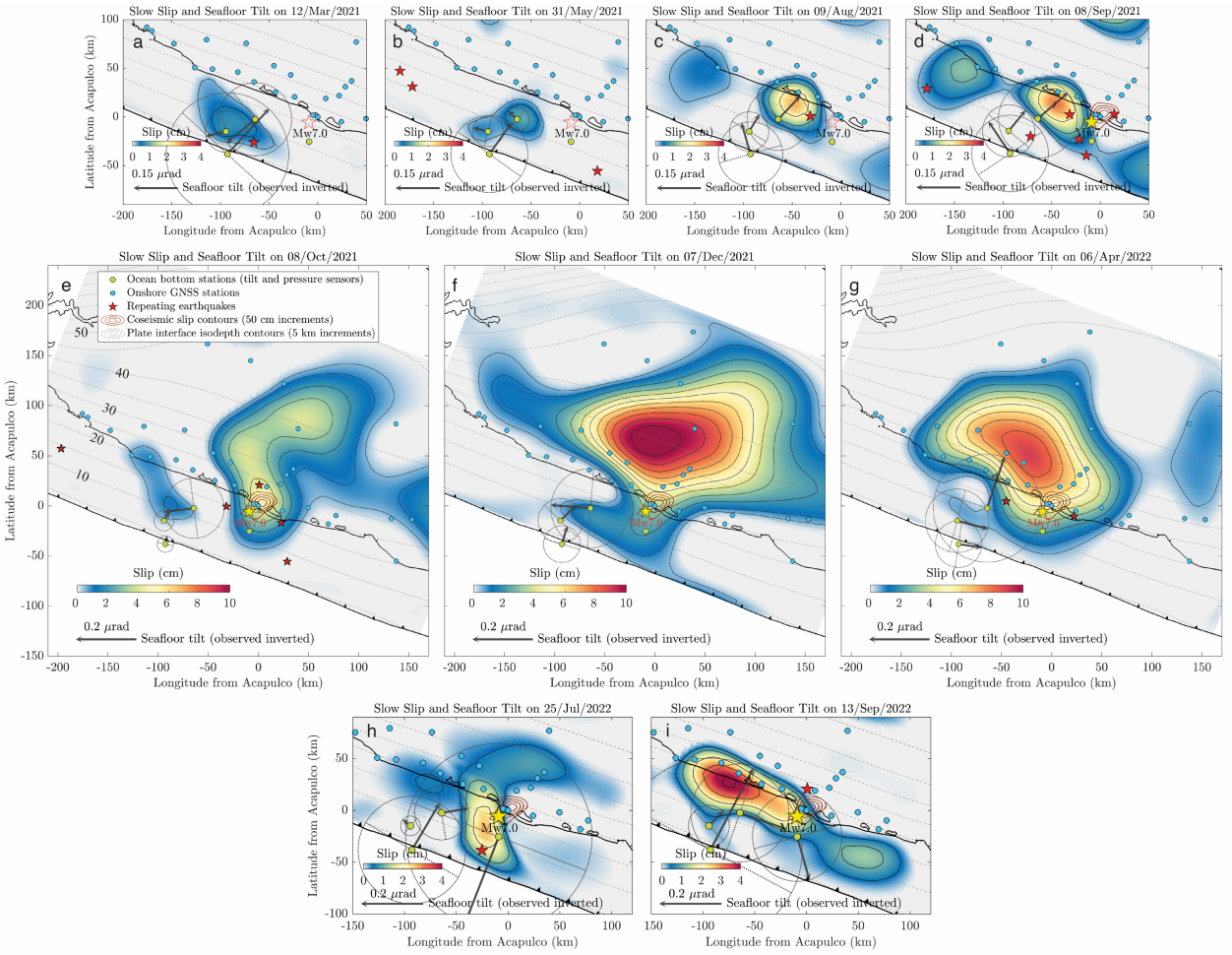

Figure 8 Plate interface slip evolution from joint inversion of onshore GNSS data and seafloor pressure and tilt data. The slip at the time indicated in each panel heading comes from the interpolation of the 10 inverted solutions whose data fit are shown in Fig. S18 (left column). Observed tilt is displayed on each panel (black arrows). The yellow star indicates the Acapulco earthquake epicenter, while red stars the location of repeating earthquakes within ±10 days.

Fig. 8 presents the resulting plate-interface slip at nine different moments along with the observed ocean bottom tilt (Movie S1). Because of the Okada model limitations used to calculate the

Somigliana Green's functions (involved in the inversion technique), tilt at OBT7 (Cocos plate) was not used for the inversions but appears in the figure (and movie) for a better and comprehensive assessment of the phenomenology. Panels a-d zoom-in the offshore interface activity before the Acapulco earthquake, where a transient SSE initiated early 2021 next to the oceanic trench (i.e., next to OBO4) and migrated during the following five/six months towards the coast and then east, towards the earthquake hypocenter in its late stage (also see Fig. S18e). The tilt is consistent at OBT4 and OBT5, where gradually and synchronously changes orientation from SW to NE following such a slip migration (Movie S1 and Fig. 7a-d). Of substantive importance to validate this result is the consistent vertical deformation recorded in the collocated OBPs, which are also well explained by the model (Fig. S18 b-e, left column). An independent (non-inverted) and meaningful observation comes out from OBT7 on the Cocos plate, where tilt accelerates when the near-trench SSE develops (Figs. 8a and Movie S1). This can be clearly seen in Fig. 7b at OBT7 during the third seafloor transient (red shade), where the Cocos plate undergoes an evolving shoreward tilt of approximately 0.5 μrad from early 2021 that stabilizes about two months before the earthquake. To the best of our knowledge, these transient seafloor tilt signals associated with an SSE and the associated inversions are the first to be formally reported.

To assess how much the seafloor data contributes to the inverted models as compared with the onshore GNSS displacements, we performed all the inversions independently (Fig. S19) for GNSS data only (left column), for GNSS and OBP data only (middle column), and for GNSS and tilt data only (right column). All three inversions determine that an offshore SSE happened along the Costa Grande west of Acapulco during the ~2 months preceding the earthquake (see Figs. S19e and 4b for the GNSS evidence of the SSE). All solutions find also a deep, onshore SSE activated in that period. However, only inversions including data from OBOs 4 and 5 can trace what occurred before and far from the coast. Noteworthy is the occurrence of the aforementioned near-trench SSE during the first three months of 2021 and then its slow coastward migration, determined using independently pressure and tilt data. During the ~2 months before the Acapulco earthquake, it is the outstanding tilt transient at OBT5 (see Fig. 7b), which points towards the northeast, that "pushes" the slip eastwards toward the rupture hypocenter. Something similar happened during the last two inverted windows (from April to September 2022), when a second offshore SSE took place south and northwest of Acapulco (Figs. 8h-i and S19i-j). As for the remaining windows after the earthquake when the rupture afterslip and a large long-term SSE occurred, the joint inversions of the whole data set (Fig. 8e-g) did not differ significantly from the independent inversions (compare with Fig. S19f-h). All these results show that ocean bottom tilt and pressure were essential, reliable and complementary for imaging the evolution of the first two offshore SSEs ever seen in the Mexican subduction zone.

2.6. Seismic evidence of slow slip and earthquake nucleation

Slow earthquakes such as tremor and low frequency events are modulated by slow slip on the plate interface[15,61], as are repeating earthquakes and background seismicity in general [62,63]. To validate our geodetic inversions and have insights into the plate interface mechanism leading to the Mw7.0 Acapulco earthquake, we develop an independent analysis based on the detection of small, unreported earthquakes by means of a Template Matching (TM) technique [64] (see Section 4.7 of Materials and Methods). We used 3-year-long continuous records from January 1, 2020 to December 31, 2022 at 8 broadband seismic stations distributed across the state of Guerrero (inset in Fig. 1) in a region about 480 km length including the seismic gap (Fig. S20a). Our final catalog

includes 38,501 events with magnitude larger than 3.2, which is above the completeness value Mc = 3.1 (Fig. S20b and c). During this period, 410 out of 768 known sequences of repeating earthquakes in southcentral Mexico[65] were activated. Representative waveform examples of detected and repeating earthquakes are shown in Figs. S21 and S22, respectively.

We seek to identify regions around the plate boundary where seismicity rate anomalies are significant to assess whether they correlate with the slow slip history determined in the previous section. Furthermore, we are interested in knowing whether repeating earthquakes occurred where slow slip was detected by ocean bottom instruments, which would represent a strong confirmation of the existence of aseismic slip in the surrounding fault matrix [62,63,66]. To do so, we first established a baseline for the background seismicity rate between January 1, 2020 and April 1, 2021, a period prior to the geodetically identified tectonic activity. Section 4.8 of the Materials and Methods explains the procedure for establishing the baseline.

The first interesting observation occurs 10 days before the Acapulco earthquake in the two east-west flanks bounding the pre-seismic SSE offshore, where the seismicity rate increased significantly (Fig. 9a left panel). Of particular interest is the seeming increase in the hypocentral region of the Acapulco earthquake, to the east. A detailed analysis of that region, i.e., within 20 km of the hypocenter (Fig. 9b left panel), reveals that the seismicity indeed increased well above the baseline during the 15 days prior to rupture (i.e., the seismicity rate doubled as compared with the five preceding months, right axis), when the offshore SSE pervaded the hypocentral zone (Fig. 8d). During the 3.5 months following the earthquake when the deep long-term SSE starts developing, average deviations largely exceed 50% in two well-localized spots (Fig. 9a right panel), with the western patch being larger around the co-seismic slip but with a clear offset to the east containing most of aftershocks. Interestingly, the eastern active zone is well delimited and away from the seismic rupture (about 60 km), where the M7.5 and M6.9 earthquakes of 1957 and 1989, respectively, occurred. In fact, a simple inspection of the seismicity rate history on that spot (Movie S2) reveals that during the first 20 days after the Acapulco earthquake the seismicity is sharply increased, suggesting that there was the possibility of a M7+ doublet similar to that of 1962 (Fig. 2a), but this time to the east of the first earthquake.

The occurrence of repeating earthquakes during the pre-seismic offshore SSE is remarkable. Fig. 9b (right panel) shows these events during the entire geodetically analyzed period along with the cumulative slip (contours) up to the Acapulco earthquake time. Between December 2020 and September 8, 2021, seven repeating sequences activated offshore (inset Fig. 9b left panel). The first two very close to the trench (sequences A and B, right panel), where the SSE initiated (Fig. 8a and Movie S1), while the later four concentrated where the SSE gained strength, about 15 km offshore (one example is sequence C). Waveforms of the three selected sequences are shown in Fig. S22. This evidence is particularly important because it points in the same direction as the seafloor geodetic observations, where a slow dislocation initiated near the trench and migrated slowly towards the coast, where the earthquake occurred. During the first three months following the earthquake, the repeaters rate increased sharply (inset Fig. 9b left panel) around the co-seismic slip and notably southwest of the hypocenter, where the pre-seismic SSE pervaded the hypocentral zone. These repeaters clearly span the post-seismic slip region (Fig. 8e-f), both updip and east from the rupture, which provides further confidence about the migration of the SSE southwest from Acapulco, where the pre-seismic repeaters took place.

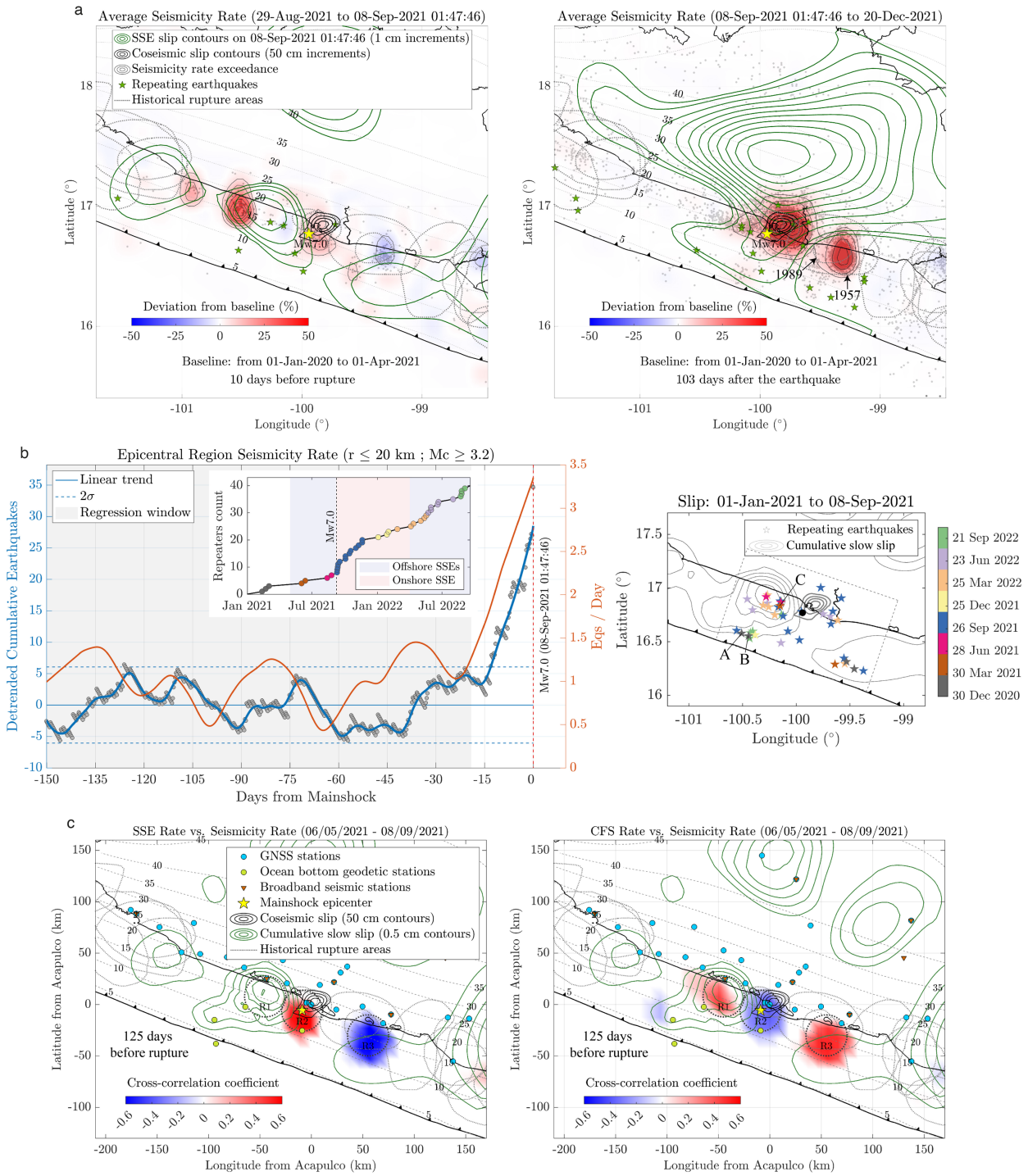

Figure 9 Analysis of template matching seismic detections (M > 3.2). (a) Seismicity rate deviations from a baseline averaged over the 10 days before the Acapulco earthquake (left) and the 103 days after the rupture (right). Green contours depict the cumulative slip on those periods and the green stars the epicenters of the associated repeating earthquakes. (b) Detrended cumulative earthquakes within 20 km from the Acapulco earthquake hypocenter (left axis) and associated occurrence rate (right axis). The inset shows the cumulative repeating earthquakes color coded as identified in the right panel, which shows the events location together with the cumulative slip over the eight months

before the earthquake (contours). Labels A, B and C indicate three selected sequences whose waveforms are shown in Fig. S21. (c) Temporal cross-correlation coefficients between seismicity rate deviations and slip rate on the left and CFS on the right, during the three months preceding the rupture (see headings). The contours correspond to the cumulative slip during this period.

Lastly, we aim to investigate whether slow slip in the hypocentral region was the dominant process leading to the rupture of the Mw7.0 mainshock. We search for evidence allowing to identify such process at the plate interface that led to the abrupt increase of foreshocks around the hypocenter (Fig. 9b left panel) and thus to the earthquake nucleation. For this we calculated the cumulative Coulomb Failure Stress (CFS) at the interface associated with each geodetic inversion of slip and coupling (Fig. S18 right column) by means of an artifact-free triangular dislocation model [67] (see Section 4.9 of Materials and Methods). [68]

The most striking evidence appears three months before the Acapulco earthquake in the hypocentral region R2 (Fig. S24c; see Fig. 9c for circular regions location), where seismicity has a maximum correlation ($cc \approx 1.0$) with slip rate (left panel) and a maximum anticorrelation ($cc \approx -1.0$) with CFS rate (right panel). In contrast, the correlations are roughly reversed during the same period and beyond in the R1 and R3 regions (Fig. S24b and d), where seismicity is highly correlated with the CFS rather than the slip rate. The same result is summarized in the maps of Fig. 9c, which show average cc in the three months before the earthquake for the slip rate (left panel) and the CFS rate (right panel). Although earthquake nucleation is sensitive to several mechanic and dynamic processes, in this case, the available evidence suggests that it was the slow slip invasion of the hypocentral zone that dominated the foreshocks activity and, therefore, likely the Acapulco earthquake nucleation over the Coulomb stresses during the rupture preparation. Although less representative of short-term interface dynamics due to averaging over a much larger window (see panels heading), the maps in Fig. S24a show that slip rate dominated the seismicity rate around the rupture zone and in a wide region east of it, while CFS played its part in the surrounding region, including shallow offshore depths near the trench. It should be noted that the CFS estimates suffer from significant uncertainties due to the unknown pre-stress and local mechanical conditions of the interface, so that their predictive power in the short term may be limited.

3. Discussion

3.1. Slip evolution, interface mechanics and seismogenesis in the gap

During 1.7 years, between December 2020 and September 2022, the plate interface around the Guerrero seismic gap slipped continuously with alternating activation depths. In early 2021, an interface dislocation (on the order of 1.5 cm) starts very close to the trench and slowly migrates (during five to six months) towards the coast where it gains strength from June to develop between 10 and 25 km depth (Mw6.8 up to 4 cm, Figs. 10a and 8a-c). In its final two-month stage, the event extends eastward to penetrate the hypocentral zone of the Mw 7.0 earthquake that occurred on September 8, 2021 (Fig. 8d). Simultaneously starting in July, another slow dislocation initiates at depth (Figs. 10b, S18e and Movie S1). That is, the plate interface decouples simultaneously above 25 km and below 40 km, segments that seem to bound the two transition zones of the interface within the gap where short-term SSEs take place. The shallow SSE is accompanied by repeating earthquakes (from the trench to the shoreline) that corroborate its existence where ocean bottom geodetic observations (i.e., hydrostatic pressure and tilt) detect it (Fig. 9b). The correlation between

the sharp increase in seismicity and slip rate in the hypocentral zone during the 15 days prior to the mainshock on the one hand, and the anticorrelation of such seismicity with the CFS (Fig. 9c) suggest that both foreshock activity and earthquake nucleation were dominated by local stress concentration in isolated asperities with aseismic slip surrounding them (Fig. 10b).

Although the juxtaposition of different driving mechanisms certainly results in the nucleation of mainshocks [63], the evidence for the Acapulco earthquake suggests that the sharp increase in the foreshock rate around the hypocenter (Fig. 9b left panel) may be the result of mutual stress transfer between the aseismic slip on the fault matrix and the foreshock asperities, which eventually focus around the nucleation point to reach the characteristic length at which slip accelerates to unfold in the main rupture [69,70]. Only a few cases have been documented in subduction zones where slow slip (or aseismic pre-slip) appears to penetrate or be very close to the nucleation zone, such as the 2011 Tohoku [2,63] and 2014 Iquique [32,71,72] megathrust earthquakes.

During the first two months following the September 8 earthquake, the post-seismic slip completely sweeps the rupture zone reaching depths of less than 10 km (Movie S1, Figs. 8e and S18f). In that period, there is an outstanding reactivation of repeater sequences to the east and south of the rupture where the afterslip develops (Fig. 9b right panel). Beginning in November, a large long-term SSE (Mw7.7 and maximum slip of ~22 cm, Fig. 10a) develops mainly between 20 and 45 km depth (Figs. 8f and S18g) and lasts until April 2022. However, in its late phase, between December and April 2022, the SSE grows pervading shallow depths offshore of 10-15 km along the entire seismic gap to the southwest of Acapulco (Figs. 8g and S18h). Although dominant below 25 km, the long-term SSE outstandingly overlaps to the east with the 1957 and 1989 rupture areas (Fig. 2a), where most of the Acapulco earthquake aftershocks occurred. Although this region appeared ripe for failure in the 10-20 days after the earthquake, a doublet similar to that in 1962 never happened (Movie S2 and Fig. 9a right panel). The updip propagation of long-term SSEs in Guerrero has been observed previously[25,33,51]. What we were previously unaware of was the existence of shallow SSEs and their role in the seismogenesis of potentially devastating earthquakes within the gap, which as described earlier, seems fundamental.

From April 2022, the offshore region south of Acapulco reactivates to initiate the second shallow SSE that may have reached the oceanic trench (Mw7.1, Figs. 10a, 8h and S18i). Then, between July and September 2022, during the three months prior to the Mw7.7 Michoacán earthquake some 350 km to the west (Fig. 1), the SSE evolves to activate a 230 km long offshore strip between 8 and 25 km deep that spans the entire seismic gap and the Costa Chica of Guerrero (i.e., east of Acapulco), with maximum slip of 4 cm northwest of OBO5, where the CFS exceeds 70 kPa (Figs. 8i, S18i-j). The strip has a distinctive shape, characterized by a deeper profile in the west along the gap, where the long-term SSE penetrated onshore regions following the earthquake (similar to the first shallow SSE event, Fig. 10a). This depth profile transitions to a shallower interface region in the east along the Costa Chica, where the slip occurred entirely offshore and encompassed the rupture areas of 1957 and 1989 (Fig. S18j). Interestingly, as occurred before the Acapulco earthquake (Fig. 10b), on the edge of the Mw7.7 Michoacán rupture, the deep part of the interface (>40 km) is also reactivated (Fig. S18j and Movie S1). In this regard, please further note how the tilt in the Cocos plate (OBT7) is strongly accelerated in that four-month period (Fig. 8i and Movie S1) as occurred before the Mw7.4 Huatulco (~430 km east, Fig. 1) and Mw7.0 Acapulco earthquakes (see red shaded transients at OBT7 in Fig. 7b), suggesting a regional episodic activation of the subducted slab, possibly related to the occurrence of the three earthquakes.

A comprehensive summary of the seismic gap activity is presented in Fig. 10a. The most striking observation is the along-strike continuity between the historical rupture areas and the two shallow SSEs observed for the first time in Mexico. Our results reveal that the locked seismogenic depths outside the seismic gap align with these short-term slow slip earthquakes within the gap. This indicates that the concept of locked depths in the gap, as commonly understood, may require re-evaluation. The baseline of background seismicity in this segment (M > 3.2), between Papanoa (101°W) and Acapulco (100°W), is significantly heterogeneous along the strike (Fig. S23a). In the eastern half of the segment, where the two shallow SSEs intersect, seismicity rate is about 10 times higher than observed in the western half, where two Mw 6.1 and 6.5 events occurred a few weeks after the Mw7.3 Papanoa earthquake west of the gap in 2014 [73]. Thus, mechanics of the interface to the east seems more prone to slow slip and small ruptures (and repeaters, see Fig. 9b right panel) than the western part. Further study is required to confirm this hypothesis, but the evidence suggests that SSEs in the gap do not inhibit the occurrence of small to moderate seismicity compared to segments where M7+ earthquakes occur regularly. The lack of large ruptures within the gap over the past 113 years can be attributed, at least in part, to the occurrence of recurrent episodes of aseismic energy release at shallow depths (i.e., short-term shallow SSEs).

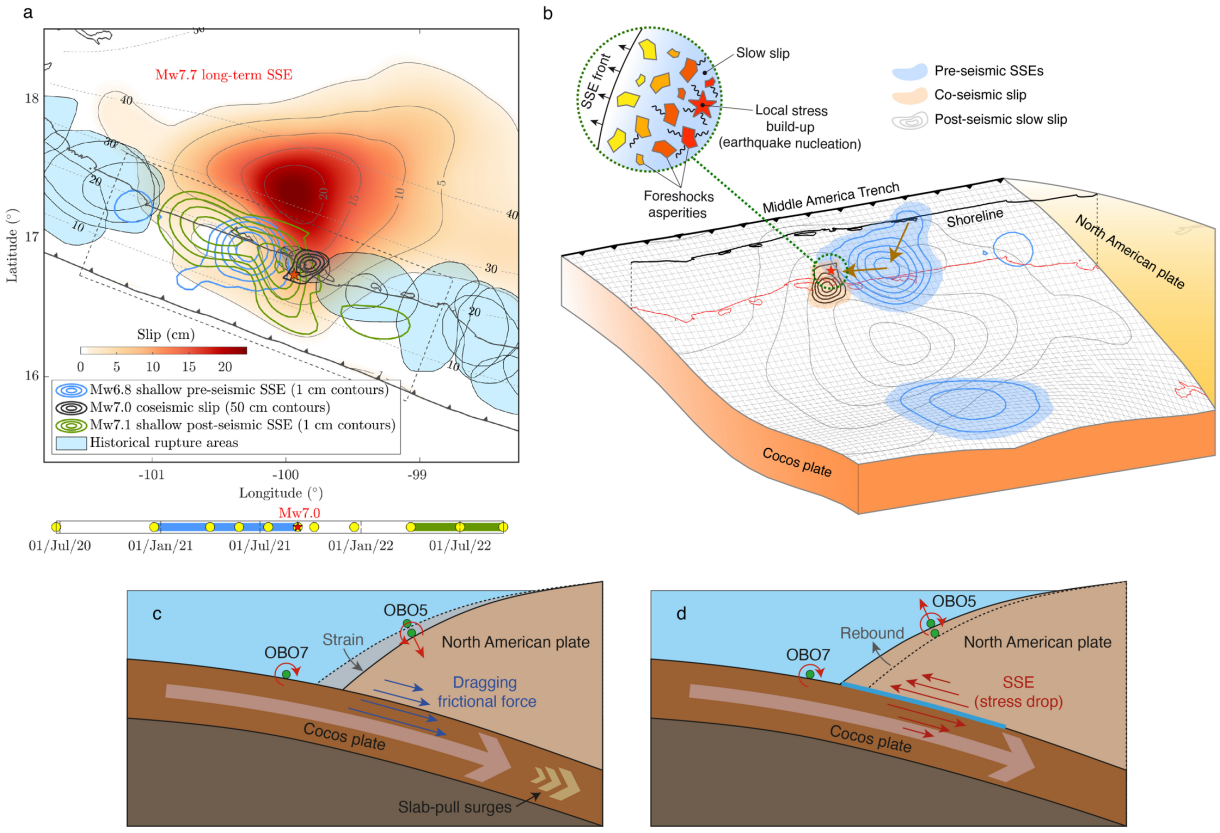

Figure 10 Summary of the Guerrero-gap plate interface activity and explanatory features of seafloor deformation patterns. (a) Slip associated with the two shallow SSEs (blue and green contours) together with the cumulative slip (red to orange shaded) over the 6.9 months after the Acapulco earthquake (i.e., between 09/08/2021 and 04/02/2022; see bottom timeline). (b) Shallow and deep pre-seismic slow slip (blue shading) over the 8.7 months preceding the earthquake,

together with the co-seismic slip and hypocenter (red star) of the Mw 7.0 rupture. The inset shows the pre-seismic SSE invasion of the hypocentral region and the local stress concentration on foreshock and mainshock asperities. The grey contours show the Mw7.7 post-seismic slow slip. (c and d) Seafloor deformation patterns (displacement and tilt) in the oceanic and overriding plates during an inter-SSE period (left) and a shallow SSE (right).

Moreover, the presence of a relatively silent zone offshore in the western sector of the gap, pointed out by Plata-Martinez et al.[22] (red dotted rectangle, Fig. S23a), coupled with the observation of tremor in the vicinity of the trench, provides further evidence to this scenario where slow dynamics prevails and fast instabilities are seldom large. Nevertheless, although unlikely as evidenced by the historical record, the potential for large ruptures in the gap resulting from short- and long-term constructive strain interactions and dynamic rupture effects cannot be discounted. This study (see, for instance, the cumulative CFS in Fig. S18) and considerations from other regions [2,52,74] provide evidence to support this scenario.

In view of the uncertainty surrounding the tilt baseline at OBT8 due to the absence of a long-term, steady period of observation, as elucidated in Section 3.4 (bottom right, Fig. S15), it is pertinent to inquire whether the second shallow SSE truly occurred south of Acapulco (Fig. 8h). The tilt baseline period was selected in order to ensure consistency between the tilt direction at the station between April and July 2022 and the seaward and downward GNSS displacement at the closest sites (Fig. S18i). Nevertheless, this decision is somewhat arbitrary and may result in implausible outcomes. In order to address this issue, inversions were performed for the final two windows during which OBT8 was operational, with the tilt data excluded. Figs. S19i and j illustrate a comparison of the slip solutions when inverting GNSS data alone (on the left), GNSS data combined with OBP data (in the middle), and GNSS data combined with tilt data (on the right). The solutions with and without tilt in the first window are found to be highly similar in the region south of Acapulco, due to the absence of an OBP in the vicinity. They both identify an offshore SSE with a peak value of approximately 1.5 cm. A similar conclusion can be drawn with regard to the final window (panel j), where the long SSE strip identified in our preferred solution (Figs. 8i and S18j) emerges in all instances, albeit with some variations to the west and southeast of Acapulco. Consequently, the baseline period selected for OBT8 appears to be a reasonable choice, given that independent inversions yielded comparable results, with all observations satisfactorily explained.

During the last window between 1 July and 18 September 2022 preceding the Mw7.7 Michoacan earthquake about 350 km west (Fig. 1), our preferred slip solution (Fig. S18j, as well as the three independent ones, Fig. S19j) features a large dislocation close to the western limit of our inversion domain. While the closest GNSS data (e.g., ZIHU station) is well explained and the CFS is high (above 50 kPa, Fig. S18i), our model lacks resolution in that sector (Fig. S16). Therefore, further investigation is necessary to confirm what occurred near the Guerrero-Michoacan states boundary in that period. A similar situation happens in the window preceding the Acapulco earthquake, between 16 July and 8 September 2021 (Figs. S18e-f). During this period, a large slip patch emerges in the eastern region of the domain. Although the resolution at this end is also inadequate, an independent analysis (not shown) of GNSS data from Oaxaca during this period corroborates the presence of a long-term SSE in the state, as evidenced by the southwestward displacements at TNMQ and OMTS stations in the vicinity of the Oaxaca border.

3.2. Near-trench deformations and deep slab activation

As far as we know, the long-standing continuous data from our ocean-bottom tiltmeters are without precedent globally. In light of these observations, it becomes necessary to consider the potential role of tectonic processes that have been rarely observed in the preparation of significant ruptures at a regional scale. Figs. 10c and d illustrate a segment of the seismic cycle in which an SSE occurs in the vicinity of the trench. During an inter-SSE period, deformation of the forearc resulting from subduction and coupling at the interface causes a distinct displacement and tilt of the ocean floor, as illustrated at station OBO5 in panel c. In this period, the station sinks and tilts in the trench direction, as evidenced by the data at that site (see the associated windrose histogram in Fig. 7a), which are predominantly opposite to the plate convergence. When an SSE below occurs and continental rebound takes place (Fig. 10d), deformation reverses directions of the observables at OBO5, which implies tilt reversals (and uplift) also present in the histogram with the direction of convergence (associated with the negative slopes at OBT5 in Fig. 7b).

During the initial phase of the tilt transient preceding the Acapulco earthquake (red shade, Fig. 7b), OBT7 starts accelerating with negative slopes (shoreward tilt), while OBT5 accelerates with positive slopes (tilt towards the trench; pattern also found in the first and second transients, and within the fourth transient from the Mw7.7 earthquake). The collocated hydrostatic pressure at OBP5 indicates a sinking trend, which aligns with the stage depicted in Fig. 10c (the same situation is clear in the second transient). During the second half of the transient, when OBT7 begins to decelerate, OBT5 reverses the sign of the slope in a similar manner to OBP5, where an uplift occurs. Both reversals are associated with the previously identified offshore SSE (Fig. 8b-d) (stage corresponding to Fig. 10d). Although of a smaller amplitude, the tilt at OBT4 in this third transient behaves in a similar manner to that observed at OBT5. The disparity in amplitude is likely due to the low interface coupling adjacent to the trench (Fig. 6) and thus to the deficit of stored elastic energy in the forearc front. These observations strongly suggest the existence of a causal relationship between transient processes occurring in the oceanic subducted plate and deformations observed in the forearc.

If we accept the existence of a causal relationship between observations made at OBT7 (Cocos plate) and those made at OBOs seated in the forearc, one is prompted to consider which process may be responsible for triggering the observed phenomena. The prevalent hypothesis would suggest that the slab converges at a constant velocity (in its deep part by asthenospheric drag) and deforms as a function of its interaction with the overriding plate (i.e., as a function of coupling and hence the slip velocity at the plate interface). Thus, a change in interface mechanics (e.g., velocity weakening) would result in a slab rebound and shallow tilt. In this instance, the tilt accelerations observed in OBT7 (Fig. 7b) can be attributed to a change in interface friction and the subsequent elastic response of the oceanic crust to this change. Nevertheless, the available evidence suggests a different outcome because in that case tilt at OBT5 would increase in the shoreward direction as illustrated in Fig. 10d, which is not the case in any of the transients (with the exception of the months prior to the Mw 7.7 Michoacán earthquake, when the second shallow SSE took place). Note that tilt at OBT7 (Cocos plate) exhibits a similar pre-seismic acceleration before the Mw7.4 Huatulco, Mw7.0 Acapulco and the Mw7.7 Michoacan earthquakes. The most reasonable explanation for the simultaneous increase in the tilt rate at OBT5 towards the trench (positive slope) and the tilt rate at OBT7 in the opposite direction (negative slope) during the initial phase of the transients, seems to be that the slab subduction rate increased and friction at the interface remained

stationary, thereby enabling the deformation of the forearc according to the evidence from the data. In this scenario, the forearc tilt is a consequence of the deformation transferred through plate coupling due to the slab underthrusting acceleration (a mechanism similar to that illustrated in Fig. 10c).

The episodic tilt acceleration of the Cocos plate (OBT7) observed several months prior to three regional M7+ earthquakes (with the exception of the initial transient, where a long-term SSE occurred instead) suggests the potential for extended slab episodic processes to precede large regional ruptures. This hypothesis is consistent with the simultaneous activation of a shallow and a deep SSE before the 2021 Acapulco (Fig. 10b) and the 2022 Michoacán (Fig. S18j) earthquakes, which demonstrates that the slab indeed experienced an acceleration along the entire subduction channel before these ruptures. In summary, the observed tilt and hydrostatic pressure data in both the Cocos and forearc near-trench regions suggest that the slab was subjected to transient alterations in its subduction velocity before three earthquakes, lasting between four and eight months, which may be regarded as precursory *slab-pull surges* (SPSs).

A similar idea to that of precursory *slab-pull surges* introduced here was previously advanced by Bouchon et al. [75] based on the analysis of foreshock seismicity prior to the 2010 Maule, 2014 Iquique and 2011 Tohoku megathrust earthquakes. The synchronous occurrence of shallow thrust foreshocks and deep intra-slab normal ruptures led these authors to postulate a causal relationship between both kinds of seismic events, rooted in the transient stretching of the slab deep into the mantle. Months before the Maule and Tohoku ruptures, GNSS observations by Bedford et al. [76] identified also a several month-long transient deformation across thousands of kilometers and a sudden pulldown of the slab, potentially caused by the rapid and deep densification of metastable minerals within the oceanic plate. This model for the Tohoku earthquake preparation is further supported by the massive gravity anomaly found by Panet et al.[77] months before the rupture, which indicates a regional-scale mass redistribution within the mantle announcing the earthquake. The periodic acceleration of the interface slip, as inferred from repeating earthquakes in eastern Japan, and its correlation with the occurrence of large earthquakes point in the same direction [66], where transient processes within the slab perturbing the subduction velocity cause the ruptures. All these findings embrace the idea of *slab-pull surges* as a potentially universal precursor of large to great ruptures, which stem from the near-trench tilt episodes preceding three M7+ regional earthquakes in Mexico.

The ocean bottom instruments that provided the data we analyzed in this study were installed in November 2017 [5], two months after the Mw8.2 intraslab Tehuantepec earthquake of 8 September 2017. In the aftermath of that earthquake, the largest ever recorded in Mexico, the mechanical properties of the plate interface underwent alterations on a regional scale[33]. That is, the instruments were deployed during the period of peak mechanical disturbance of the interface. The unprecedented seismic waves caused dynamic stress perturbations of approximately 100 kPa for over 70 seconds at the interface in the vicinity of Acapulco, more than 600 km away [33]. These transient perturbations triggered an SSE in Oaxaca and drastically disrupted the periodicity and magnitude of SSEs in Guerrero over the subsequent two years[33]. Five months after the rupture, on 16 February 2018, another earthquake (Mw7.2, Fig. 1) was triggered near Pinotepa Nacional by the unfolding Oaxaca SSE [33]. Figure [5]7a illustrates the tilt time series at the three operational stations at that time (OBT4, OBT5 and OBT7) together with the timing of the aforementioned ruptures. From the Mw7.2 Pinotepa earthquake onwards, there was a drastic change in the tilting

tendency of the forearc (OBT4 and OBT5) over the following four months. It is noteworthy that OBT4, situated 9 km from the trench and characterized by long-term stationary behavior, experienced an unparalleled tilt change of approximately 1 μrad in the trench direction (positive slope) during this period. A similar but smaller transient is also present right after the Michoacan earthquake in 2022. At the same time, from the Mw7.2 rupture, OBT5 undergoes a transient tilt reversal in the opposite direction, towards the coast (negative slope). Dynamic perturbations generated by the Pinotepa earthquake (of the order of 70 kPa for ~10 s at the interface near Acapulco), with an epicenter 250 km east of the subsea network, triggered a deep SSE on the Costa Chica of Guerrero (north-northwest of Acapulco)[33], spanning the same period as the tilt transients (blue shaded). The Cocos plate (OBT7), on the other hand, experienced the highest tilt rate in a long time following the Pinotepa earthquake. Preliminary inversion of these signals, which is beyond the scope of this work, reveals that the Pinotepa earthquake also triggered an SSE offshore, in close proximity to the trench. The more comprehensive investigation currently underway, which also has identified contemporary tectonic tremor in OBSs [22], underscores the necessity of ultra-long-period tilt mechanical amplifiers on both tectonic plates to detect SSEs that may also be triggered dynamically by seismic waves from regional earthquakes. These findings will contribute to our understanding of the mechanical response of the interface associated with frequent large events and thus to our comprehension of their role in the evolution of the seismic cycle.

The observation of SSEs offshore and precursory *slab-pull surges* in the oceanic crust was made possible by affordable TMAs. In other words, by unprecedented seafloor instruments that enable the detection of near-trench tilt transients presumably linked to deep processes within the slab and, remarkably, beyond the reach of significant ocean noise, which may seriously obscure tectonic deformations in ultra-sensitive sensors such as OBPs and currently existing ocean bottom tiltmeters. Continuous monitoring of the seafloor tilt utilizing TMAs, at both the incoming and overriding plates, could prove invaluable in identifying short-term processes and patterns that lead to SSEs and/or large regional ruptures at a smaller scale than the aforementioned mega-ruptures in Japan and Chile. Tilt data from all the Fetch units (or similarly design devices) deployed in different subduction zones such as New Zealand, Alaska, the Sea of Marmara, Cascadia and Chile can already be used to do this systematically. The prospective development of future laboratory-designed TMAs with pre-established amplification responses in conjunction with submarine cable systems or real-time satellite data transmission has the potential to markedly enhance our capacity to observe the precursors of and to forecast future catastrophic earthquakes and tsunamis.

4. Materials and Methods

4.1. Acapulco earthquake co-seismic slip inversion

For the inversion we assumed a planar fault, discretized with 2 km subfaults, with the W-phase focal mechanism provided by the USGS (i.e., strike 279°, dip 20° and rake 73°) and a relocated hypocenter at latitude 16.77° and longitude -99.94° with 16 km depth [48]. Furthermore, a von Karman correlation length of 10 km with a Hurst exponent of 0.75 was assumed to spectrally bound the inversion. With a maximum recorded uplift of 20.3 cm at station ACAP (Fig. S2), our preferred source model produced a rms misfit of 0.74 ± 0.47 cm and 0.41 ± 0.28 cm for the GNSS and InSAR data, respectively (Figs. 2 and S4), while Mobile Checkerboard (MOC) resolution tests indicate that the model has a nominal error under 10% within the rupture area for slip patches larger than 10 km (i.e., median restitution indexes above 0.9; Fig. S5).

4.2. Analysis of ocean bottom pressure data

Seafloor hydrostatic pressure is primarily a superposition of harmonic functions (Fig. S6a) associated with ocean tides that can therefore be removed from the records by subtracting theoretical tidal predictions [41] or by filtering data (Fig. S6b-c). However, non-tidal oceanographic components related mostly to ocean currents, gyres and eddies resulting from the wind blowing across the ocean and by differences in the water temperature, density and atmospheric pressure, represent noise whose amplitude may exceed those expected from small tectonic deformations [42,55,56].

At our three long-standing sites, OBP4, OBP5 and OBP7, a comparison between filtered pressure for different high-pass periods, T, and temperature (Fig. S7c) shows that a significant correlation exists only at the shallowest site, OBP5, at 973 m depth (i.e., maximum correlation coefficient (cc) of 0.44 around T = 35 days) (Fig. S7a). The time lag that maximizes correlation in that site is 12 days (with delayed temperature) but ranges between 9 and 14 days for $10 < T < 60$ days (Fig. S7b). In contrast, on the deepest sites OBP4 (2,374 m depth) and OBP7 (4,992 m depth), the maximum cc is below 0.31 for all cutoff periods and the associated lags around 18 and 150 days, respectively. Thus, for the following analysis, we correct the pressure data at OBP5 only by subtracting the scaled temperature with the time lag that maximizes cc [43], where the scaling factor is the quotient between the RMS of the pressure and the temperature. Fig. S8 illustrates how important the temperature correction is at OBP5 relative to the reference site OBP7 on the incoming Cocos plate. Corrected signals (right column) are very consistent regardless of the frequency band and significantly less noisy in long periods. Additionally, as discussed later, the data local trends in the corrected signals are much more consistent in time and space with seafloor tilt and GNSS observations.

4.3. Tilt mechanical amplifier model

Fig. 5a shows a two-dimensional free-body diagram of a tilted unit seated upon marine sediments. The exact technical specifications and dimensions of the units are given in Fig. S10 and Table S1. Assuming a rigid basement and tripod, to find forces $F_1(\alpha)$ and $F_2(\alpha)$ during the quasi-static instrument tilt we first assume that angular moments from all existing forces vanish. Equilibrium of angular moments with respect to the feet of leg 1 and leg 2 reads

$$\sum M_{F_1} = W\frac{L}{2}\cos\alpha - Wh\cdot\sin\alpha - F_{1N}\cdot L = 0$$

$$\Longrightarrow F_{1N} = W\cdot A_1 \tag{1}$$

and

$$\sum M_{F_2} = -W\frac{L}{2}\cos\alpha - Wh\cdot\sin\alpha + F_{2N}\cdot L = 0$$

$$\Longrightarrow F_{2N} = W\cdot A_2, \tag{2}$$

respectively, where

$$A_1 = \frac{1}{2}\cos\alpha - \frac{h}{L}\sin\alpha$$

and

$$A_2 = \frac{1}{2}\cos\alpha + \frac{h}{L}\sin\alpha.$$

If we neglect basement deformations between legs in the *x*-axis direction (i.e., strain tensor component $e_{xx} = 0$, which implies constant displacement u_x) and thus assume that tangential forces in both feet are given by Amonton's law,

$$F_T = \mu F_N, \tag{3}$$

where μ is the friction static coefficient, the equilibrium of forces in the *x*-axis direction reads

$$\sum F_x = \mu(F_{1N} + F_{2N}) - W \cdot \sin\alpha = 0.$$

Arranging terms after substitution of (1) and (2) yields

$$W(\mu \cdot \cos\alpha - \sin\alpha) = 0$$

$$\mu = \tan\alpha. \tag{4}$$

Magnitude of force F_i, where $i \in [1,2]$, is given by

$$|F_i(\alpha)| = \sqrt{F_{iT}^2 + F_{iN}^2}$$

so that, equations (1), (2), (3) and (4) lead to the general expressions for both legs' forces

$$|F_i(\alpha)| = W A_i \sqrt{1 - \tan\alpha^2},$$

which simply reduces to

$$|F_i(\alpha)| = W\left(0.5 \pm \frac{h}{L}\tan\alpha\right), \tag{5}$$

where $i = [1,2]$ stands for leg 1 and addition, or leg 2 and subtraction, α for the basement (i.e., tectonic) tilt, W for the unit net weight under the water, h for the height of the glass sphere and L for the leg aperture at the basement. Since the expected tilt during an SSE is small (i.e., tens of micro-radians so that $\tan\alpha \approx \alpha$), Equations 5 are linear. As expected, for $\alpha = 0$ (horizontality), each force is half the Fetch Unit net weight in water, and for $\alpha = \theta = \mathrm{atan}(L/2h)$ (see Fig. 5a), F_1 = W and $F_2 = 0$.

Thus, for small α both forces are linear functions of tilt with opposite signs. This means that a tilt increment implies an increment of F1 and a decrement of F2 of the same magnitude. Considering the mass and buoyancy of all unit components, the net total weight W is 402.2 Nw (Table S1).

Given the leg-foot surfaces of 0.108 m^2, the unit would exert an initial pressure P_0 of 1.862 kPa on each leg for $\alpha = 0$ (horizontal case). However, since the actual tripod is three-dimensional (i.e., it has three legs; Fig. S10b) and tilt can be at any azimuth, to mitigate the two-dimensional simplification we multiply the forces by a factor of 2/3 in subsequent analysis.

Deepwater marine sediments are highly compressible [57,58,78]. Under a quasi-static load, their volume undergoes large changes due to fluid drainage and particle consolidation. One way of quantifying this is by estimating the distribution of vertical stresses across the sediment column and then the corresponding settlement. Boussinesq[79] introduced a model describing the vertical stress in a soil produced by a distributed circular load on top of it, which reads

$$\Delta\sigma_z = q\left[1 - \left(\frac{1}{1+(r_0/z)^2}\right)^{3/2}\right], \tag{6}$$

where q is the load pressure, r_0 is the radius of the load and z is depth. In our case, $r_0 = 0.1854\ m$ (deduced from Table S1) and $q = P_0 = 1.862 \times \frac{2}{3} = 1.242$ kPa on each leg for $\alpha = 0$ μrad. The blue curve of Fig. S11a depicts the corresponding $\Delta\sigma_z$ as a function of depth. The total stress, σ_{tot}, will be the sum of $\Delta\sigma_z$ and the effective vertical stress, σ_{eff} or γ, which grows linearly with depth and ranges between 2.5-10.2 kPa/m in deep, water-saturated seabed clay samples [57]. The black and red curves in that figure show σ_{eff} and σ_{tot}, respectively, assuming the average value γ = 5 kPa/m reported by Davie et al.[57]

As a first-order approximation, the settlement (i.e., the normal surface displacement due to sediment consolidation) of a water-saturated layer with thickness H_0 may be estimated as [80]

$$\delta = C_c \frac{H_0}{1 + e_0} \log\frac{\sigma_{tot}}{\sigma_{eff}}, \tag{7}$$

where C_c is the sediments compressibility index and e_0 the associated void ratio. Consolidation tests on different types of marine sediments from the Gulf of Mexico (GM) and the Pacific Ocean (PO) indicate that C_c may vary significantly, ranging within 0.25-0.7 for terrigenous clays, within 0.66-1.2 for diatom-rich terrigenous clays and within 1.7-1.82 for hemipelagic and pelagic clays [57,58]. Values for e_0 determined by these authors range between 0.7-1.7 and 3.5-6.0 for the first and third kinds of clays, respectively. The larger C_c and the smaller e_0, the higher the settlement will be. Given a depth discretization of n thin layers with thickness $H_0 = \Delta z$, we can estimate the settlement δ at any depth z by integrating Eq. 7 for layers deeper than or equal to z. Our long-record Fetch units are settled at ~1,000 m (OBO5 and OBO8, continental slope), 2,374 m (OBO4, nearby continental rise), and 4,992 m (OBO7, abyssal plain) depth, so they were likely on top of different kinds of clays. However, since we do not have any information on the actual properties of sediments at each OBO site, to illustrate the procedure we set $C_c = 1.1$ and $e_0 = 4.2$, which are not extreme values and thus lead to conservative estimates.

Fig. S11b shows the settlement associated with the stress condition of Fig. S11a. Equations 6 and 7 involve non-linear functions and, as a result, settlement decreases rapidly with depth, being 35.2 mm at the surface and about an order of magnitude less at 0.5 m depth. This estimate corresponds

to the initial load $q = P_0$ under each unit leg for $\alpha = 0$ μrad (horizontal case). In the absence of sediments, Eq. 1 predicts linear differential increments of the legs' pressure with tilt. However, once the basement begins to tilt (i.e., for $\alpha \neq 0$ in Eq. 1), the differential pressure upon the sediments induces differential settlements that are non-linear functions of the evolving Boussinesq stress (Eq. 6) and settlement (Eq. 7). This means that the tectonic tilt is no longer linearly related to the pressure of the legs acting upon the sediments. Because of suction effects on leg 2 where the pressure decreases, in the following, we assume that no displacement occurs there so that the settlement-induced tilt, α_s, will be only due to consolidation beneath leg 1, where pressure increases. Furthermore, since we are interested in slow tectonic deformations that may last from weeks to several months, we also assume that settlement evolves quasi-statically, which means that any fluid drainage/diffusion effects occurring on smaller time scales are neglected. This also implies that possible restoring processes in the sediments associated with suction effects where pressure decreases are not considered. Although beyond the scope of this study, the evaluation of these processes may be important because they could demonstrate the long-term viability of TMAs on the ocean floor.

To quantify the evolution of α_{tot}, the effective instrument tilt within the glass sphere, as the basement tilts, we solve iteratively for δ as α increases linearly from 0 to 2.5 μrad with steps $\Delta\alpha$ = 0.03 μrad. This means that for every *i*-th α step we (1) use α_{tot}^{i} to estimate pressure P_1 on leg 1 (Eq. 5), (2) estimate the incremental pressure $\Delta P = P_1 - P_0$, (3) estimate the incremental total stress $\Delta\sigma_{tot}^{i}$ from ΔP (Eq. 6), (4) estimate the incremental settlement $\Delta\delta^{i}$ from $\Delta\sigma_{tot}^{i}$ (Eq. 7), (5) estimate the incremental settlement-induce tilt $\Delta\alpha_s^{i}$ as $\arctan(\Delta\delta^{i})$ (because L = 1 m, Table S1), and (6) update the effective instrument tilt as $\alpha_{tot}^{i+1} = \alpha_{tot}^{i} + \Delta\alpha + \Delta\alpha_s^{i}$ before stepping forward.

4.4. Tilt data analysis

As previously described by Villafuerte et al.[52] for the treatment of GNSS time series, the right column of Fig. S12 presents the tilt data set after the removal of outliers exceeding ±1.5σ of the mean difference with a locally weighted second-order polynomial regression (red curves) with a moving support of 250 samples. This procedure is important to accurately determine the sensors' orientation and does not affect the general data trends. Note that regressions were run independently on every earthquake-bounded segment so that tilt discontinuities produced by the events could be seen.

Except for OBT4, which is seated on the North American plate about 9 km from the oceanic trench, the time series show a clear long-term trend. Besides, they all show month-long transient variations most time-correlated with the previously documented 2018 and 2019 long-term SSEs in Guerrero [33] and the 2021-2022 events. To assess the origin of these variations, we first compared both tilt components in the three long-recording sites with collocated temperatures (Fig. S13a) and hydrostatic pressure (Fig. S13b) for different period bandwidths. As for the pressure-temperature analysis, to quantify the correlation between the observables, we (1) detrended the tilt data, (2) normalized the temperature and pressure so that their RMS is equal to the tilt's time series, and (3) search for the moveouts maximizing the correlation coefficients (cc). The lack of similarity between the tilt and pressure/temperature time series is quantitatively confirmed (Fig. S13c) with cc less than 0.16 in all cases except for pressure in OBT7, where it reaches an average of ~0.27, well below the correlation found between pressure and temperature in OBP5 (Fig. S7). These

results are somehow expected because the tiltmeters are isolated from the water within the glass sphere and point towards a possible link between the tilt variations and tectonic activity. Another possible origin of the variations could be local soil settlements and/or landslides. However, as shown later, most of them are correlated in time between sites more than 20 km apart, which rules out these hypotheses in those cases.

To estimate the orientation of the tiltmeters, for the 3.5-year data windows between February 17, 2018, and September 7, 2021, we assumed that the first eigenvector of the data covariance matrix at each site is parallel to the plate convergence with respect to North America (according to the NUVEL-1A model[60]), which has an azimuth of 35.5° from the North on the Middle America trench at the traverse of Acapulco. This hypothesis is important because it implies that the long-term data trends are driven by the secular deformation of the crust produced by the subduction of the Cocos plate underneath the continent. It is noteworthy that tests with significantly shorter windows (i.e., of several months) yielded reasonable results if chosen during quiescent periods. In the case of OBT8, which is located 26 km offshore of Acapulco and has a much shorter record with large time variations, the sensor orientation becomes more difficult. This site was deployed on April 3, 2022, only seven months after the Mw7.0 Acapulco earthquake and during the subsequent SSE in Guerrero discussed later. Thus, the site was likely tilting fast because of the nearby rupture after-slip and/or the SSE. We tried different baseline windows looking for correlations with the closest GNSS site ACAP, where the north component changed its trend from April 2022 (Fig. 4a), and found the baseline from April 2 to June 1, 2022, the most reasonable choice for the principal component decomposition. However, we do not have strong arguments to validate the sensor orientation at this site, so the data should be treated with caution for interpretation. Another uncertainty in the general procedure is the actual sign of the eigenvectors. Since we do not have any information about the instrument landing orientations, the first eigenvector could have either sign. For this reason, as detailed below, we used theoretical tilt predictions for an inter-SSE deformation period to attribute the signs.

Fig. S14a (left column) shows the baseline tilt components as a function of time at each site along with the two associated eigenvectors. The eigenvector with the largest eigenvalue, P_1, corresponds to the direction that maximizes the baseline tilt rate. Assuming that this direction corresponds to the plate convergence, then we can simply decompose the whole time series into North and East geographic components, as shown in Fig. S14b (right column). One of the most prominent features in the geographically referenced signals is the eastward tilt jump at station OBT5 due to the Acapulco earthquake (see Fig. 2a). Fig. S15 shows the tilt components in the plate convergence (P_l) and its perpendicular (P_{lp}) directions along with linear regressions indicating the long-term rates (except for OBT8, where there is no long-term data). Notice that tilt rates in the P_l direction at OBT5 and OBT7 are opposite signs because the former lies on the overriding plate and the latter on the subducting Cocos plate. While station OBT4 close to the trench is stable in both components, tilt rates in the P_l direction are much higher in the other three sites, with absolute values ranging from ~400 to ~2,000 μrad/yr. As expected, due to the sediment-induced tilt amplification, these values are extremely high when compared with known secular deformations of the crust in subduction margins [45,46].

4.5. Inter-SSE plate interface coupling inversion

For the inversion of the inter-SSE coupling from GNSS displacement data, the interface was discretized with 5 km subfaults. Furthermore, a von Karman correlation length of 30 km with a Hurst exponent of 0.75 was assumed. An advantage for the inversion of geodetic data from the Mexican subduction zone compared to Northen Japan and Chile, where the oceanic trench is more than 120 km from the coast, is the proximity that separates them in Guerrero of only ~65 km. This allows remarkably high interplate slip resolution offshore even in the absence of ocean-bottom instruments. Fig. S16 shows the result of mobile checkerboard (MOC) tests [51] for three different checker unit sizes (h, top panels) considering the 3D interface geometry introduced by Cruz-Atienza et al. [33]. The number of checkerboard inversions for each MOC ranged between 18 and 32 depending on h. The second and third rows of the figure display the median restitution indexes (MRI)[51] excluding and including the vertical displacements at the OBPs (i.e., at OBP4 and OBP5), respectively. In the worst-case scenario where OBPs were excluded for the smallest h = 40 km (left column), MRIs are close to 0.7 at the oceanic trench within the GGap. This means that our slip (coupling or SSEs) solutions should have a nominal error below ~30% as compared to the actual slip for patches larger than or equal to 40 km from the oceanic trench up to an interface depth of about 40 km. For larger h equal to 60 km and 80 km (middle and right columns), MRI raises to 0.75 and 0.8 at the trench with no OBPs, and above 0.85 in the best-case scenario for h = 80 km including OBPs.

4.6. Tilt and displacement joint inversion

ELADIN addresses regularization by iteratively projecting the problem solution into a physically-consistent and spectrally bounded space determined by the von Karman correlation function [51]. The spectral bounds are thus defined by both the Hurst exponent and the correlation length of that function. Well-balanced solutions will also depend on the relative data weights that we systematically explored. Fig. S17 shows three checkboard inversions without added noise considering a correlation length of 30 km, a Hurst exponent of 0.75 (both optimal values determined from the MOC tests, Fig. S16) and a data weighting that depends on precision matrices derived from each data set (i.e., GNSS/OBP and Tilt). Precision is a data-driven metric incorporated into the ELADIN formalism to penalize unreliable observations and corresponds to the inverse of the data covariance [51]. In practice, given the independently determined precision matrices for displacement and tilt, which varies between zero and one and thus implies a data weak normalization, we found that a relative average weight of 12.1 between both matrices, being larger the displacement matrix, yields reasonable and stable results. This means that tilt remarkable sensitivity to slip should be compensated to allow displacement illumination of the plate interface across larger wavenumbers. Another consideration for properly balancing the inversions is to set all data in units producing magnitudes of the same order, i.e., displacement in centimeters and tilt in microradians. The checkerboard inversions in Fig. S17, whose target model intentionally includes slip at the trench (panel a), were obtained following this strategy for GNSS data alone (panel b), for GNSS and OBP data (panel c), and jointly for GNSS, OBP and tilt data (panel d). While the three tests resolve similarly well the slip distribution onshore, only the inversion including tilt is able to retrieve the target model up to the oceanic trench. It is important to note that the relative weight between displacement and tilt is particularly important and should probably depend on the tectonic context and/or the inversion formal strategy used.

The left column of Fig. S18 shows the joint inversion and model data fit of GNSS, OBP and tilt observations for the 10 windows (yellow dots in Figs. 4a and 7a) carefully selected based on the behavior of data from June 24, 2020 to September 18, 2022. During those 2.2 years surrounding the Mw7.0 Acapulco earthquake, several remarkable events took place. Note that the first 6-month window correspond to a rather quiescent inter-SSE period. To better appreciate the events, we time interpolated the solutions every 10 days by means of piecewise cubic Hermite interpolating polynomials (PCHIP) which honors the target function when providing a more physically-consistent picture of slip (e.g., its acceleration) than simple piecewise linear regressions. We stress that no significant change in the interpretation of the solutions depends on our chosen interpolant.

4.7. Template matching analysis

The Template Matching (TM) technique we used was introduced by Liu et al.[64]. The technique was applied over 3-year-long continuous records at 8 broadband seismic stations distributed in Guerrero (inset in Fig. 1) from January 1, 2020 to December 31, 2022. The templates correspond to waveforms of 4,876 earthquakes reported by the SSN in the same period. TM performs a continuous search by computing the correlation coefficient between the templates and the data at each sample step. A detection is declared when the stacked correlation coefficient for the three components of five stations exceeds *n* times the mean average deviation (MAD) of the correlation coefficient for each day. Since the study region is large (i.e., more than 300 km along the coast), the search was divided in two sectors with five stations each and an overlap between them (Fig. S20a). By visually inspecting the detections for different MAD threshold values, we empirically determined that MAD $\geq$ 15 provides a robust and reliable catalog with 38,501 earthquakes (Fig. S20c). Representative examples of waveforms matches are shown in Fig. S21 along with the associated MAD values. Following Liu et al.[64], the magnitude of the detections was estimated by comparing the median of the relative amplitude between the peak values of the template and the detection. The maximum curvature criterion of the Gutenberg-Richter distribution leads to a completeness magnitude Mc = 3.1 (Fig. S20b). The location of each detection was attributed following a three-dimensional normal distribution centered at the template location with a standard deviation of 0.03^{o} horizontally and 3 km in depth, so that most of detections from a single template lie within a spheroidal region with ~7 km radius (i.e., 2σ).

4.8. Background seismicity baseline

To establish the background seismicity baseline, the seismic catalog was spatially discretized on a regular grid of 15 km per side (Fig. S20c) to estimate temporal linear regressions in each bin of the grid. To loosely guarantee the completeness of the catalog, only earthquakes with magnitude greater than or equal to 3.2 were considered. Fig. S23a shows the baseline determined along with the region where the regressions have an adjusted R-square value greater than 95%, derived from the spatial distribution of that metric shown in Fig. S23b. That is, the region where the linear model is reasonably representative of the background seismicity rate. To illustrate the validity of the approach, Figs. S23c and d show the earthquake cumulative counts along with the baseline linear models at five selected sites as well as in a 20-km-radius region around the hypocenter of the Acapulco earthquake, respectively. To estimate seismicity rate deviations from the baseline between April 1, 2021 and September 18, 2022, the period following the tectonic quiescence, a temporal scan of the catalog was performed in 10-day increments to subtract the baseline from the

rate determined per window in each bin. The evolution of the seismicity rate deviations is shown in Movie S2 along with the slow slip contours and the occurrence of repeating earthquakes.

4.9. Coulomb failure stress and seismicity rate

The CFS associated with each individual slip inversion (Fig. S18) was interpolated every 10 days in the same manner as done for the slip (Movie S1). Fig. S24b-d compare the seismicity rate time series with the slip rate (left column) and CFS rate (right column) time series, averaged over three circular regions R1, R2, and R3 with a radius of 20 km (Fig. S24a), a length that corresponds to the characteristic asperity size resolved above 80% in our near-shore slip inversions (see Fig. S16 left column). The top panels show the cross-correlation coefficient (cc) as a function of time for the associated time series below using a wavelet decomposition approach [68].

5. References

1. Aoi, S. *et al.* MOWLAS: NIED observation network for earthquake, tsunami and volcano. *Earth, Planets and Space 2020 72:1* **72**, 1–31 (2020).
2. Ito, Y. *et al.* Episodic slow slip events in the Japan subduction zone before the 2011 Tohoku-Oki earthquake. *Tectonophysics* **600**, 14–26 (2013).
3. Davis, E. E., Villinger, H. & Sun, T. Slow and delayed deformation and uplift of the outermost subduction prism following ETS and seismogenic slip events beneath Nicoya Peninsula, Costa Rica. *Earth Planet Sci Lett* **410**, 117–127 (2015).
4. Wallace, L. M. *et al.* Slow slip near the trench at the Hikurangi subduction zone, New Zealand. *Science (1979)* **352**, 701–704 (2016).
5. Cruz-Atienza, V. M. *et al.* A seismogeodetic amphibious network in the Guerrero Seismic Gap, Mexico. *Seismological Research Letters* **89**, (2018).
6. Fredrickson, E. K. *et al.* Optimizing sensor configurations for the detection of slow-slip earthquakes in seafloor pressure records, using the Cascadia Subduction Zone as a case study. *J Geophys Res Solid Earth* **124**, 13504–13531 (2019).
7. Barcheck, G. *et al.* The Alaska Amphibious Community Seismic Experiment. *Seismological Research Letters* **91**, 3054–3063 (2020).
8. Tréhu, A. M. *et al.* Post-seismic response of the outer accretionary prism after the 2010 Maule earthquake, Chile. *Geosphere* **16**, 13–32 (2020).
9. Rogers, G. & Dragert, H. Episodic tremor and slip on the Cascadia subduction zone: The chatter of silent slip. *Science (1979)* **300**, 1942–1943 (2003).
10. Obara, K., Hirose, H., Yamamizu, F. & Kasahara, K. Episodic slow slip events accompanied by non-volcanic tremors in southwest Japan subduction zone. *Geophys Res Lett* **31**, 1–4 (2004).
11. Schwartz, S. Y. & Rokosky, J. M. Slow slip events and seismic tremor at circum-pacific subduction zones. *Reviews of Geophysics* **45**, (2007).
12. Ito, Y., Obara, K., Shiomi, K., Sekine, S. & Hirose, H. Slow earthquakes coincident with episodic tremors and slow slip events. *Science (1979)* **315**, 503–506 (2007).
13. Yamashita, Y. *et al.* Migrating tremor off southern Kyushu as evidence for slow slip of a shallow subduction interface. *Science (1979)* **348**, 676–679 (2015).
14. Ide, S. Variety and spatial heterogeneity of tectonic tremor worldwide. *J Geophys Res Solid Earth* **117**, (2012).
15. Villafuerte, C. & Cruz-Atienza, V. M. Insights into the causal relationship between slow slip and tectonic tremor in Guerrero, Mexico. *J Geophys Res Solid Earth* **122**, 6642–6656 (2017).
16. Kostoglodov, V. *et al.* The 2006 slow slip event and nonvolcanic tremor in the Mexican subduction zone. *Geophys Res Lett* **37**, (2010).
17. Houston, H. Low friction and fault weakening revealed by rising sensitivity of tremor to tidal stress. *Nat. Geosci.* **8**, 409–415 (2015).
18. Hyndman, R. D., McCrory, P. A., Wech, A., Kao, H. & Ague, J. Cascadia subducting plate fluids channelled to fore-arc mantle corner: ETS and silica deposition. *J Geophys Res Solid Earth* **120**, 4344–4358 (2015).
19. Audet, P., Bostock, M. G., Christensen, N. I. & Peacock, S. M. Seismic evidence for overpressured subducted oceanic crust and megathrust fault sealing. *Nature* **457**, 76–78 (2009).

20. Warren-Smith, E. *et al.* Episodic stress and fluid pressure cycling in subducting oceanic crust during slow slip. *Nat. Geosci.* **12**, 475–481 (2019).
21. Cruz-Atienza, V. M., Villafuerte, C. & Bhat, H. S. Rapid tremor migration and pore-pressure waves in subduction zones. *Nat Commun* **9**, (2018).
22. Plata-Martinez, R. *et al.* Shallow slow earthquakes to decipher future catastrophic earthquakes in the Guerrero seismic gap. *Nat Commun* **12**, (2021).
23. Nishikawa, T. *et al.* The slow earthquake spectrum in the Japan Trench illuminated by the S-net seafloor observatories. *Science (1979)* **365**, 808–813 (2019).
24. Nishimura, T., Yokota, Y., Tadokoro, K. & Ochi, T. Strain partitioning and interplate coupling along the northern margin of the Philippine Sea plate, estimated from Global Navigation Satellite System and Global Positioning System-Acoustic data. *Geosphere* **14**, 535–551 (2018).
25. Radiguet, M. *et al.* Slow slip events and strain accumulation in the Guerrero gap, Mexico. *J Geophys Res Solid Earth* **117**, (2012).
26. Kostoglodov, V. *et al.* A large silent earthquake in the Guerrero seismic gap, Mexico. *Geophys Res Lett* **30**, (2003).
27. Singh, S. K., Astiz, L. & Havskov, J. Seismic gaps and recurrence periods of large earthquakes along the Mexican subduction zone: A reexamination. *Bulletin of the Seismological Society of America* **71**, 827–843 (1981).
28. UNAM Seismology Group. Papanoa, Mexico earthquake of 18 April 2014 (Mw7.3). *Geofisica Internacional* **54**, 363–386 (2015).
29. Kanamori, H., Jennings, P. C., Singh, S. K. & Astiz, L. Estimation of strong ground motions in Mexico City expected for large earthquakes in the Guerrero seismic gap. *Bulletin - Seismological Society of America* **83**, 811–829 (1993).
30. UNAM Seismology Group. The September 1985 Michoacan earthquakes: aftershock distribution and history of rupture. *Geophys Res Lett* **13**, 573–576 (1986).
31. Kato, A. *et al.* Propagation of slow slip leading up to the 2011 M(w) 9.0 Tohoku-Oki earthquake. *Science (1979)* **335**, 705–708 (2012).
32. Ruiz, S. *et al.* Intense foreshocks and a slow slip event preceded the 2014 Iquique Mw 8.1 earthquake. *Science (1979)* **345**, 1165–1169 (2014).
33. Cruz-Atienza, V. M. *et al.* Short-term interaction between silent and devastating earthquakes in Mexico. *Nat Commun* **12**, (2021).
34. Radiguet, M. *et al.* Triggering of the 2014 Mw7.3 Papanoa earthquake by a slow slip event in Guerrero, Mexico. *Nat. Geosci.* **9**, 829–833 (2016).
35. Spiess, F. N. *et al.* Precise GPS/Acoustic positioning of seafloor reference points for tectonic studies. *Physics of the Earth and Planetary Interiors* **108**, 101–112 (1998).
36. Matsumoto, Y. *et al.* Undersea co-seismic crustal movements associated with the 2005 Off Miyagi Prefecture Earthquake detected by GPS/acoustic seafloor geodetic observation. *Earth, Planets and Space* **58**, 1573–1576 (2006).
37. Cruz-Atienza, V. M. *et al.* A seismogeodetic amphibious network in the Guerrero Seismic Gap, Mexico. *Seismological Research Letters* **89**, 1435–1449 (2018).
38. Foster, J. H., Ericksen, T. L. & Bingham, B. Wave Glider–Enhanced Vertical Seafloor Geodesy. *J Atmos Ocean Technol* **37**, 417–427 (2020).
39. Chadwell, C. D. *et al.* Expansion of GPS-Acoustic Arrays offshore the Cascadia and Alaska Subduction Zones. *AGUFM* **2018**, T44C-02 (2018).
40. Suzuki, K. *et al.* Synchronous changes in the seismicity rate and ocean-bottom hydrostatic pressures along the Nankai trough: A possible slow slip event detected by the Dense

Oceanfloor Network system for Earthquakes and Tsunamis (DONET). *Tectonophysics* **680**, 90–98 (2016).
41. Polster, A., Fabian, M. & Villinger, H. Effective resolution and drift of paroscientific pressure sensors derived from long-term seafloor measurements. *Geochemistry, Geophysics, Geosystems* **10**, (2009).
42. Hino, R., Kubota, T., Chikasada, N. Y., Ohta, Y. & Otsuka, H. Assessment of S-net seafloor pressure data quality in view of seafloor geodesy. *Prog Earth Planet Sci* **9**, 1–18 (2022).
43. Gomberg, J., Hautala, S., Johnson, P. & Chiswell, S. Separating Sea and Slow Slip Signals on the Seafloor. *J Geophys Res Solid Earth* **124**, 13486–13503 (2019).
44. He, B., Wei, M., Watts, D. R. & Shen, Y. Detecting Slow Slip Events From Seafloor Pressure Data Using Machine Learning. *Geophys Res Lett* **47**, e2020GL087579 (2020).
45. Boudin, F. *et al.* Slow slip events precursory to the 2014 Iquique Earthquake, revisited with long-base tilt and GPS records. *Geophys J Int* **228**, 2092–2121 (2021).
46. Tsuji, S. *et al.* Precise tilt measurement by seafloor borehole tiltmeters at the Nankai Trough subduction zone. *Earth, Planets and Space* **75**, 1–14 (2023).
47. Shiobara, H., Ito, A., Sugioka, H., Shinohara, M. & Sato, T. Tilt Observations at the Seafloor by Mobile Ocean Bottom Seismometers. *Front Earth Sci (Lausanne)* **8**, (2021).
48. Iglesias, A. *et al.* A Source Study of the Mw 7.0 Acapulco, Mexico, Earthquake of 8 September 2021. *Seismological Research Letters* **93**, 3205–3218 (2022).
49. Melgar, D., Ruiz-Angulo, A., Crowell, B. W., Fielding, E. J. & Solano-Hernandez, E. A. The Mechanisms of Tsunami Amplification and the Earthquake Source of the 2021 M 7 Acapulco, Mexico, Earthquake. *Bulletin of the Seismological Society of America* **112**, 2902–2914 (2022).
50. Gao, H., Liao, M. & Feng, G. An improved quadtree sampling method for insar seismic deformation inversion. *Remote Sens (Basel)* **13**, 1678 (2021).
51. Tago, J. *et al.* Adjoint slip inversion under a constrained optimization framework: Revisiting the 2006 Guerrero slow slip event. *Geophys J Int* **226**, (2021).
52. Villafuerte, C. *et al.* Slow slip events and megathrust coupling changes contributed to the earthquake potential in Oaxaca, Mexico. *Authorea Preprints* (2024) doi:10.22541/ESSOAR.172987685.53574342/V1.
53. Singh, S. K., Corona-Fernandez, R. D., Santoyo, M. Á. & Iglesias, A. Repeating Large Earthquakes along the Mexican Subduction Zone. *Seismological Research Letters* **95**, 458–478 (2024).
54. Graham, S. E. *et al.* GPS constraints on the 2011-2012 Oaxaca slow slip event that preceded the 2012 March 20 Ometepec earthquake, southern Mexico. *Geophys J Int* **197**, 1593–1607 (2014).
55. Dobashi, Y. & Inazu, D. Improving Detectability of Seafloor Deformation From Bottom Pressure Observations Using Numerical Ocean Models. *Front Earth Sci (Lausanne)* **8**, (2021).
56. Fredrickson, E. K. *et al.* Slow Slip Detectability in Seafloor Pressure Records Offshore Alaska. *J Geophys Res Solid Earth* **128**, (2023).
57. Davie, J. R., Fenske, C. W. & Serocki, S. T. Geotechnical properties of deep continental margin soils. *Marine Georesources & Geotechnology* **3**, 85–119 (1978).
58. Hampton, M. A. Geotechnical properties of sediment on the Kodiak continental shelf and upper slope, gulf of Alaska. *Marine Georesources & Geotechnology* **8**, 159–180 (1989).

59. Okada, Y. Surface deformation due to shear and tensile faults in a half-space. *Bulletin of the Seismological Society of America* **75**, 1135–1154 (1985).
60. DeMets, C., Gordon, R. G., Argus, D. F. & Stein, S. Effect of recent revisions to the geomagnetic reversal time scale on estimates of current plate motions. *Geophys Res Lett* **21**, 2191–2194 (1994).
61. Frank, W. B. *et al.* The evolving interaction of low-frequency earthquakes during transient slip. *Sci Adv* **2**, (2016).
62. Yamashita, Y., Shimizu, H. & Goto, K. Small repeating earthquake activity, interplate quasi-static slip, and interplate coupling in the Hyuga-nada, southwestern Japan subduction zone. *Geophys Res Lett* **39**, (2012).
63. Kato, A. & Ben-Zion, Y. The generation of large earthquakes. *Nature Reviews Earth & Environment 2020 2:1* **2**, 26–39 (2020).
64. Liu, M., Li, H., Zhang, M. & Wang, T. Graphics Processing Unit-Based Match and Locate (GPU-M&L): An Improved Match and Locate Method and Its Application. *Seismological Research Letters* **91**, 1019–1029 (2020).
65. Dominguez, L. A. *et al.* Interplate Slip Rate Variation Between Closely Spaced Earthquakes in Southern Mexico: The 2012 Ometepec and 2018 Pinotepa Nacional Thrust Events. *J Geophys Res Solid Earth* **127**, (2022).
66. Uchida, N., Iinuma, T., Nadeau, R. M., Bürgmann, R. & Hino, R. Periodic slow slip triggers megathrust zone earthquakes in northeastern Japan. *Science (1979)* **351**, 488–492 (2016).
67. Nikkhoo, M. & Walter, T. R. Triangular dislocation: an analytical, artefact-free solution. *Geophys J Int* **201**, 1119–1141 (2015).
68. Cooper, G. R. J. & Cowan, D. R. Comparing time series using wavelet-based semblance analysis. *Comput Geosci* **34**, 95–102 (2008).
69. Kaneko, Y., Nielsen, S. B. & Carpenter, B. M. The onset of laboratory earthquakes explained by nucleating rupture on a rate-and-state fault. *J Geophys Res Solid Earth* **121**, 6071–6091 (2016).
70. Cattania, C. & Segall, P. Precursory Slow Slip and Foreshocks on Rough Faults. *J Geophys Res Solid Earth* **126**, e2020JB020430 (2021).
71. Kato, A. & Nakagawa, S. Multiple slow-slip events during a foreshock sequence of the 2014 Iquique, Chile Mw 8.1 earthquake. *Geophys Res Lett* **41**, 5420–5427 (2014).
72. Socquet, A. *et al.* An 8 month slow slip event triggers progressive nucleation of the 2014 Chile megathrust. *Geophys Res Lett* **44**, 4046–4053 (2017).
73. Singh, S. K. *et al.* Evidence of directivity during the earthquakes of 8 and 10 May 2014 (M w 6.5, 6.1) in the Guerrero, Mexico seismic gap and some implications. *J Seismol* **23**, 683–697 (2019).
74. Nocquet, J. M. *et al.* Supercycle at the Ecuadorian subduction zone revealed after the 2016 Pedernales earthquake. *Nature Geoscience 2017 10:2* **10**, 145–149 (2016).
75. Bouchon, M. *et al.* Potential slab deformation and plunge prior to the Tohoku, Iquique and Maule earthquakes. *Nature Geoscience 2016 9:5* **9**, 380–383 (2016).
76. Bedford, J. R. *et al.* Months-long thousand-kilometre-scale wobbling before great subduction earthquakes. *Nature 2020 580:7805* **580**, 628–635 (2020).
77. Panet, I., Bonvalot, S., Narteau, C., Remy, D. & Lemoine, J. M. Migrating pattern of deformation prior to the Tohoku-Oki earthquake revealed by GRACE data. *Nature Geoscience 2018 11:5* **11**, 367–373 (2018).

78. Hattab, M. & Favre, J. L. Analysis of the experimental compressibility of deep water marine sediments from the Gulf of Guinea. *Mar Pet Geol* **27**, 486–499 (2010).
79. Boussinesq, J. (1842-1929). A. du texte. Application des Potentiels a l'Etude de Ie l'Equilibre et du Mouvement des Solides Elastiques. *Gauthier-Villars* (1885).
80. Budhu, M. Soil mechanics fundamentals. *Wiley-Blackwell* 368 (2015).

6. Acknowledgments

We thank Chris Maron, Michel Campillo, Pascal Bernard, Léonard Seydoux and Tomoaki Nishikawa for enriching discussions. We also thank Ligia Pérez Cruz, the Oceanographic Platform Coordination of UNAM, and the crew of the B/O El Puma for all their support.

Funding:
Universidad Nacional Autónoma de México, PAPIIT grants IG100617, IG100921 and IN111524.
Universidad Nacional Autónoma de México, R/V El Puma grants GGAP2017-1, GGAP2017-2, GGAP2018-1, GGAP2018-2, GGAP2019, GGAP2020, GGAP2023 and GGAP2024.
The Japan Science and Technology Agency–Japan International Cooperation Science and Technology Research Partnership for Sustainable Development, SATREPS grant JPMJSA1510.

Author contributions:
Conceptualization and formal analysis: VMCA
Methodology: VMCA, JT, LAD
Investigation: VMCA, JT, LAD, VK, YI, EOS, TRN, RG, LR, AB, CV
Data processing: VMCA, LAD, SF, DS, PM, EK, FB
Visualization: VMCA, LAD, AB
Supervision: VMCA
Technical support: SF, JR, EK, AR, VMCA, YI
Writing—original draft: VMCA
Writing—review & editing: most of authors

Competing interests:
No competing interests

Data and materials availability:
Codes used for the analysis are available upon request. Seafloor pressure and tilt data are restricted until the end of 2028 due to confidentiality clauses of the SATREPS-UNAM project. GNSS data are restricted according to the data distribution policy of the National Seismological Service (SSN) and the Department of Seismology of the Institute of Geophysics, UNAM. Exceptions may be granted after discussion with project leaders as long as the motivation is to establish substantive scientific collaboration. Broadband seismological data are unrestricted and can be obtained on request from the SSN.

Science Advances
AAAS

This manuscript is under second review in Science Advances

Supplementary Materials for

Seafloor Geodesy Unveils Seismogenesis of Large Subduction Earthquakes in México

Víctor M. Cruz-Atienza* *et al*.

*Corresponding author. Email: cruz@igeofisica.unam.mx

This PDF file includes:

Figs. S1 to S24
Tables S1 to S2
Movies S1 to S2

Other Supplementary Materials for this manuscript include the following:

Movies S1 to S2

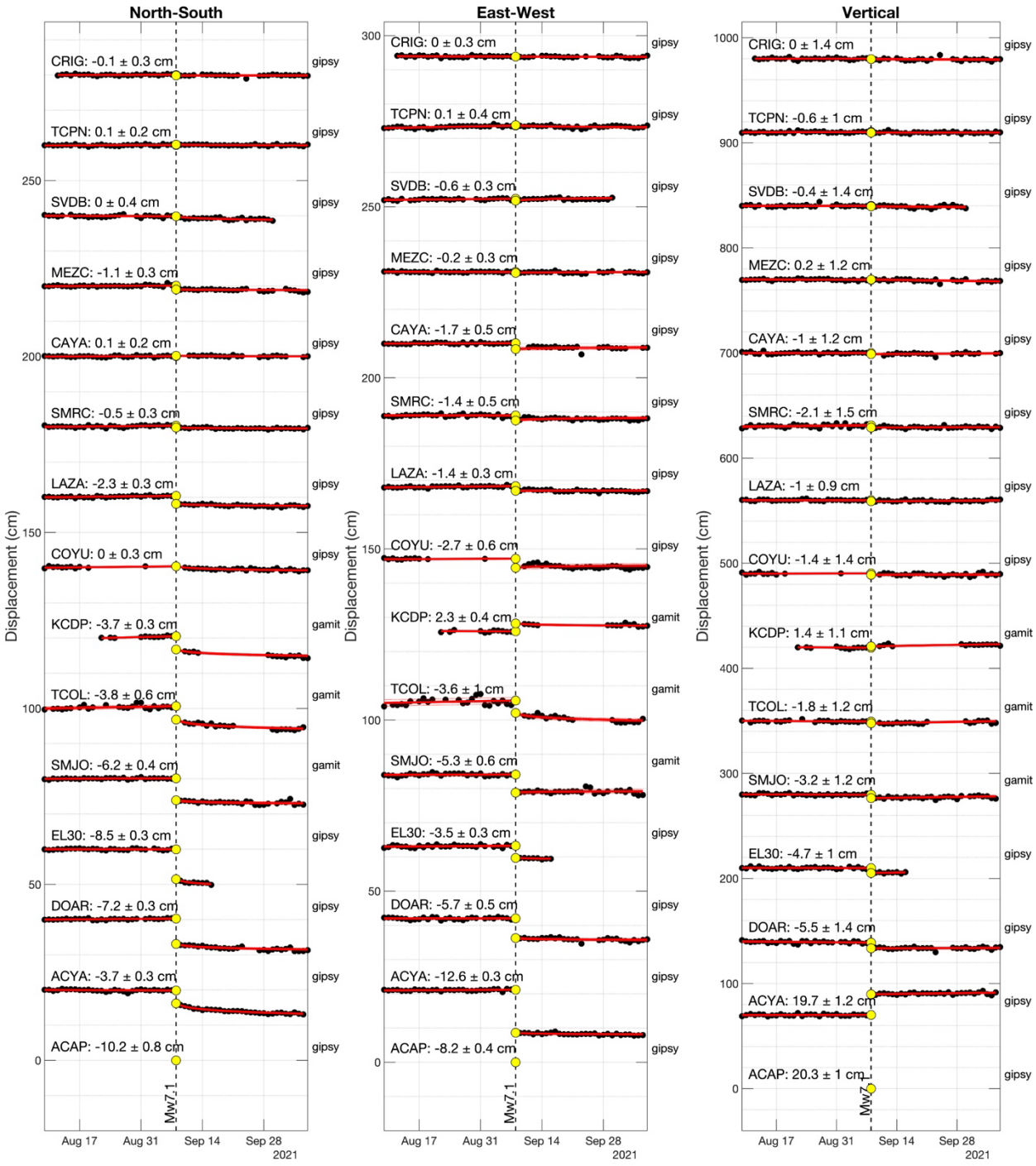

Fig. S1. Estimation of co-seismic displacements from GNSS data for the 2021 Acapulco earthquake. According to Villafuerte et al. (2024), the three-component displacements were estimated independently from one-day extrapolations of two regression functions before and after the earthquake. Before the earthquake we used linear regressions over 30-day-long windows, while after the earthquake, we used a logarithmic function of time of the form A + B log t to fit the data over 30-day-

long windows. For both regressions the day of the earthquake was excluded, and their corresponding values extrapolated. See Fig. S2 for estimates at station ACAP.

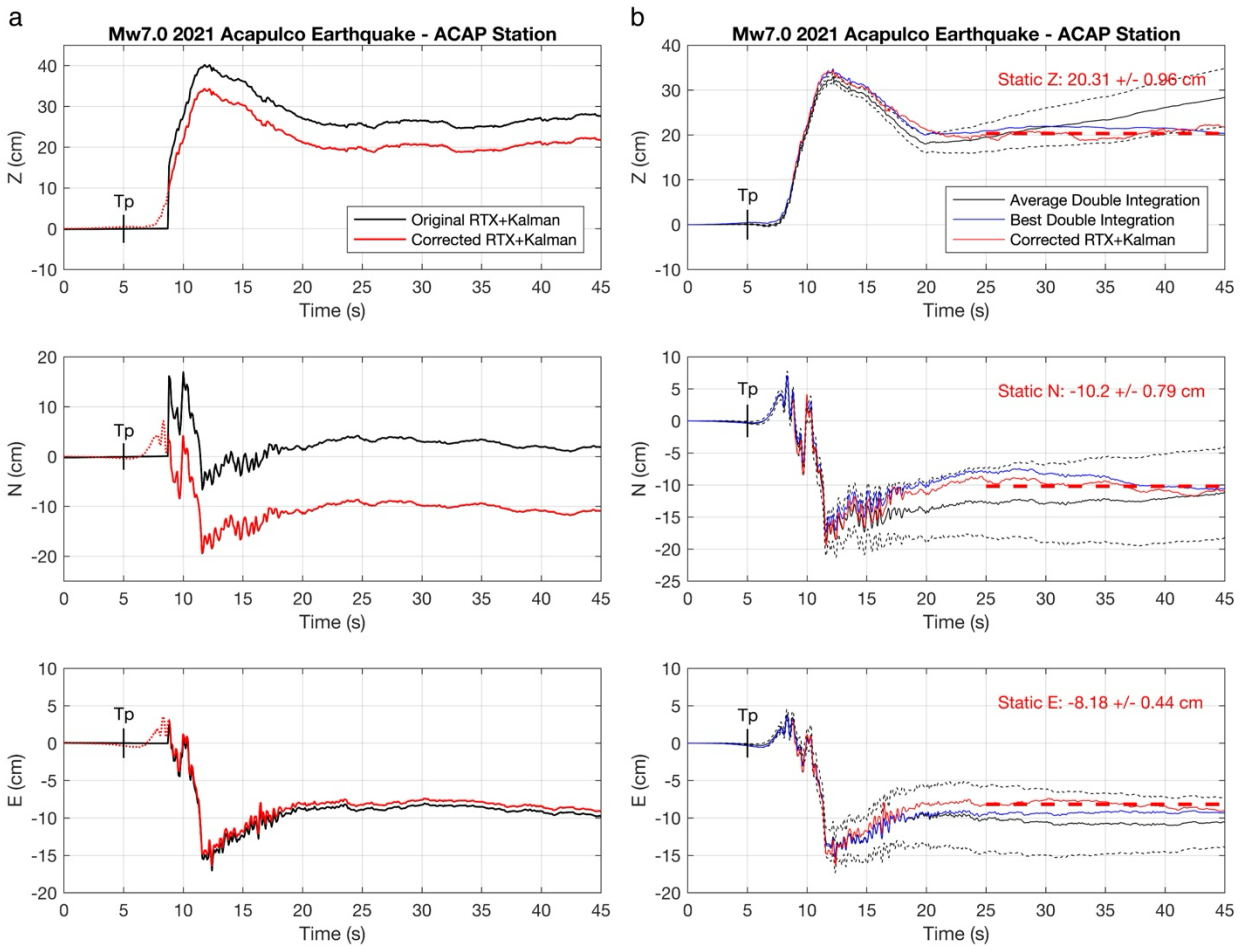

Fig. S2. Estimation of co-seismic displacements at station ACAP from GNSS-RTX-Kalman and acceleration data for the 2021 Acapulco earthquake. (a) Three displacement components estimated by a Kestrel instrument using GNSS-RTX-Kalman corrections (black). Note that the station started recording 4 seconds after the arrival of the P-wave. The red curves are the corrected records (see panel b). (b) To correct the RTX-Kalman records (panel a, black), a double integration with baseline correction according to Melgar et al. (2013) was performed for the first 4 seconds of the signals and the result was concatenated with the RTX-Kalman estimates (red). The black curves show the variation of the double integration as a function of the baseline parameterization and the blue curve the preferred estimate. Note that the integration is very stable during the first 4 seconds.

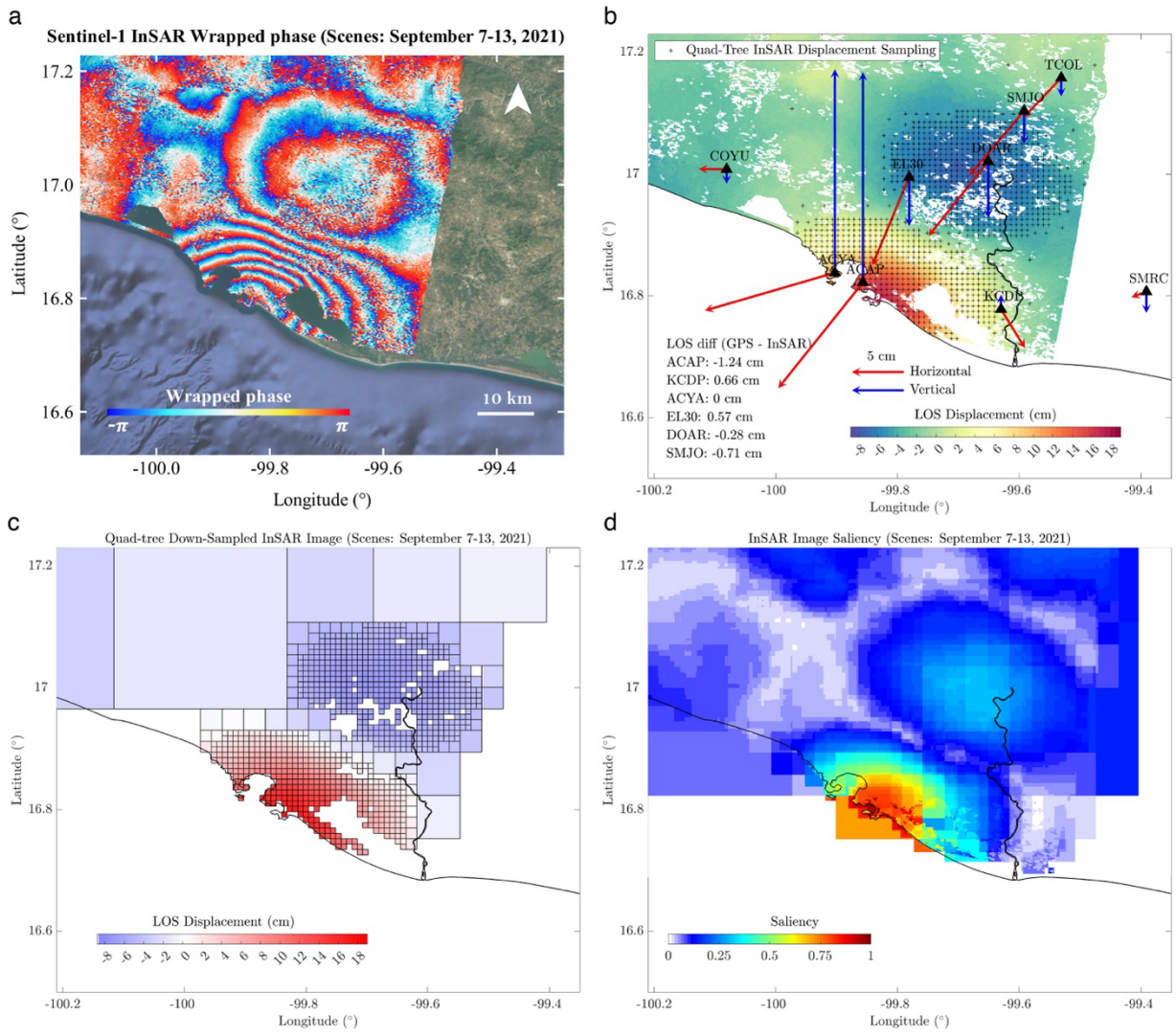

Fig. S3. InSAR data processing for the 2021 Acapulco earthquake. (a) Wrapped phase for the ascending track for scenes acquired on 7 and 13 September. (b) Unwrapped line-of-sight (LOS) displacements together with the co-seismic displacement at the GNSS sites. The interferogram was calibrated to match the co-seismic displacement at station ACYA. Differences at several sites with GNSS displacements in the LOS direction are shown. (c) Quad-tree InSAR data sampling according to Gao et al. (2021) based on the saliency of the image shown in panel (d).

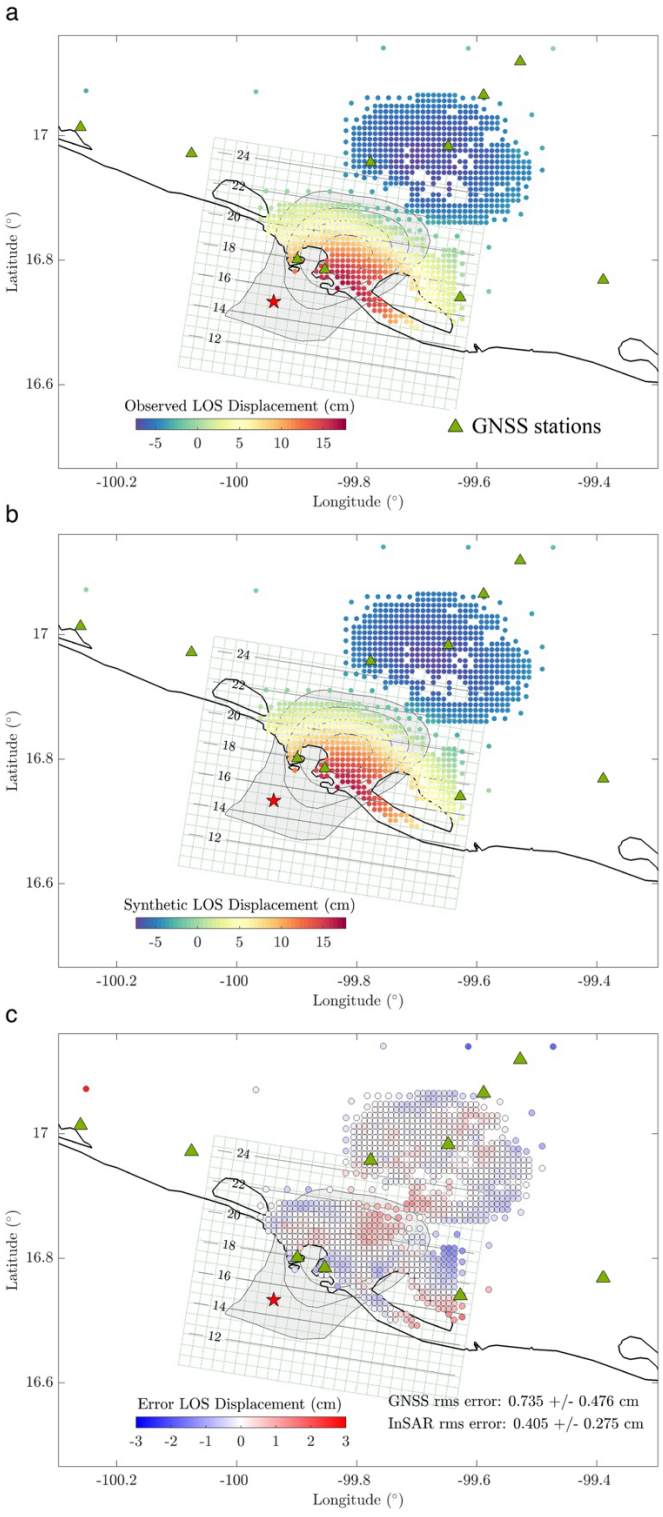

Fig. S4. Space distribution of InSAR data co-seismic inversion error. See headings of colorbars.

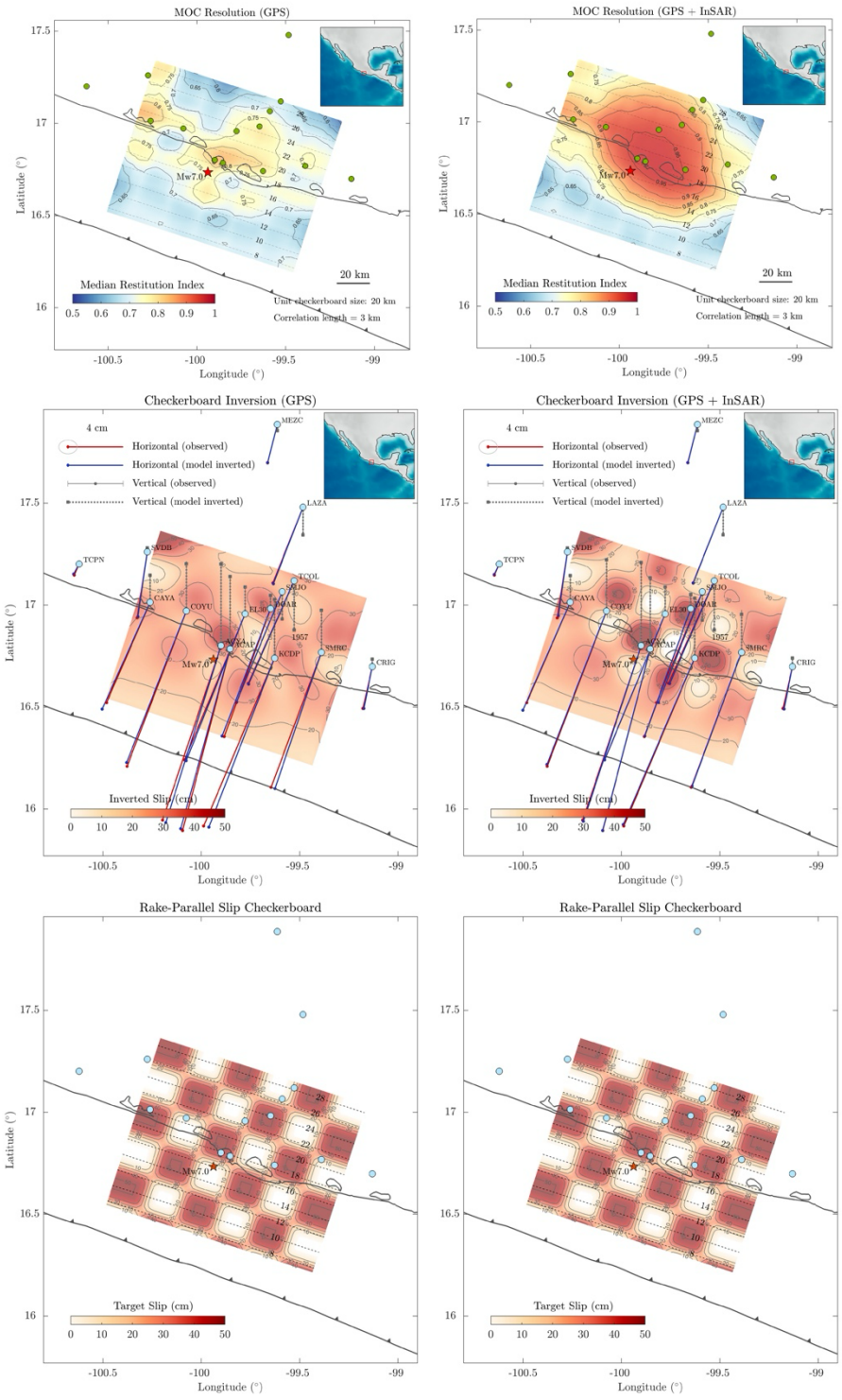

Fig. S5. Co-seismic inversion resolution tests for GNSS data alone (left column) and for the joint inversion of GNSS and InSAR data (right column). The tests correspond to mobile checkerboard (MOC) inversions for an asperity size of 10 km in length (bottom row), where the median restitution index (MRI) is shown in the first row for both exercises. The MRIs within the actual rupture area are above 0.95 in the joint inversion, which means that the nominal error there for real data is below 5%. The middle row shows the synthetic inversions for a given checkerboard.

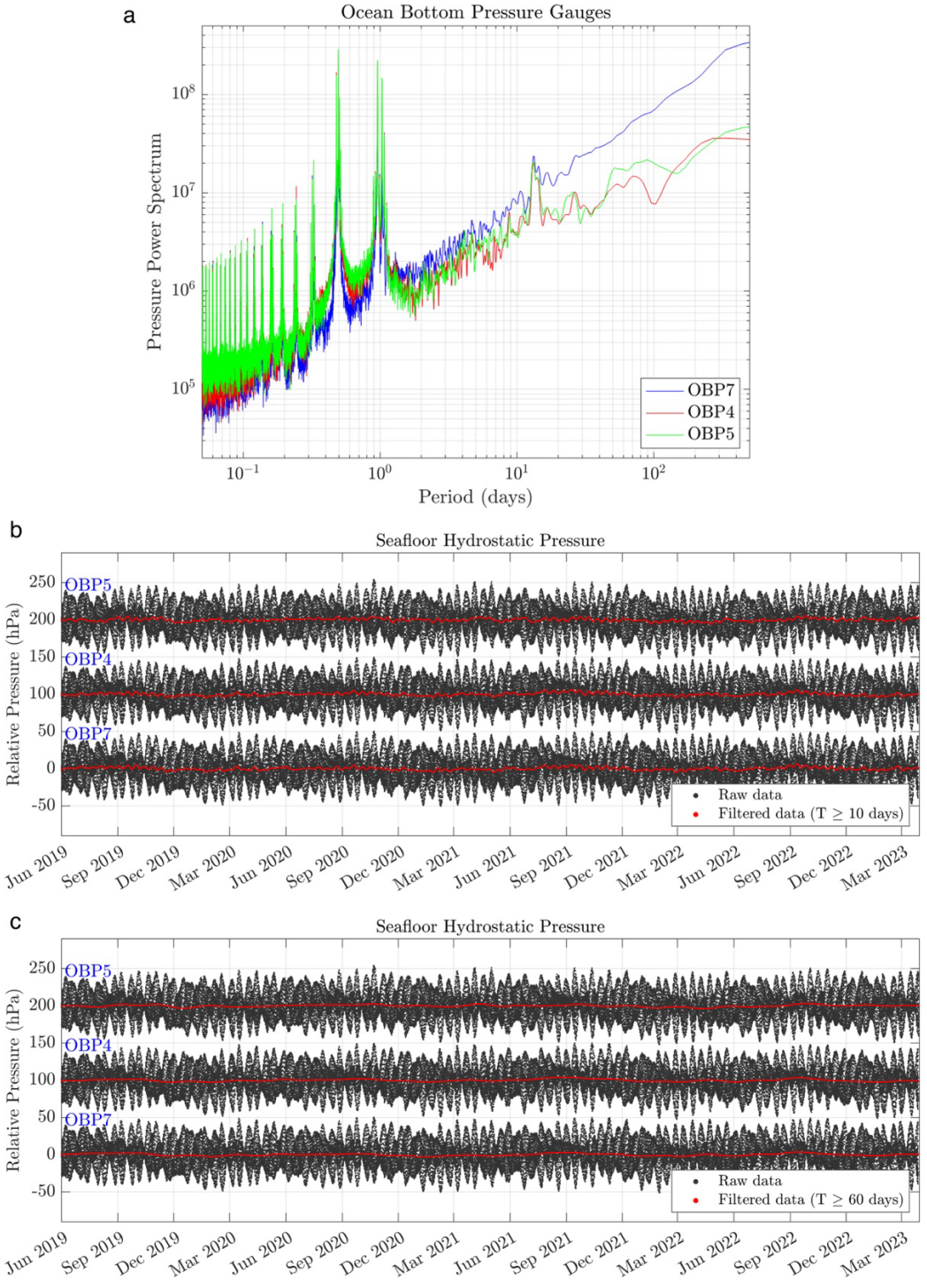

Fig. S6. Spectral analysis of ocean bottom pressure records at the three long-standing sites. (a) Fourier spectra as a function of period. (b) and (c) show the comparison of raw (black) and filtered data for cut-off periods of 10 and 60 days (red), respectively. Filter used is a four-order Butherworth.

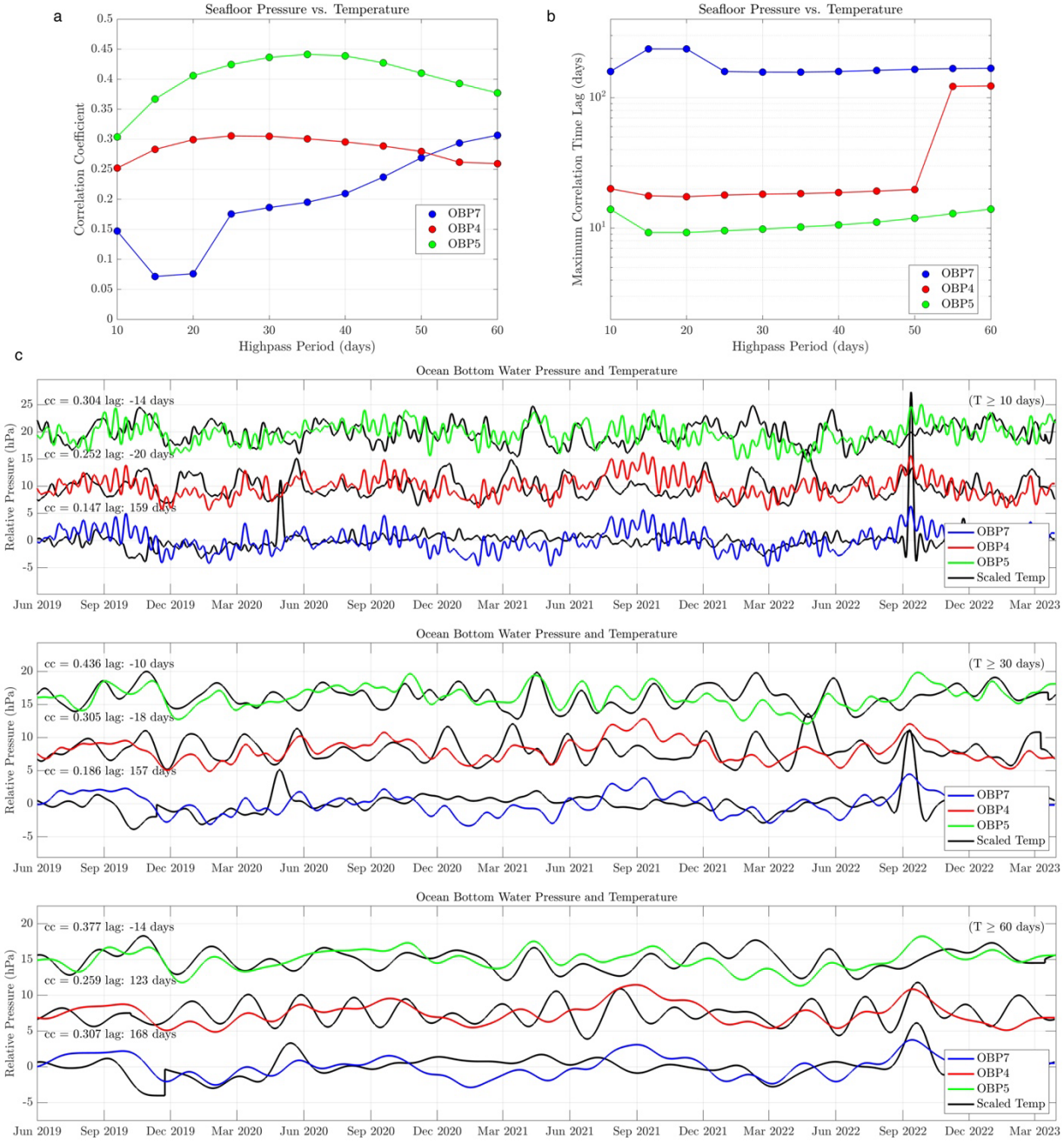

Fig. S7. Comparison of ocean bottom pressure with collocated temperature at the three long-standing sites. (1) Maximum correlation coefficients (cc) as a function of high-pass cut-off periods. (b) Shifts that maximize cc. (c) Comparisons of pressure and temperature time series for different cut-off periods (see text in panels), where the temperature has been normalized so that its RMS is equal to that of the pressure. Temperature time series have been shifted to maximize cc.

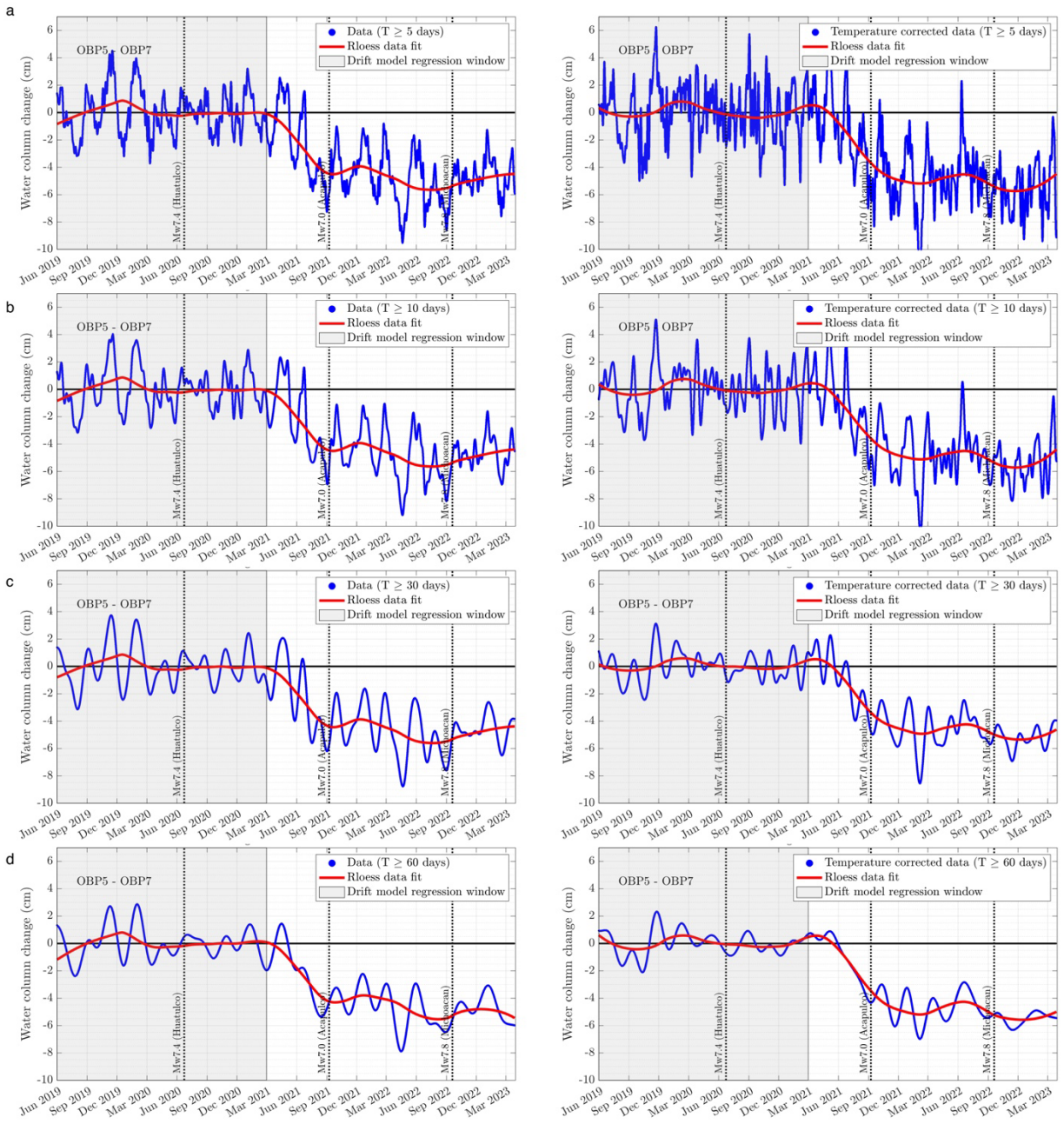

Fig. S8. Temperature correction of ocean bottom pressure records at site OBP5 relative to the Cocos Plate (OBP7). The left column shows the pressure without correction, while the right column shows the corrected signal for different high-pass cut-off periods (different rows, see legends). The correction was done by subtracting the scaled temperature with the moveout that maximizes the cross-correlation coefficient between the two signals in the same bandwidth. Note how the correction eliminates a significant amount of long-period noise, so that the onset of the offshore SSE prior to the Acapulco earthquake is much better defined, among other valuable features for the inversion. Note also how robust/stable the correction is regardless of the bandwidth (compare data fits, red curves).

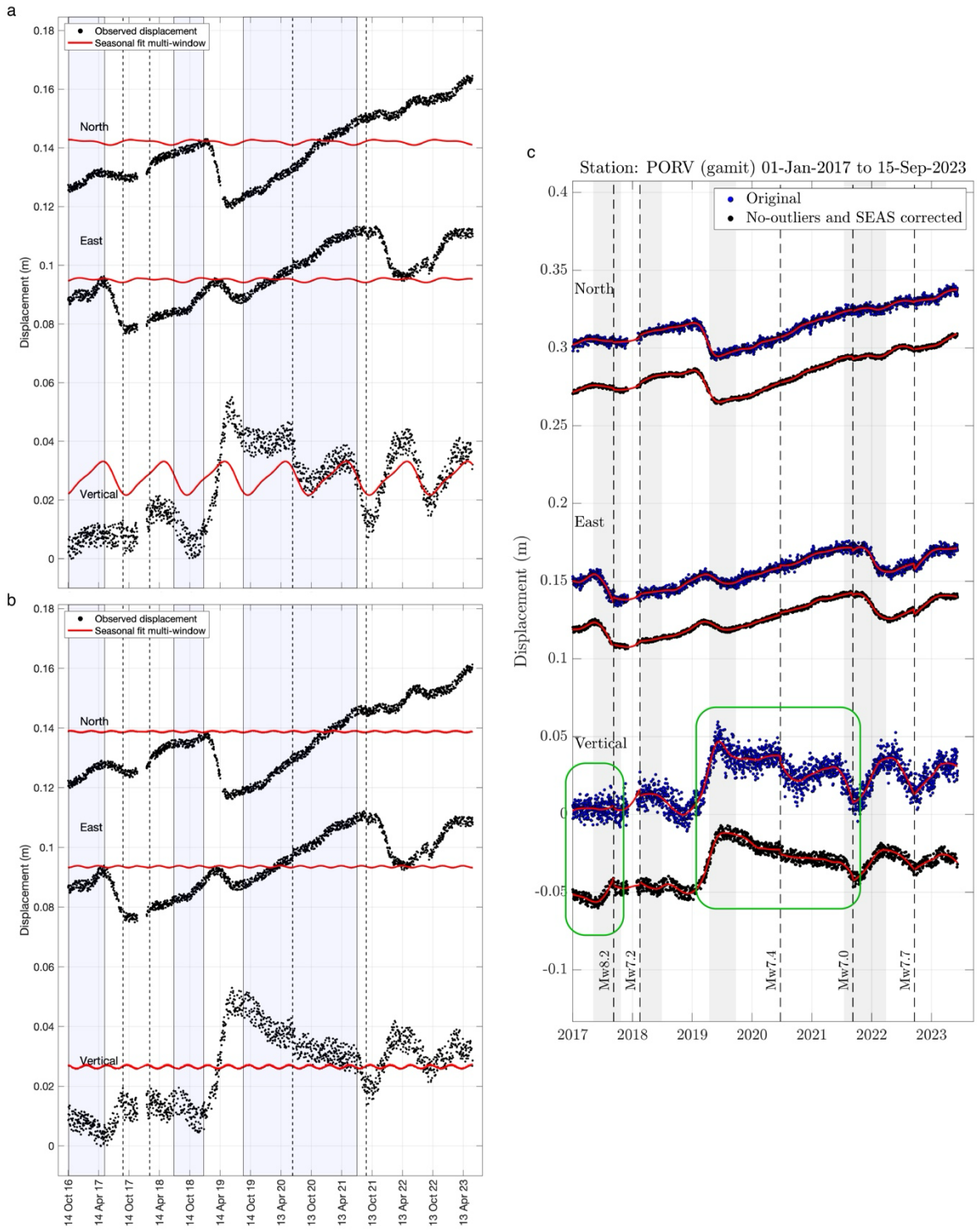

Fig. S9. Seasonal noise reduction and outlier removal from GNSS time series. (a) and (b) show the two stages of the correction where annual, semi-annual and higher frequency harmonic functions are fitted along inter-SSE windows and removed according to Villafuerte et al. (2024) (c) Comparison of raw (blue) and corrected (black) signals at three different sites. Green rectangles indicate segments where the correction is clearly visible, particularly in the vertical component.

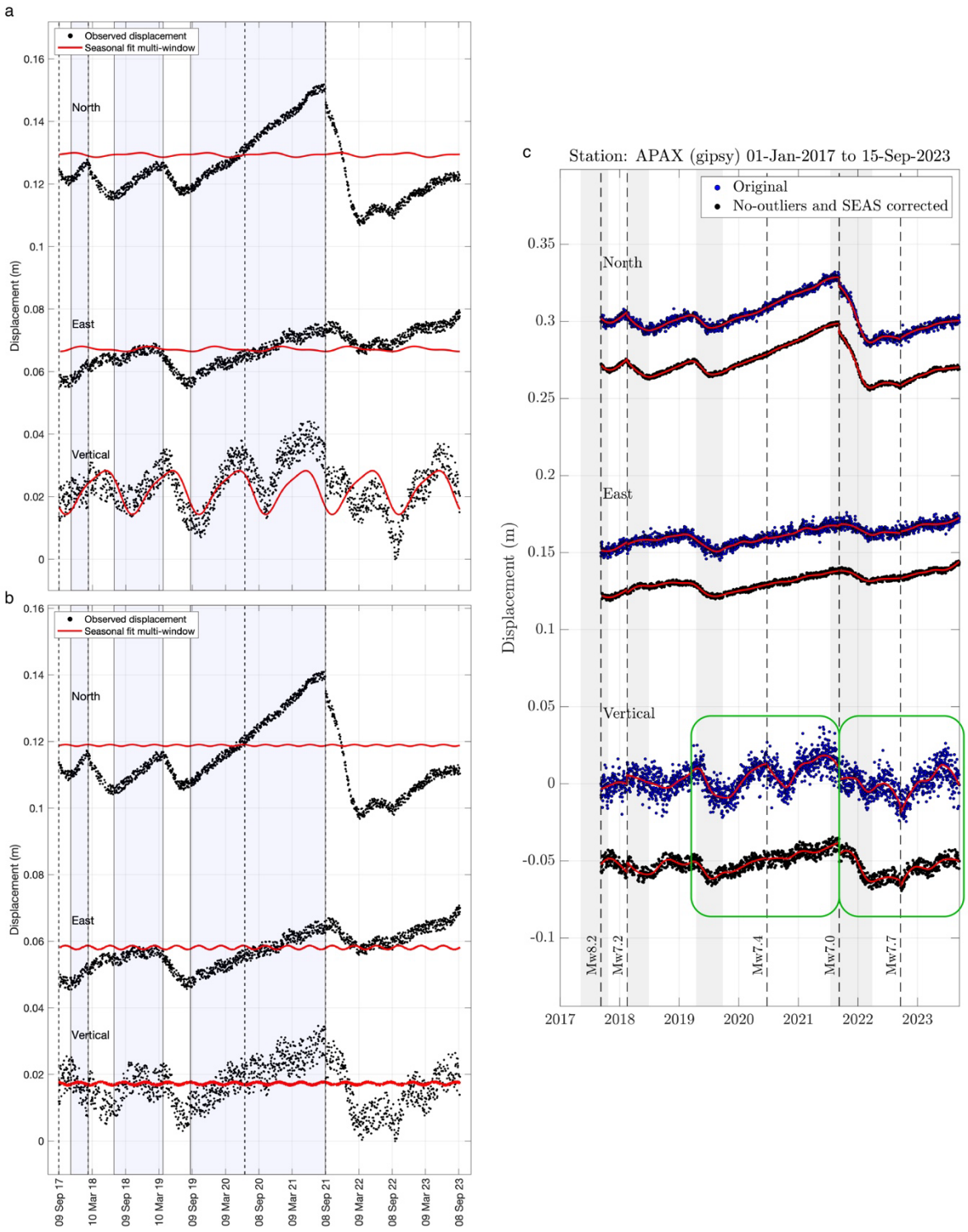

Fig. S9. (continue)

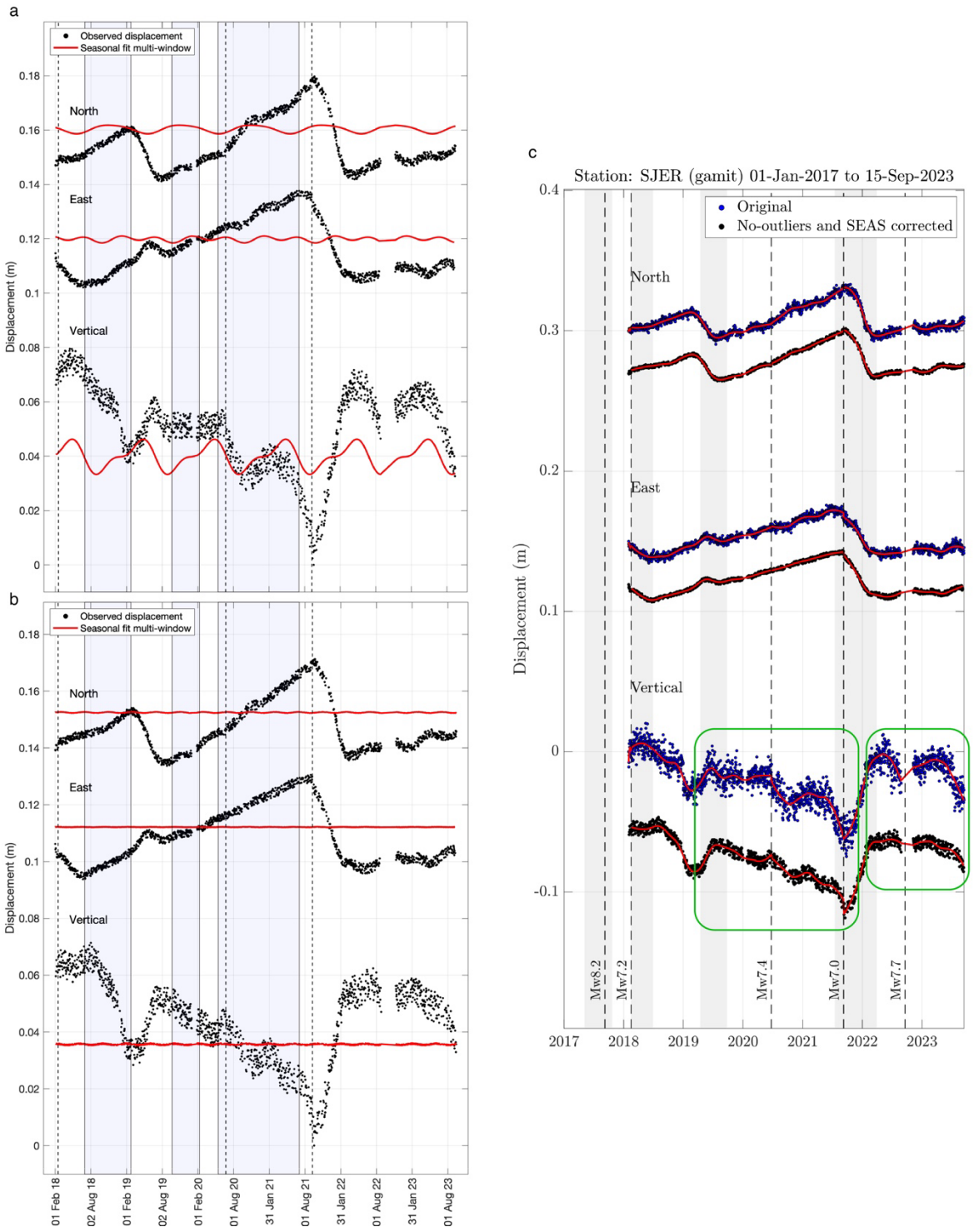

Fig. S9. (continue)

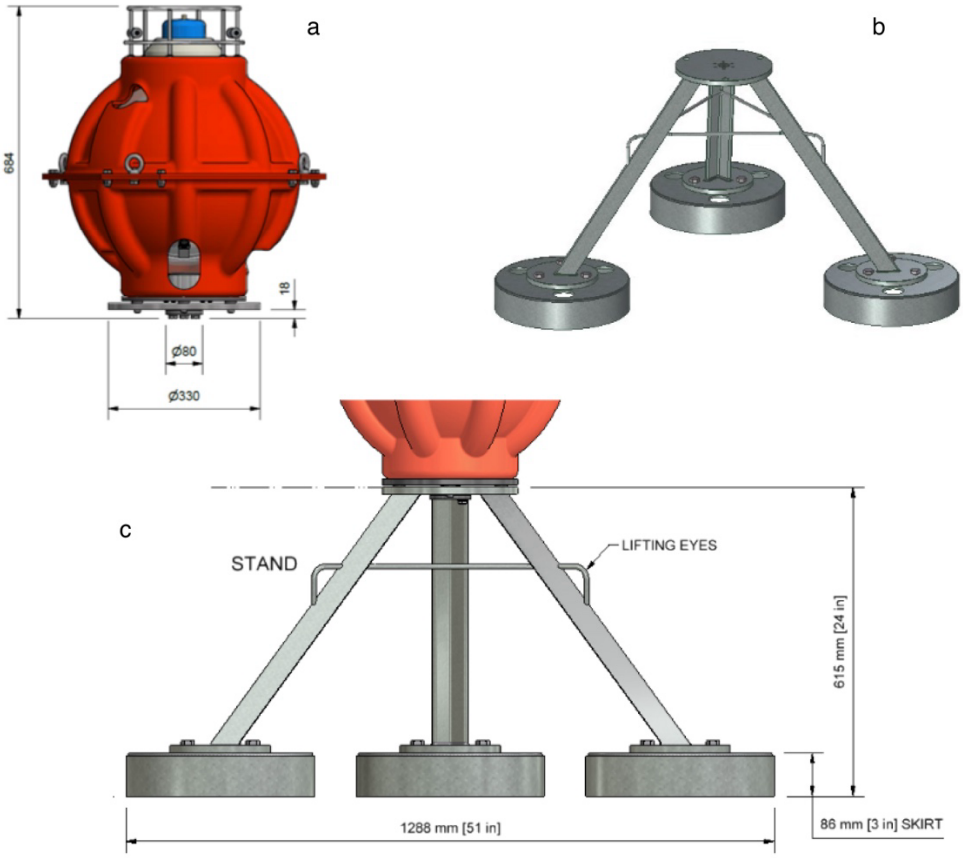

Fig. S10. Sonardyne Co Fetch unit dimensions and configuration. (a) Plastic covering (orange) of the glass sphere and transducer (blue). (b) and (c) show the steel tripod on which the glass sphere is mounted.

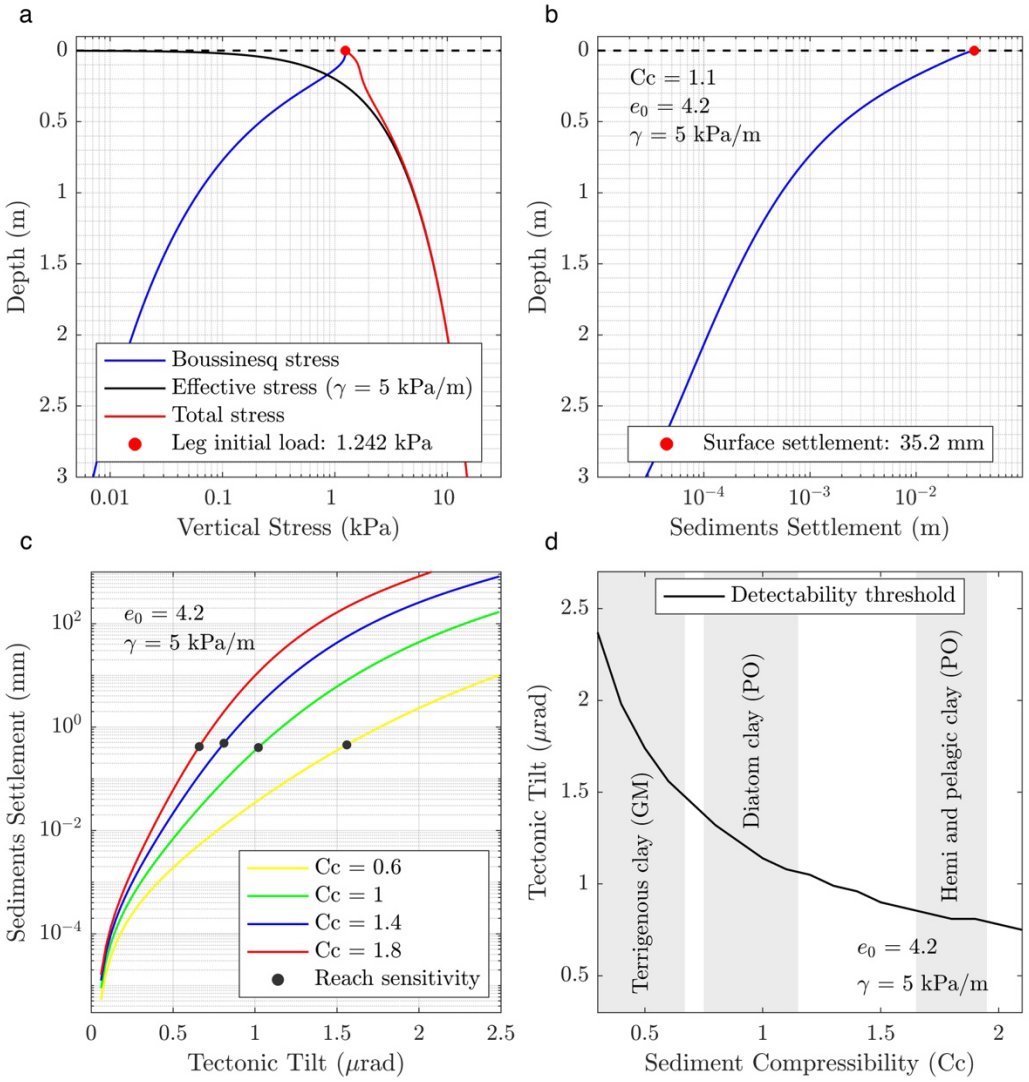

Fig. S11. Analysis of seafloor sediment settlement beneath a fetch unit as a function of basement (tectonic) tilt. (a) Boussinesq (blue) and effective (black) stress distributions in the sediment column beneath a tripod foot for the initial load of the Fetch unit. The total stress is shown in red. (b) Sediment settlement as a function of depth for the initial load considering an average compressibility index (Cc) and void ratio for different seafloor sediment types. (c) Surface settlement for different Cc's as a function of basement tilt. Dots indicate the moments when the effective instrument tilt reaches the tiltmeter sensitivity threshold of 436 µrad within the glass sphere. (d) Curve showing the basement tilts at which the tiltmeter sensitivity is reached as a function of Cc. Typical ranges of Cc for different types of seabed sediments are shown in grey.

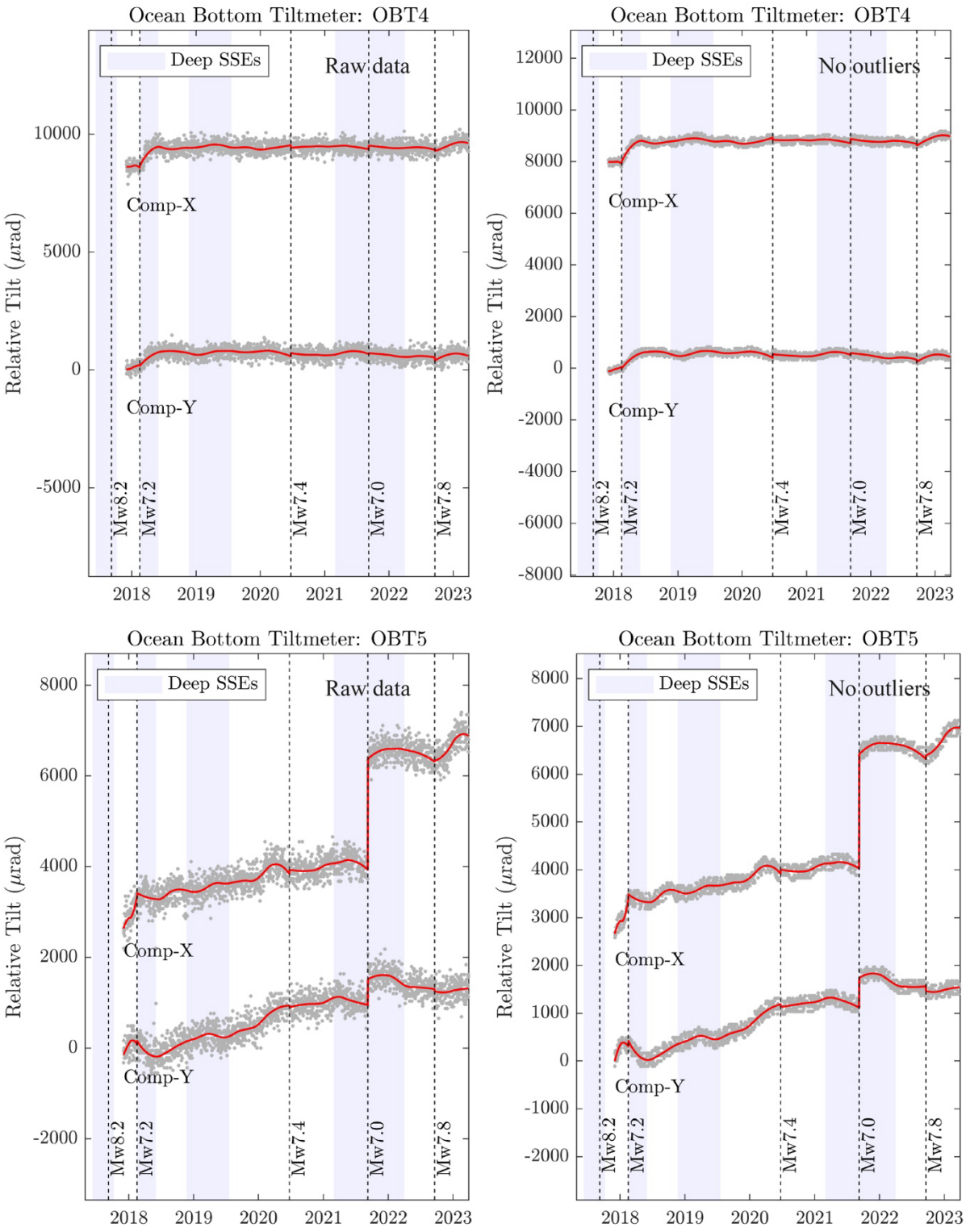

Fig. S12. Two-component raw tilt data (left column) with 24 h sampling rate and tilt data after outlier removal (right column) at our four ocean bottom tiltmeters. Red curbs are locally weighted regression functions (fLOESS) using a 2nd order polynomial with a window support of 250 samples. Regressions are performed independently for each earthquake bounded period, so that possible co-seismic discontinuities are visible. Outliers are data more than 1.5σ away from the regressions per window. Note that fitting functions are not affected by the outlier removal.

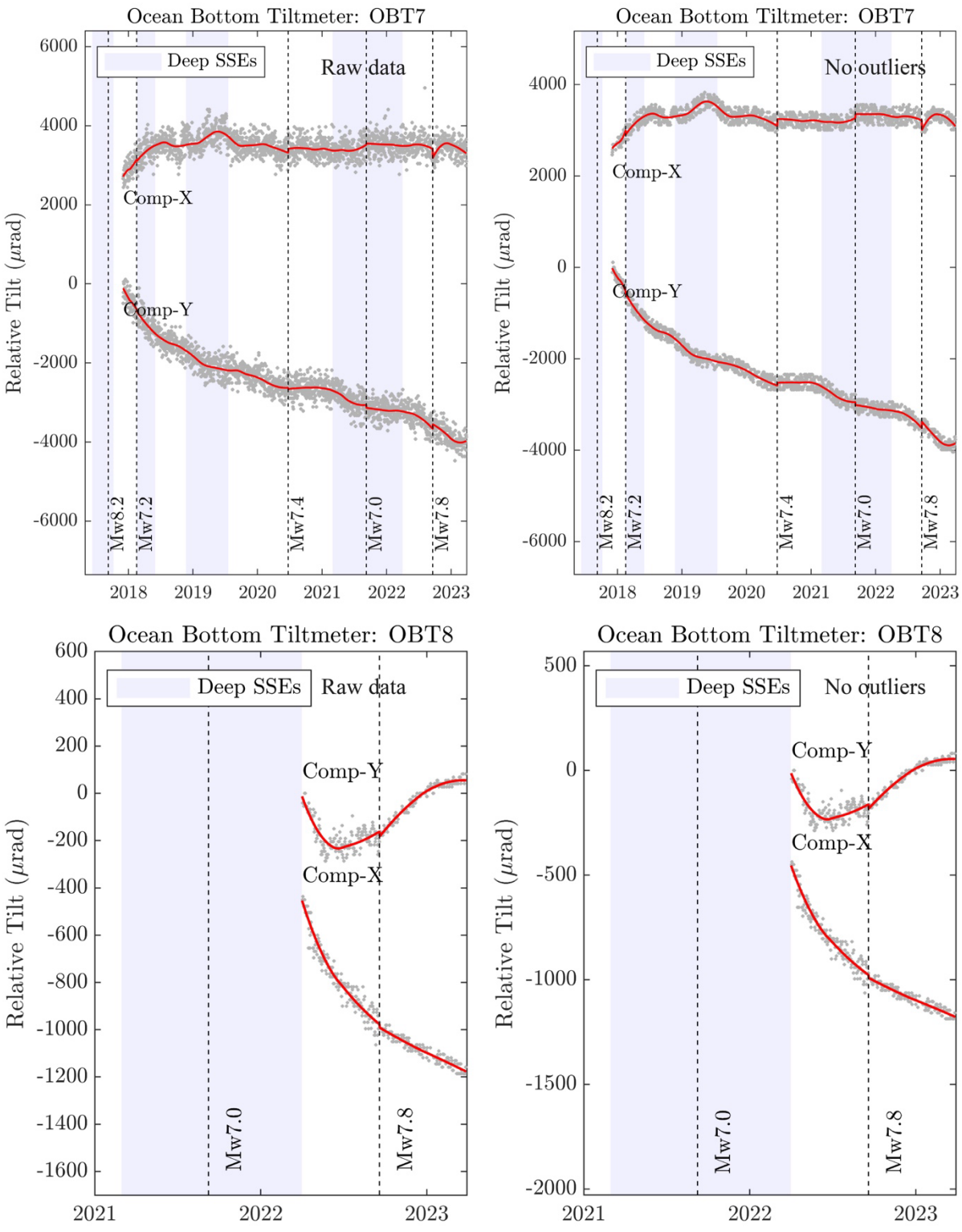

Fig. S12. (continue)

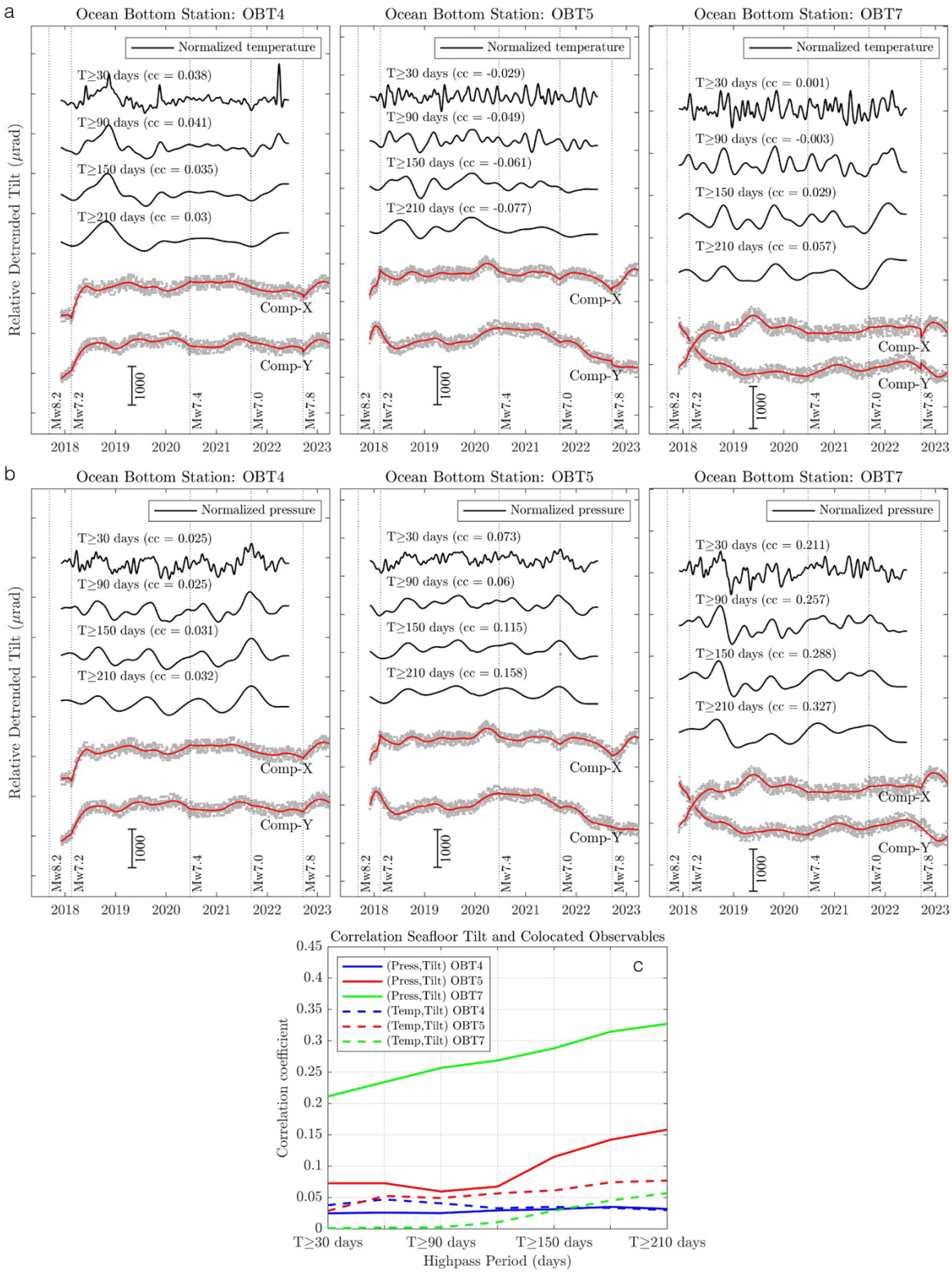

Fig. S13. Comparison of ocean bottom tilt data with collocated pressure and temperature at the three long-standing OBOs (see panel headings). For comparison, all tilt time series were linearly detrended. Normalized temperature (a) and pressure (b) so that their RMS is equal to that of the associated tilt data for different high-pass periods (see labels). (c) Maximum cross-correlation coefficients between tilt and both temperature and pressure for different bandwidths.

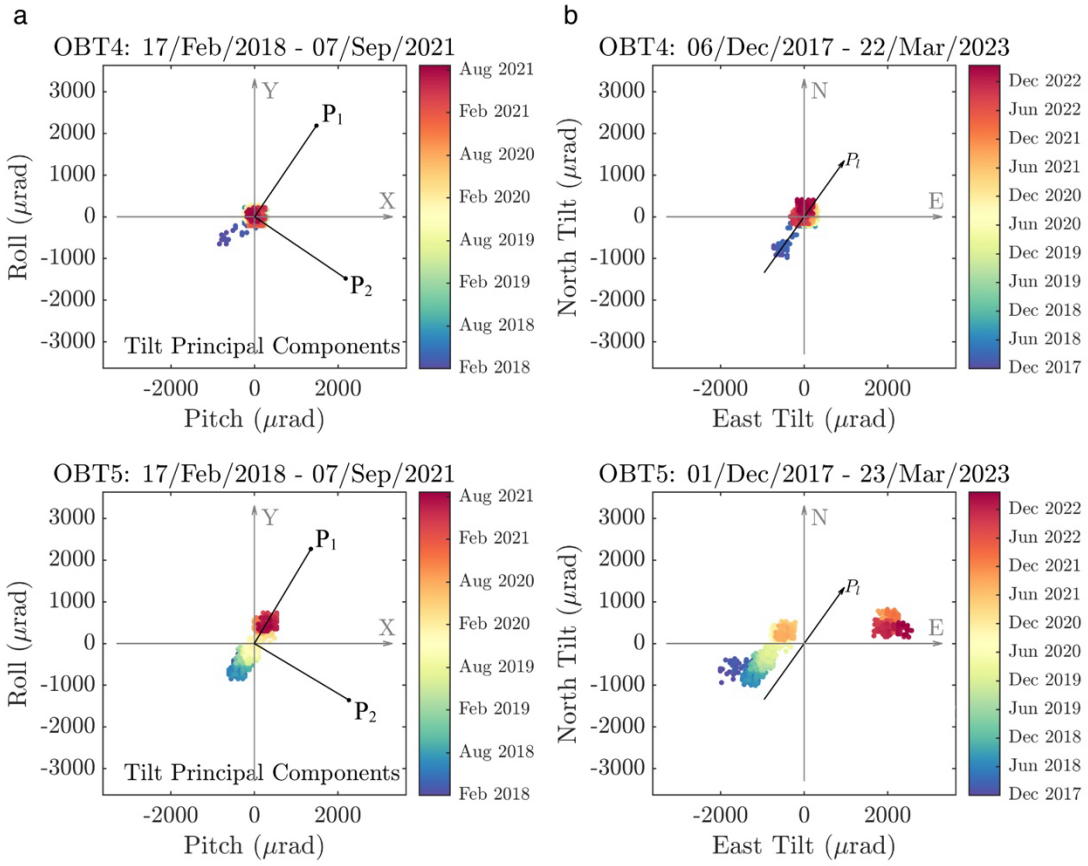

Fig. S14. Tiltmeter sensor orientation at the four OBOs. (a) Baselines (see panel headings for bounding dates) as a function of time (color coded) together with the two eigenvectors, P1 and P2, of the baseline covariance matrix. (b) Geographically oriented tilt data as a function of time, assuming that the first eigenvector coincides with the plate convergence direction (P_l).

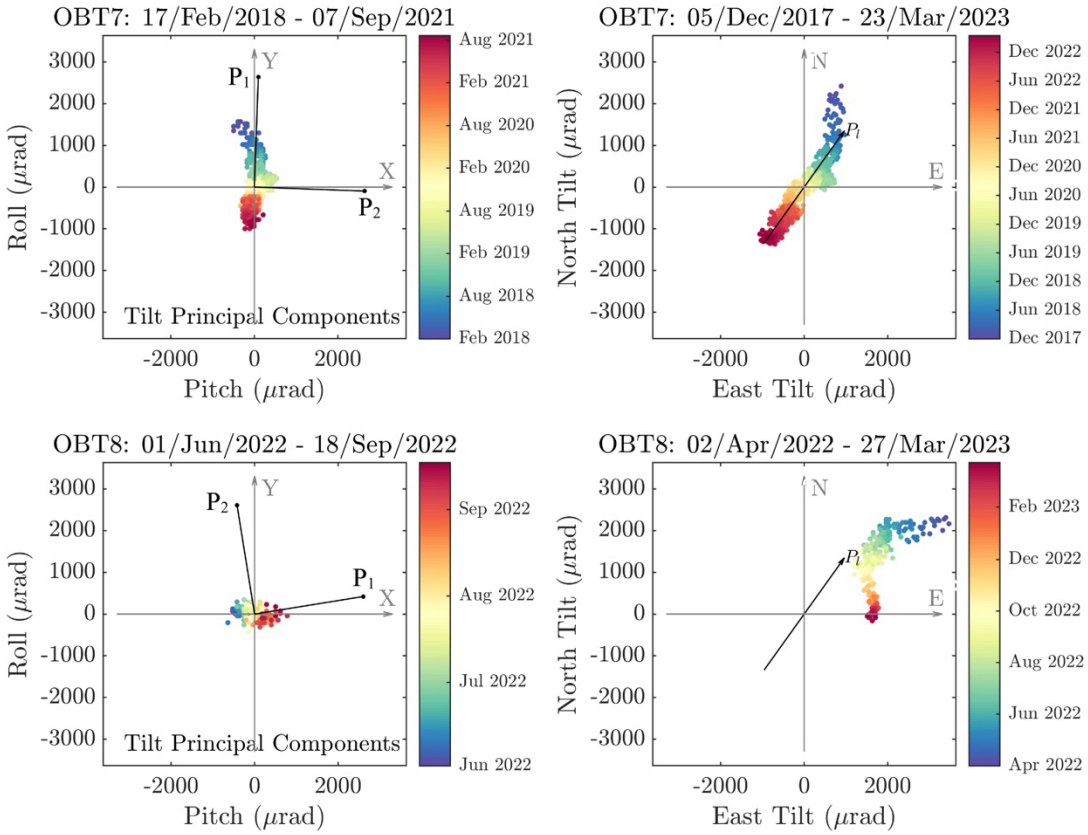

Fig. S14. (continue)

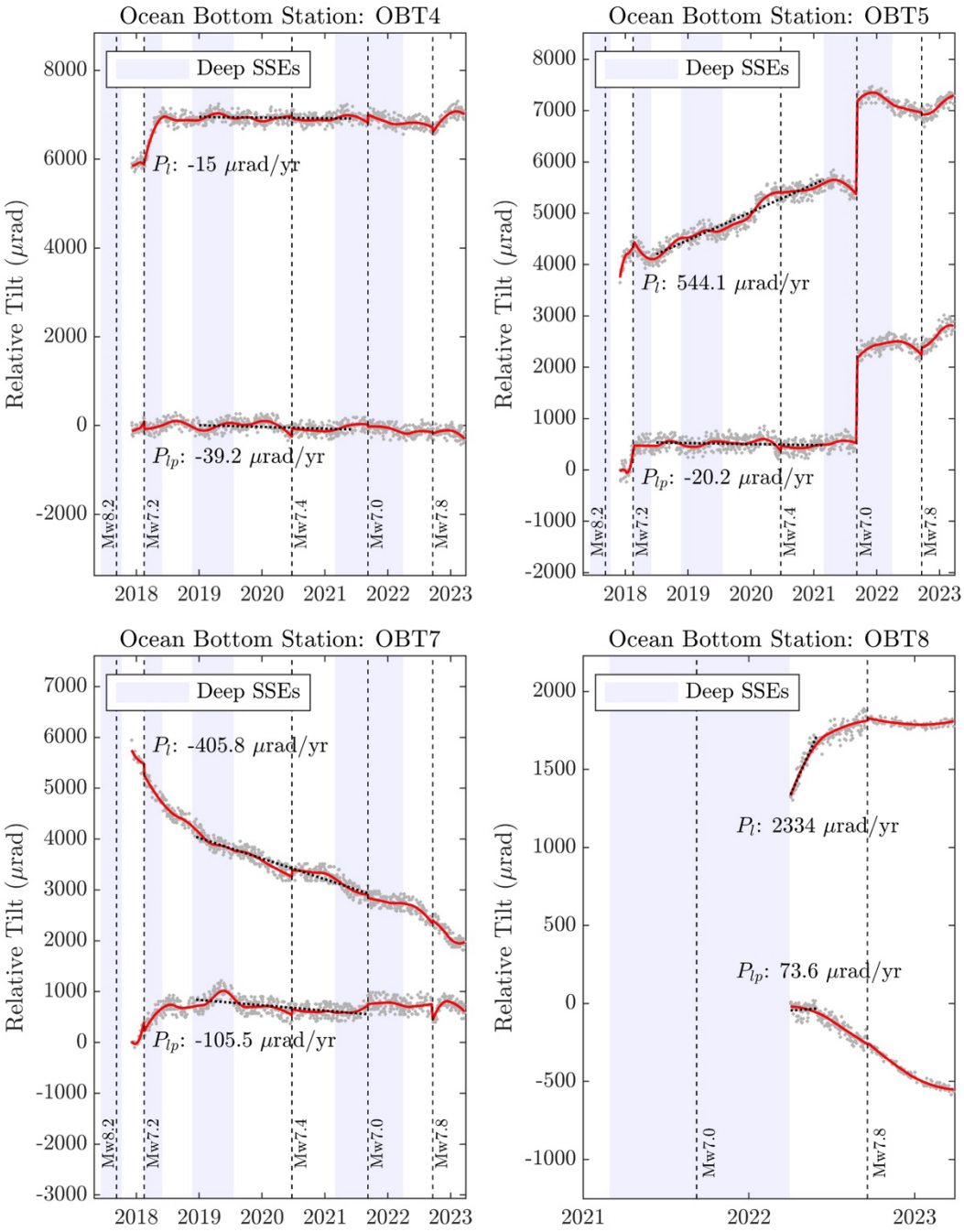

Fig. S15. Two components of geographically oriented tilt data at the four OBOs before the amplification correction (see panel headings).

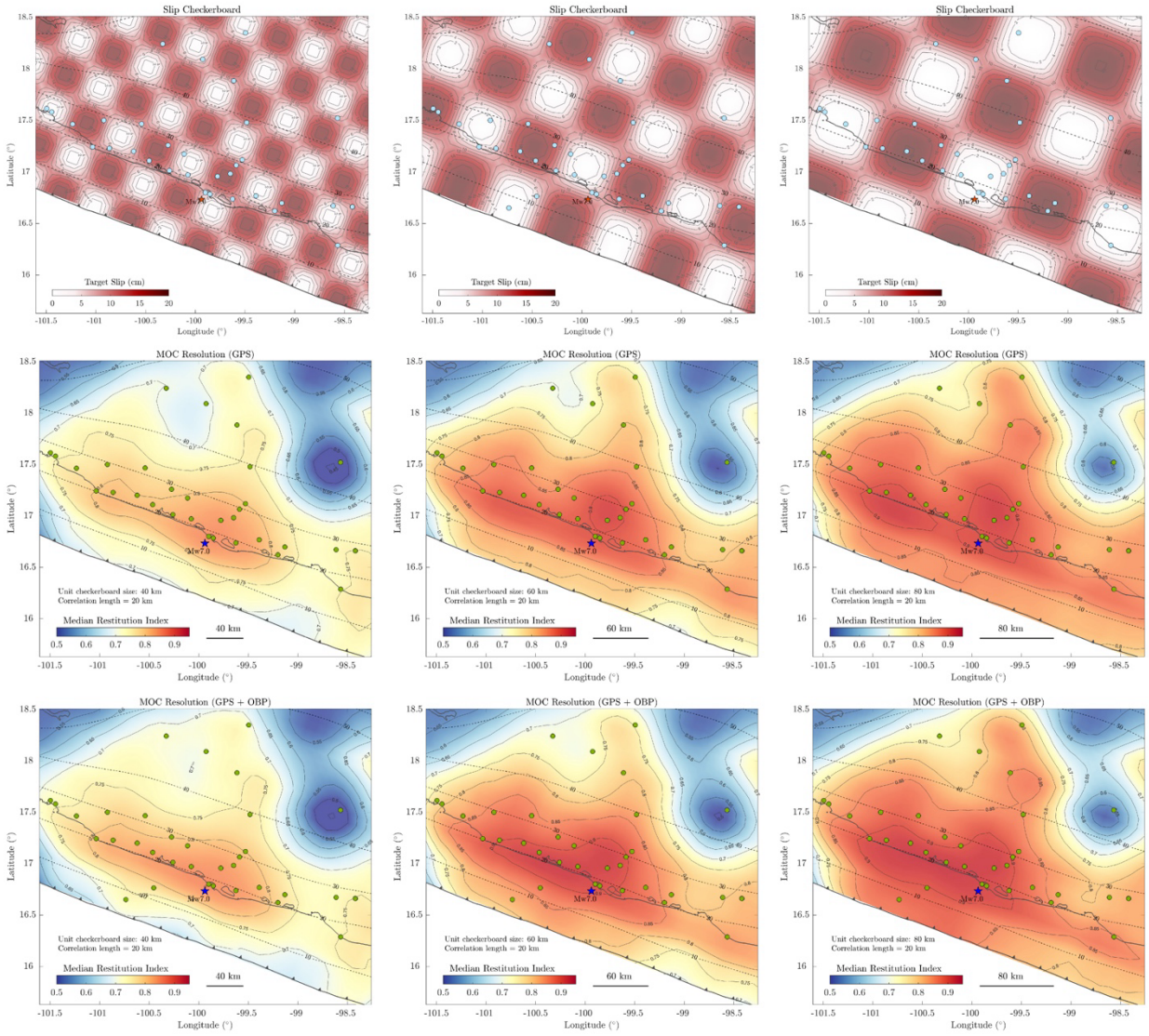

Fig. S16. Mobile checkerboard (MOC) resolution tests for slip asperities of 40 (left column), 60 (middle column) and 80 km (right column) length for inversion of GNSS data alone (second row) and for joint inversion of GNSS and OBP data (bottom row). The checkerboards in the first row were randomly selected to illustrate the slip models behind each MOC test. The median restitution index (color gradients) is a metric that quantifies the ability of the inversions to reconstruct the target model. Note that MRI values near the trench are above 0.8 along the seismic gap for asperities greater than 40 km, implying that nominal errors in the real data inversion are less than 20%.

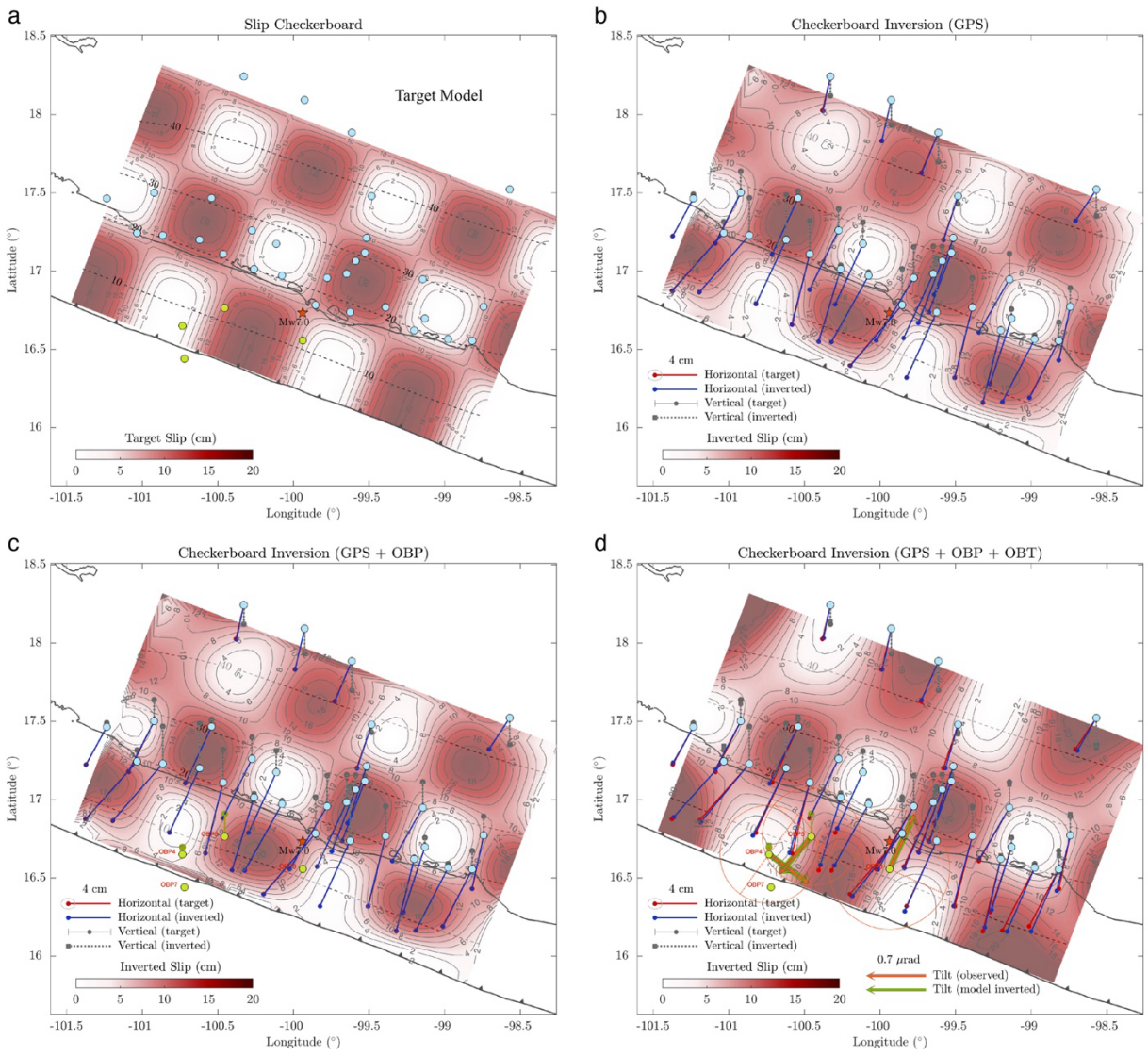

Fig. S17. Inversion of a slip checkerboard with 60 km unit size reaching the oceanic trench (panel a, target model) for GNSS data alone (b), for the joint inversion of GNSS and OBP data (c) and for the joint inversion of GNSS, OBP and tilt data (d).

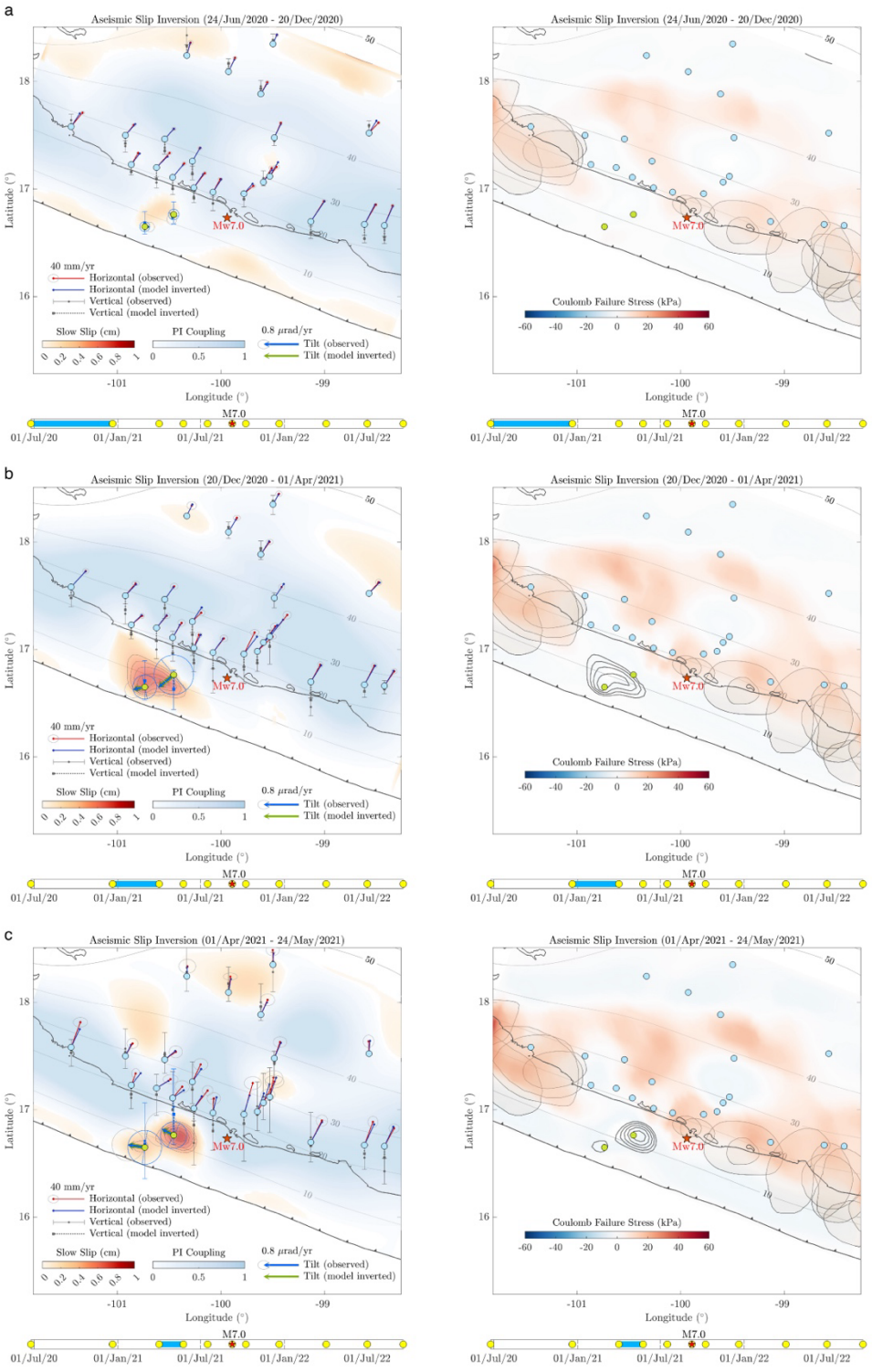

Fig. S18. Slip and plate interface coupling (PIC) joint inversion of GNSS, OBP and tilt data for ten consecutive windows, shown in the lower time lines (left column), together with the associated Coulomb failure stress (CFS, right column). The grey shapes in the right column indicate the rupture areas of historical earthquakes. The slip solution on the left is indicated by contours on the right.

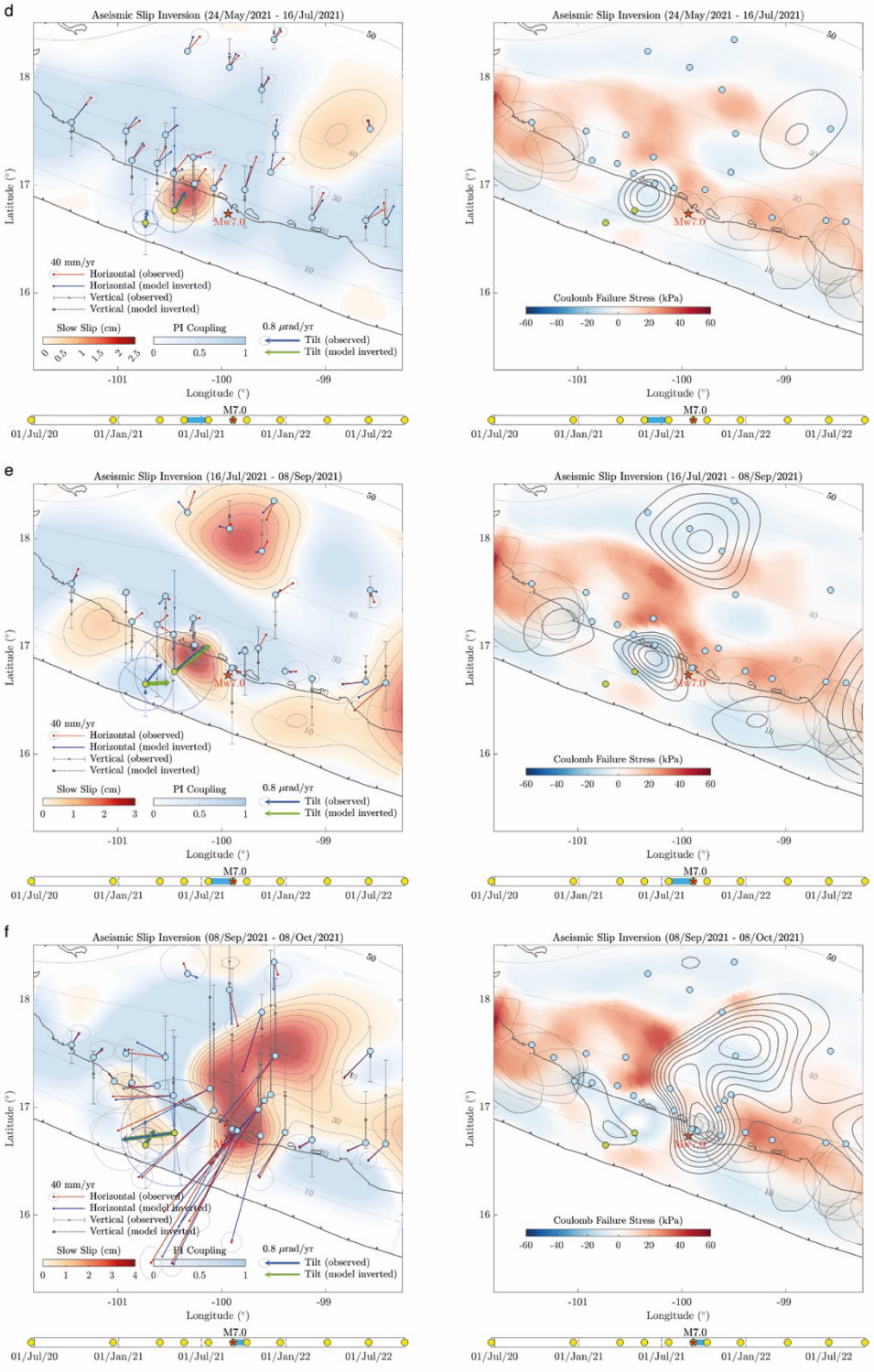

Fig. S18. (continue)

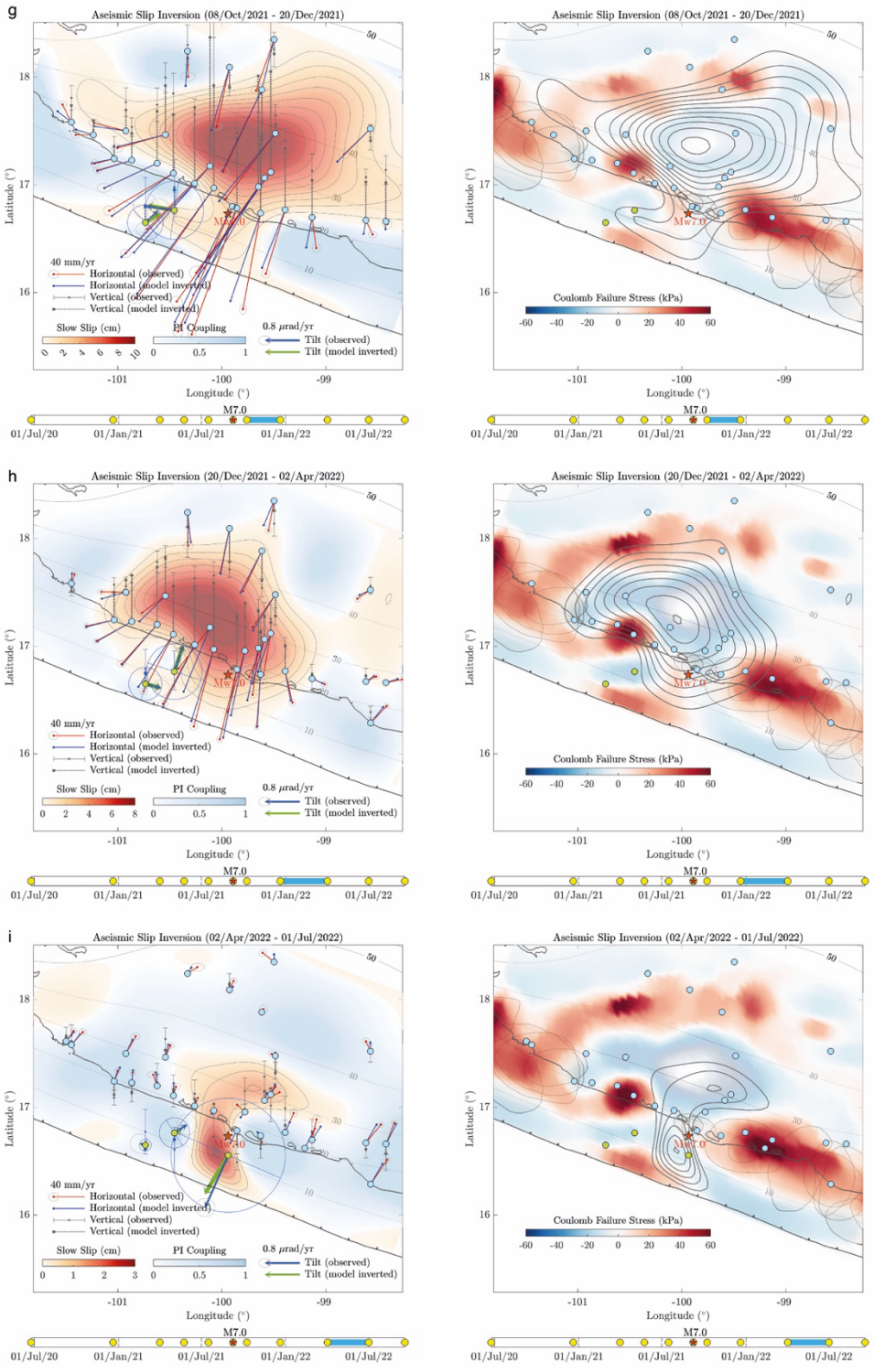

Fig. S18. (continue)

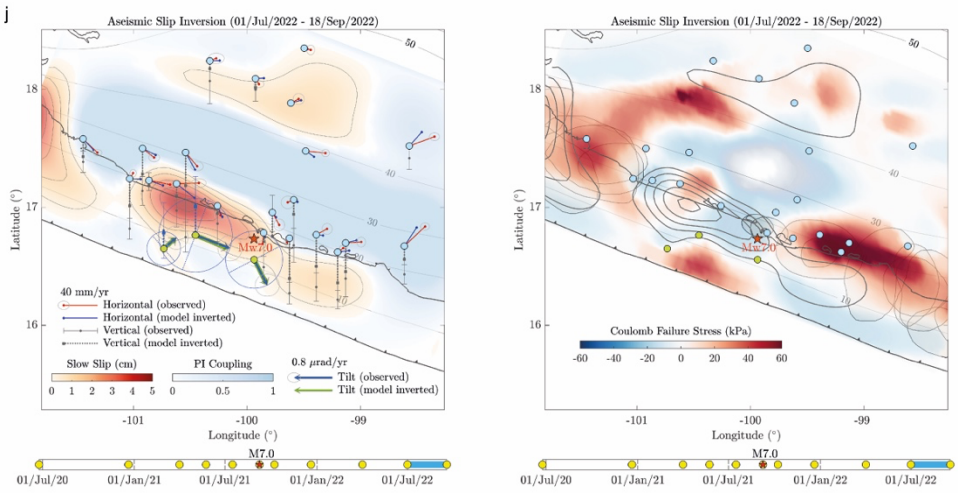

Fig. S18. (continue)

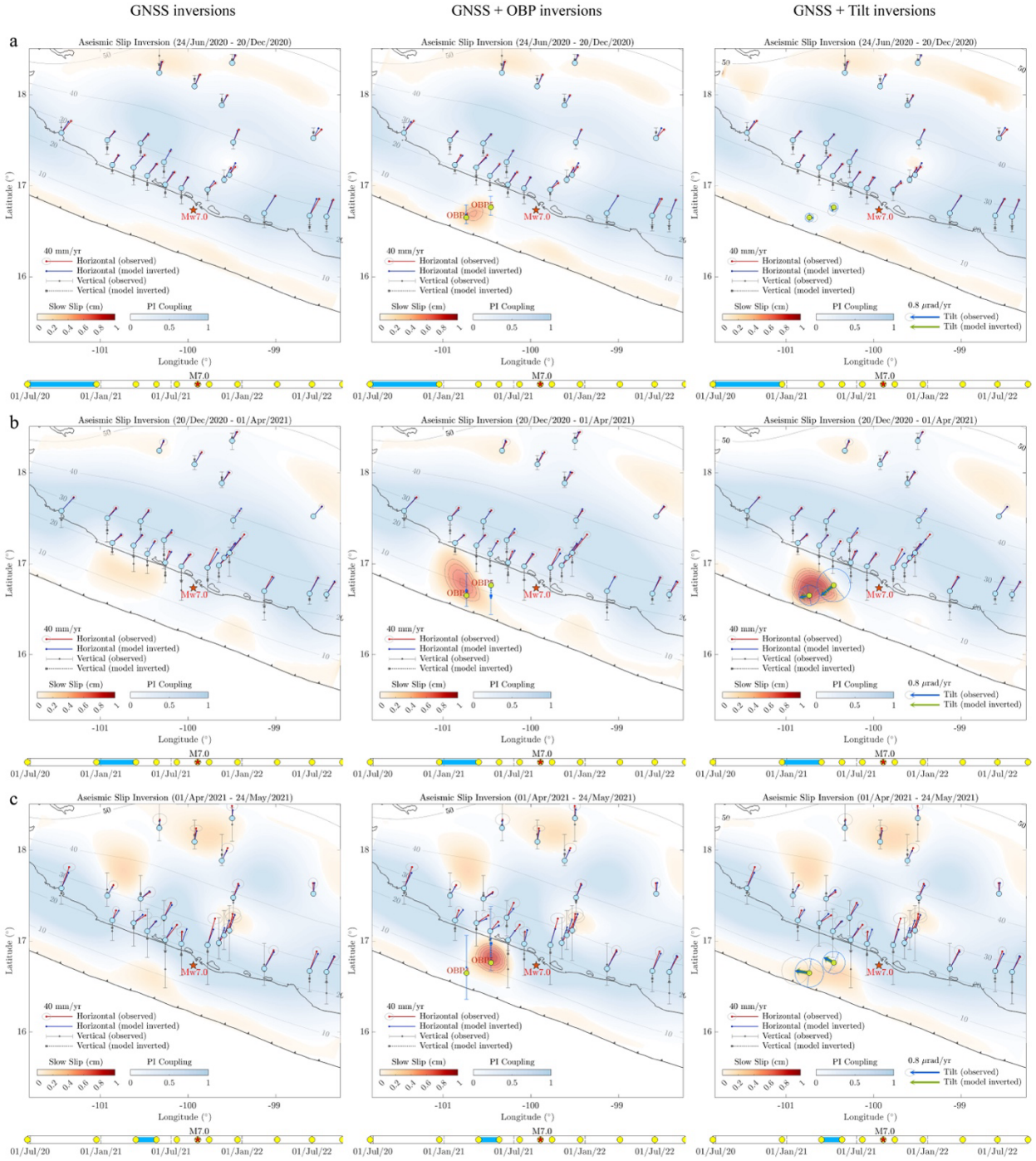

Fig. S19. Slip and Plate Interface Coupling (PIC) inversion comparison of ten consecutive windows with different data set combinations. The left column shows the inversion of GNSS data alone, the middle column shows the inversion of GNSS and OBP data, and the right column shows the inversion of GNSS and tilt data. Note that only the independent seafloor inversions find the downdip propagation of the offshore SSE prior to the 2021 Acapulco earthquake. GNSS data can resolve the offshore SSE only in its final stage before rupture (panel e).

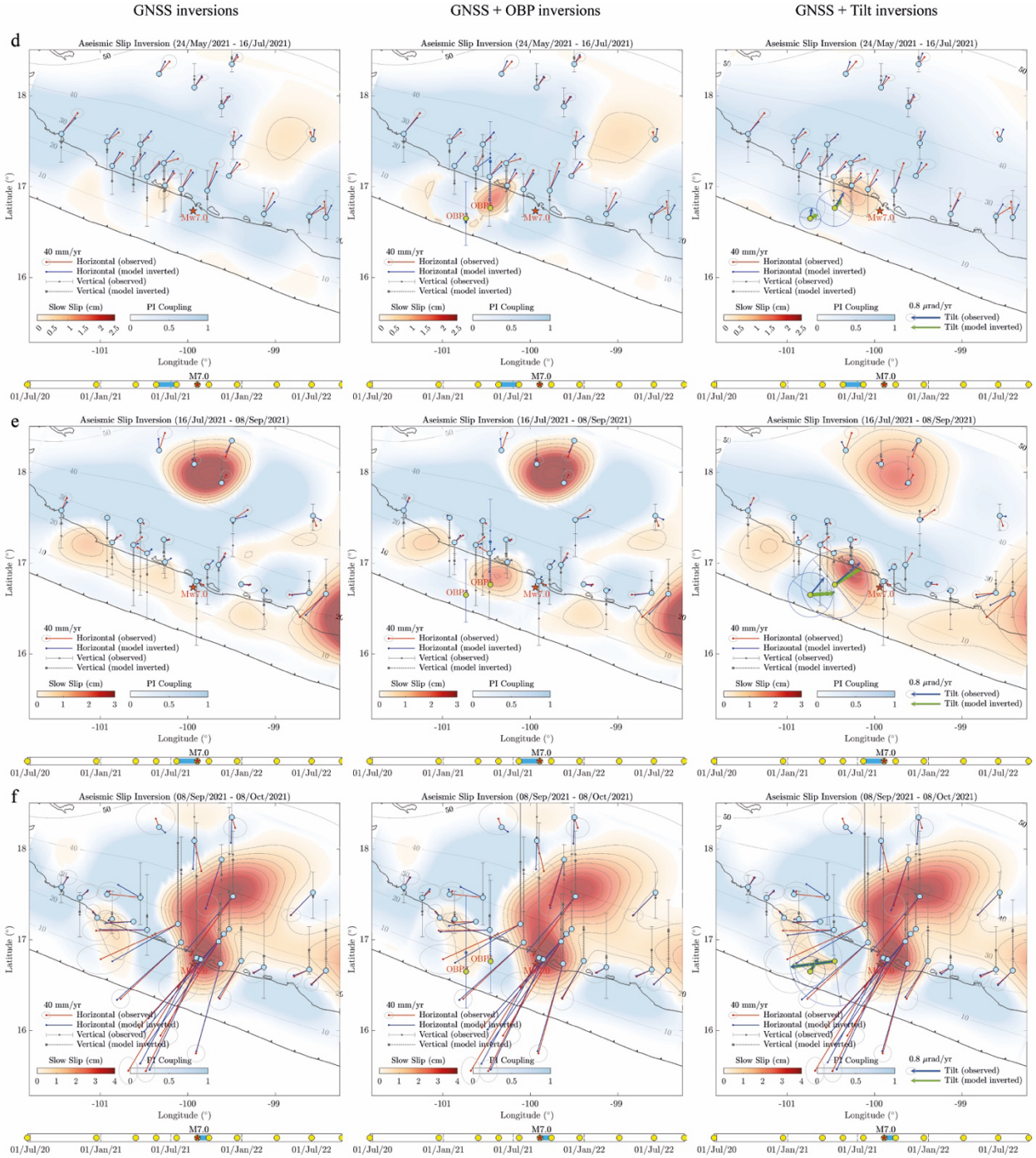

Fig. S19. (continue)

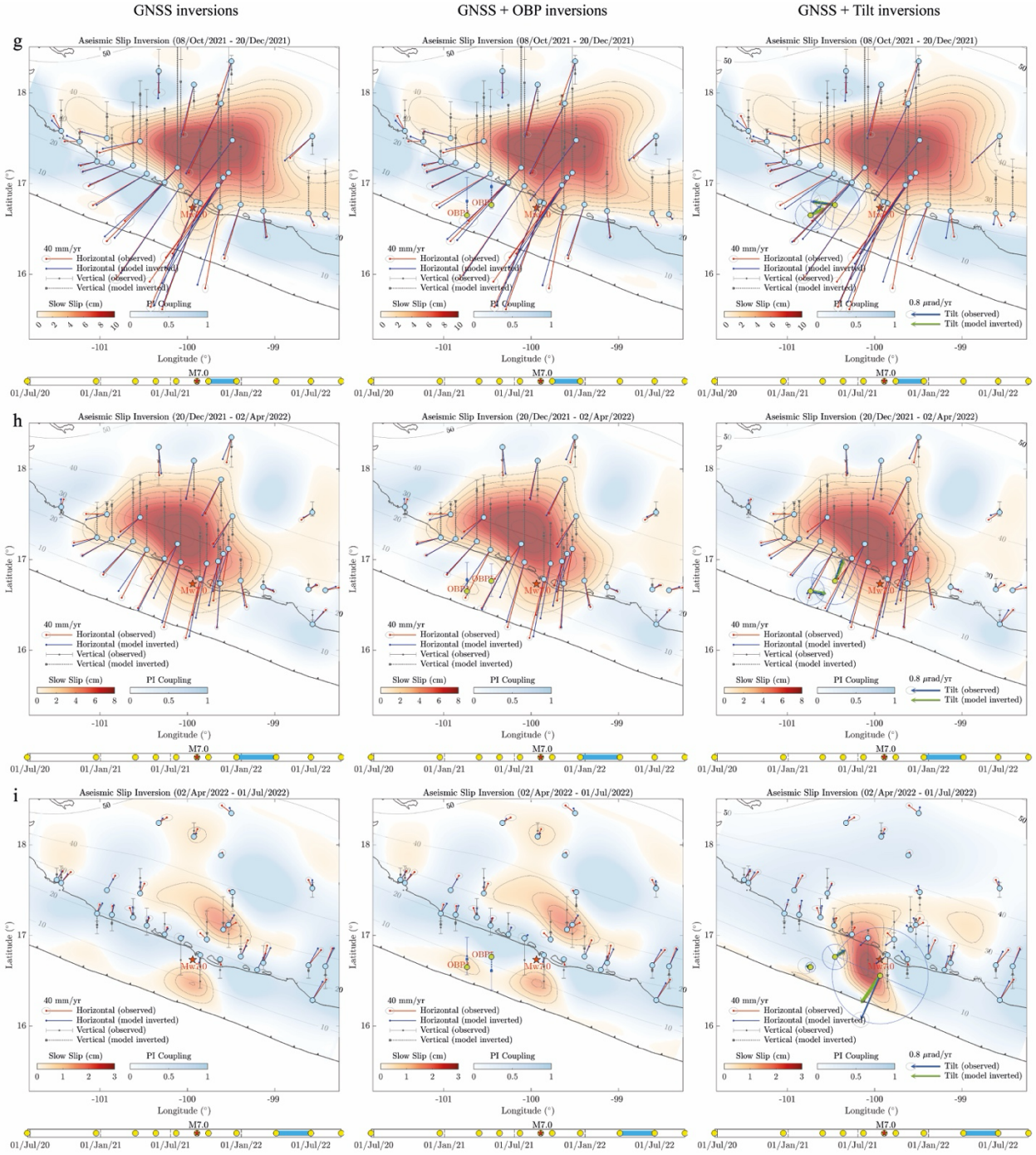

Fig. S19. (continue)

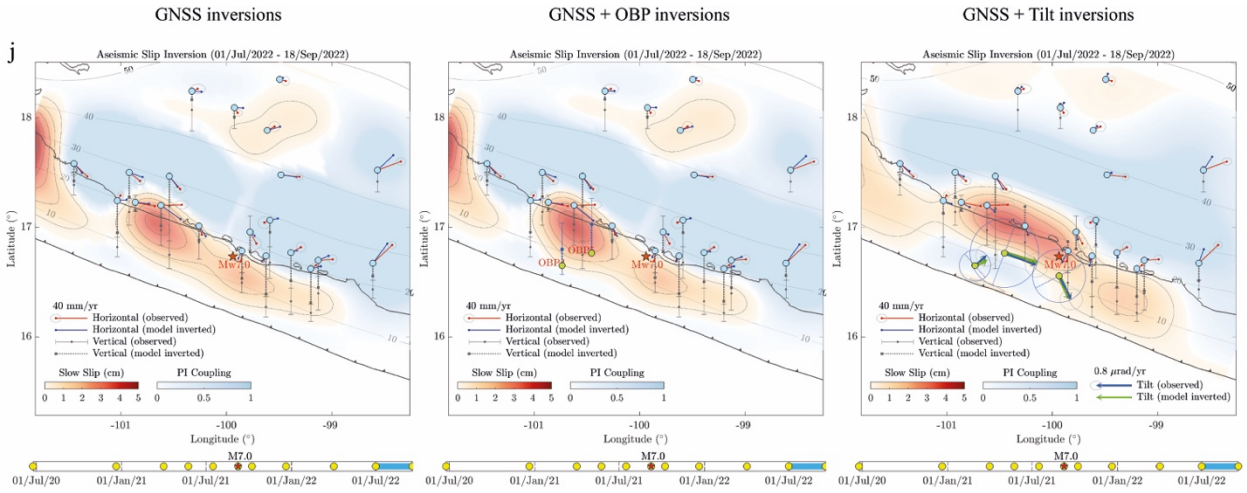

Fig. S19. (continue)

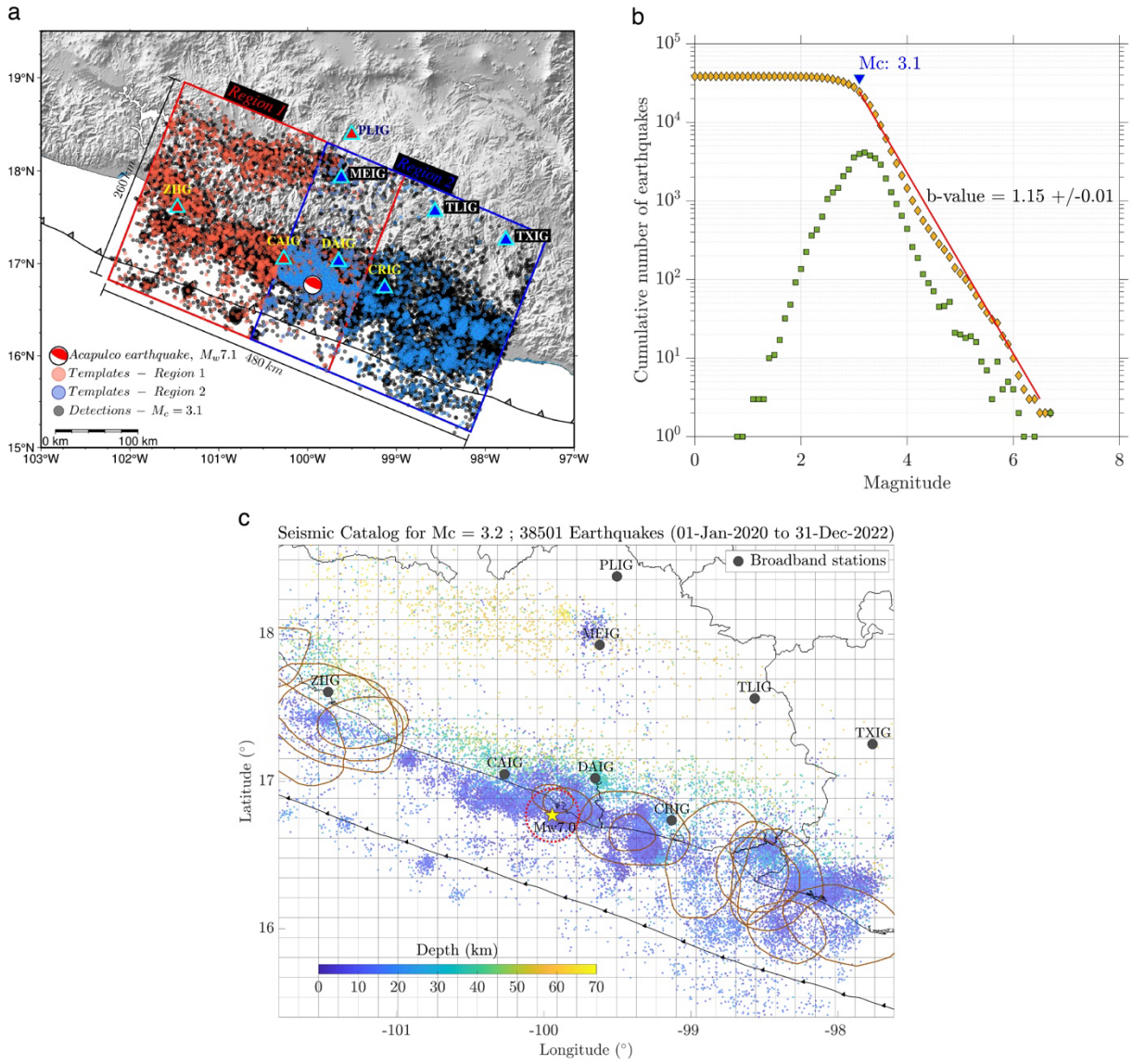

Fig. S20. Template matching seismic catalog (a), completeness magnitude Mc (b) and spatial discretization of the catalog (c). The catalog has 38,501 events above Mc for the 3 years period analyzed (panel c). Broadband seismic stations are indicated in (a) and (c), while the brown shapes in panel c depict the rupture areas of historical earthquakes. The red dotted circle in panel c indicates the 20 km radius region used in the seismicity analysis around the hypocenter of the 2021 Acapulco earthquake (see Fig. 9b).

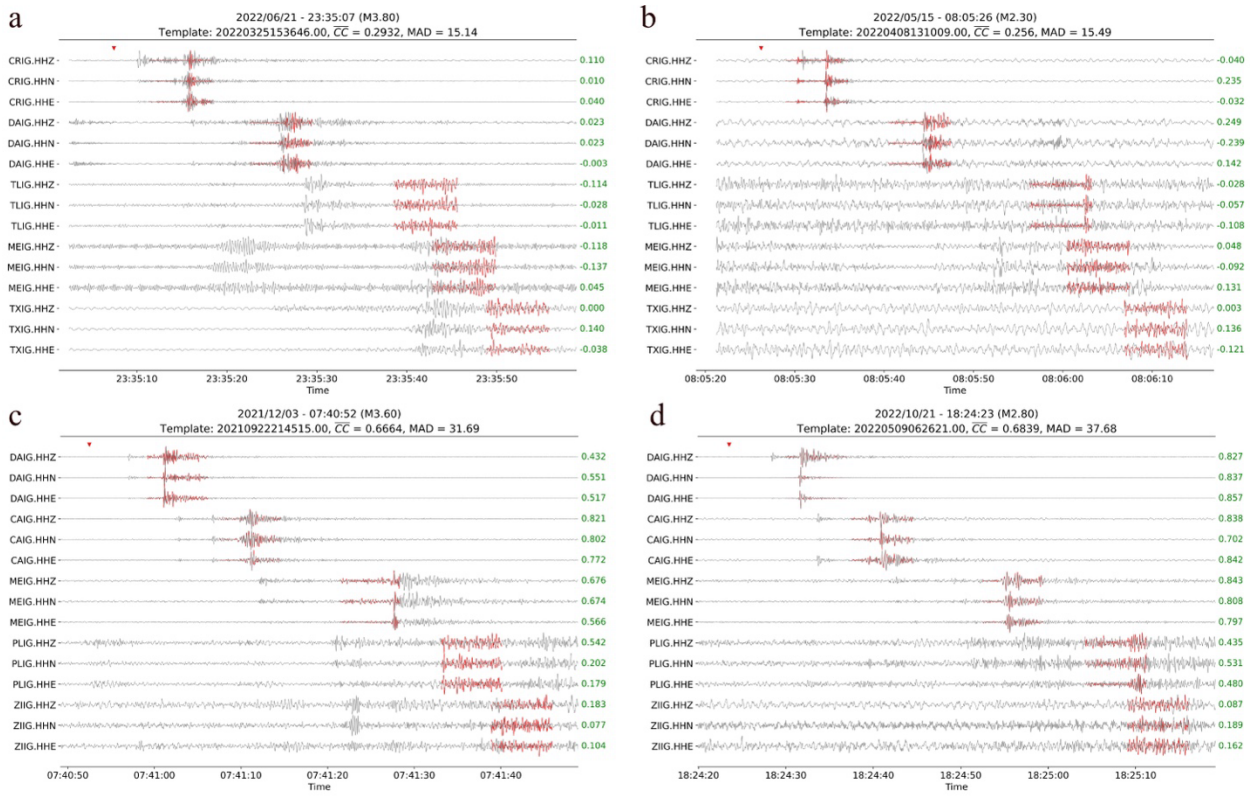

Fig. S21. Examples of template matching detections across a range of MAD values. Panels (a) and (b) show detections near the detection threshold (MAD ≥ 15), while panels (c) and (d) show detections with larger MAD values. Gray traces represent the continuous record, with templates overlaid in red. Green numbers to the right of each plot indicate individual correlation coefficient estimates.

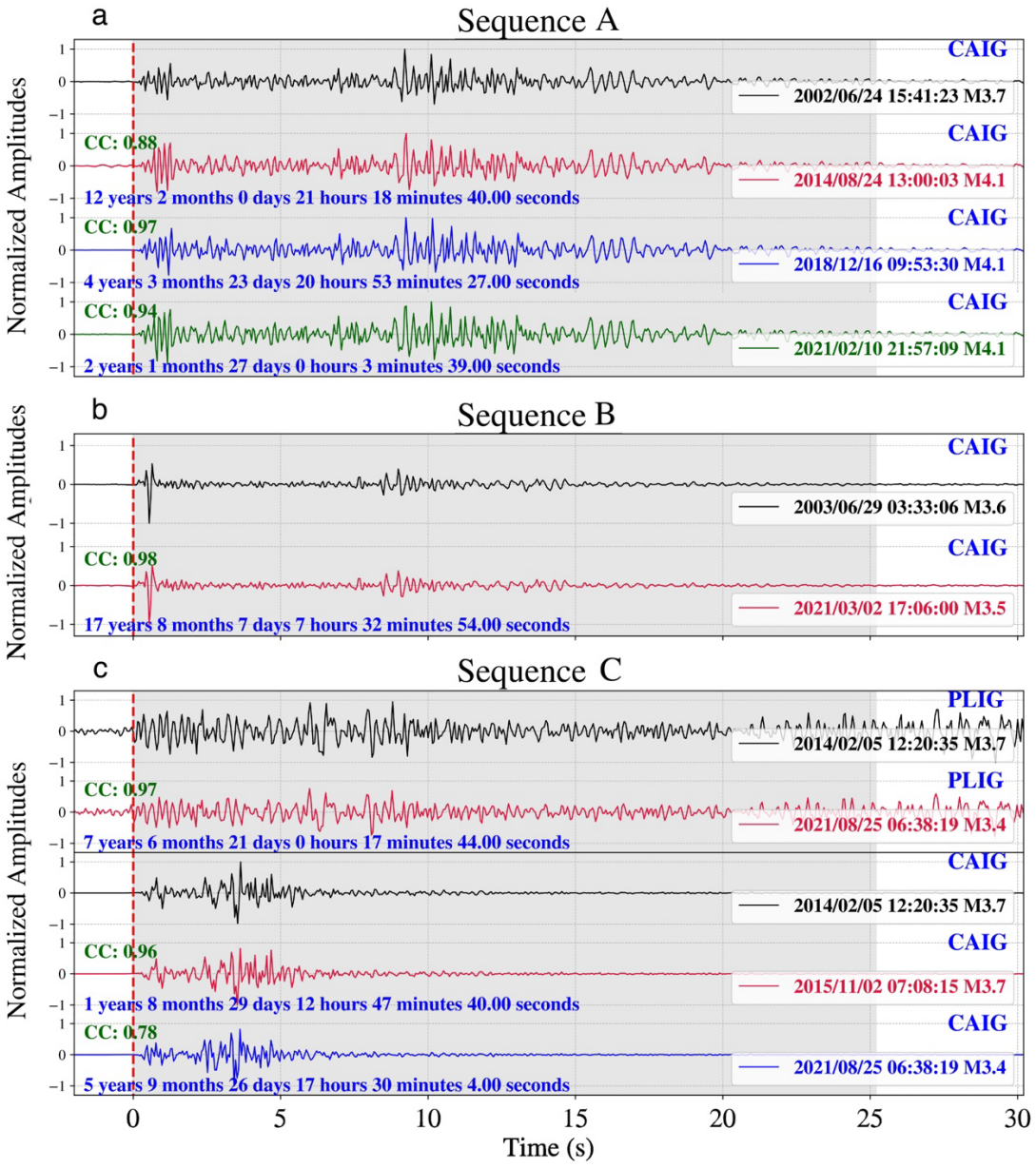

Fig. S22. Example waveforms for repeating earthquakes activated during the pre-seismic offshore SSE. (a and b) Sequences detected at the initial phase of the SSE near the trench identified only at the CAIG station. (c) One of the sequences activated weeks prior to the Acapulco earthquake where the SSE gained strength close to the shoreline, detected by stations PLIG and CAIG. The inter-event time between adjacent detections is shown in blue text, and the correlation coefficient for each pair with the first event in the sequence is shown in green text. All waveforms are filtered using a bandpass Butterworth filter from 1–8 Hz for the vertical component, and the amplitudes have been normalized to the maximum values of each trace. The gray shaded area indicates the time window where the correlation coefficient is computed. The location of each sequence is shown in panel b of Figure 9.

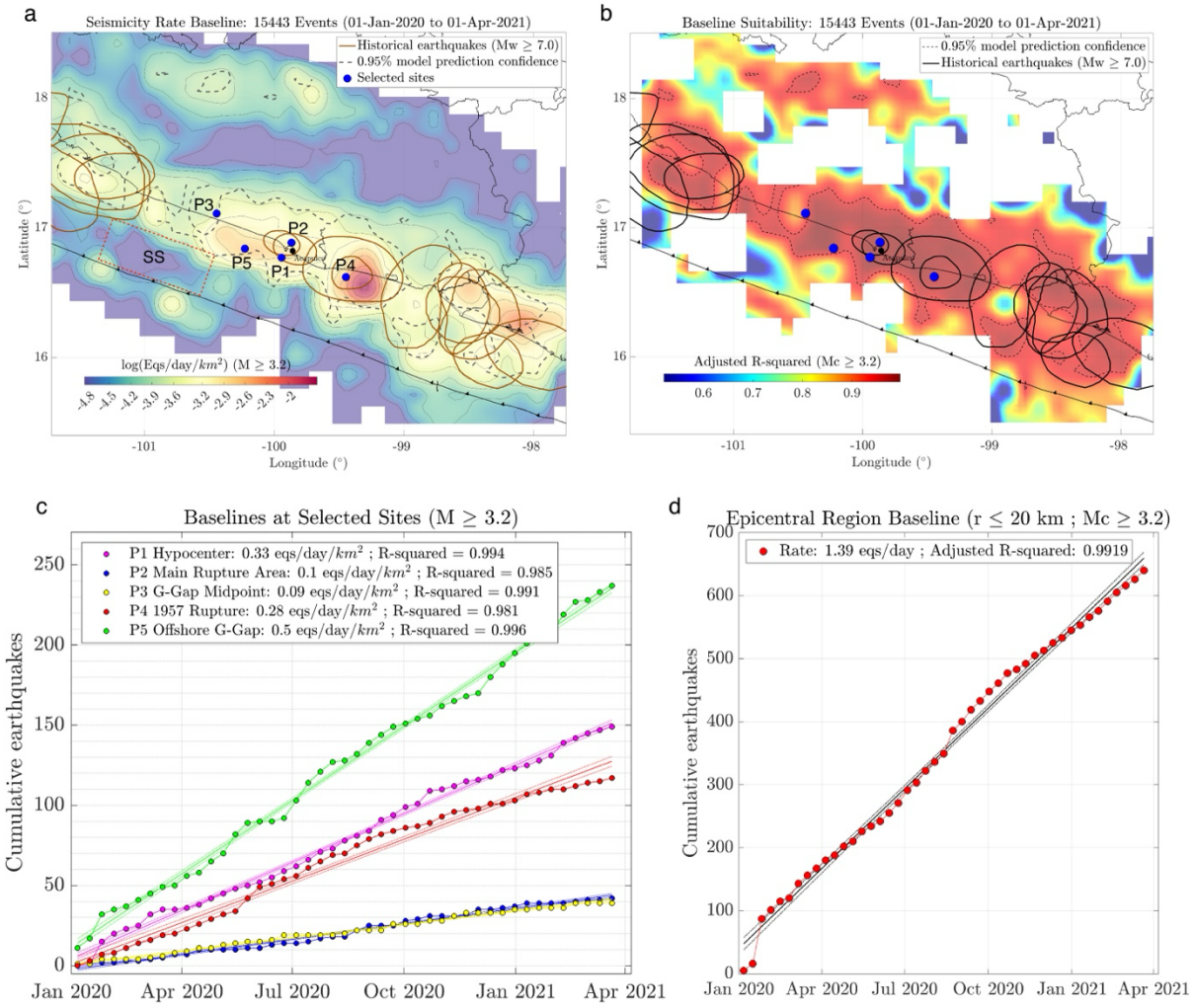

Fig. S23. Seismicity baseline and baseline confidence. (a) Seismicity baseline for the 1.3 year period indicated in the heading, preceding the period in which tectonic activity was identified from geodetic data. The baseline was determined from linear regressions within the geographical bins shown in Fig. S22c. Baseline values were interpolated to a regular 5 km grid. (b) Adjusted R-squared estimates for the baseline regressions. The dashed contour delineates the region with 95% regression confidence. (c) Plots of the linear model compared to the data at five selected sites (see panel a). (d) Cumulative earthquakes within a 20 km radius around the hypocenter of the Acapulco earthquake along with a regression of the linear model.

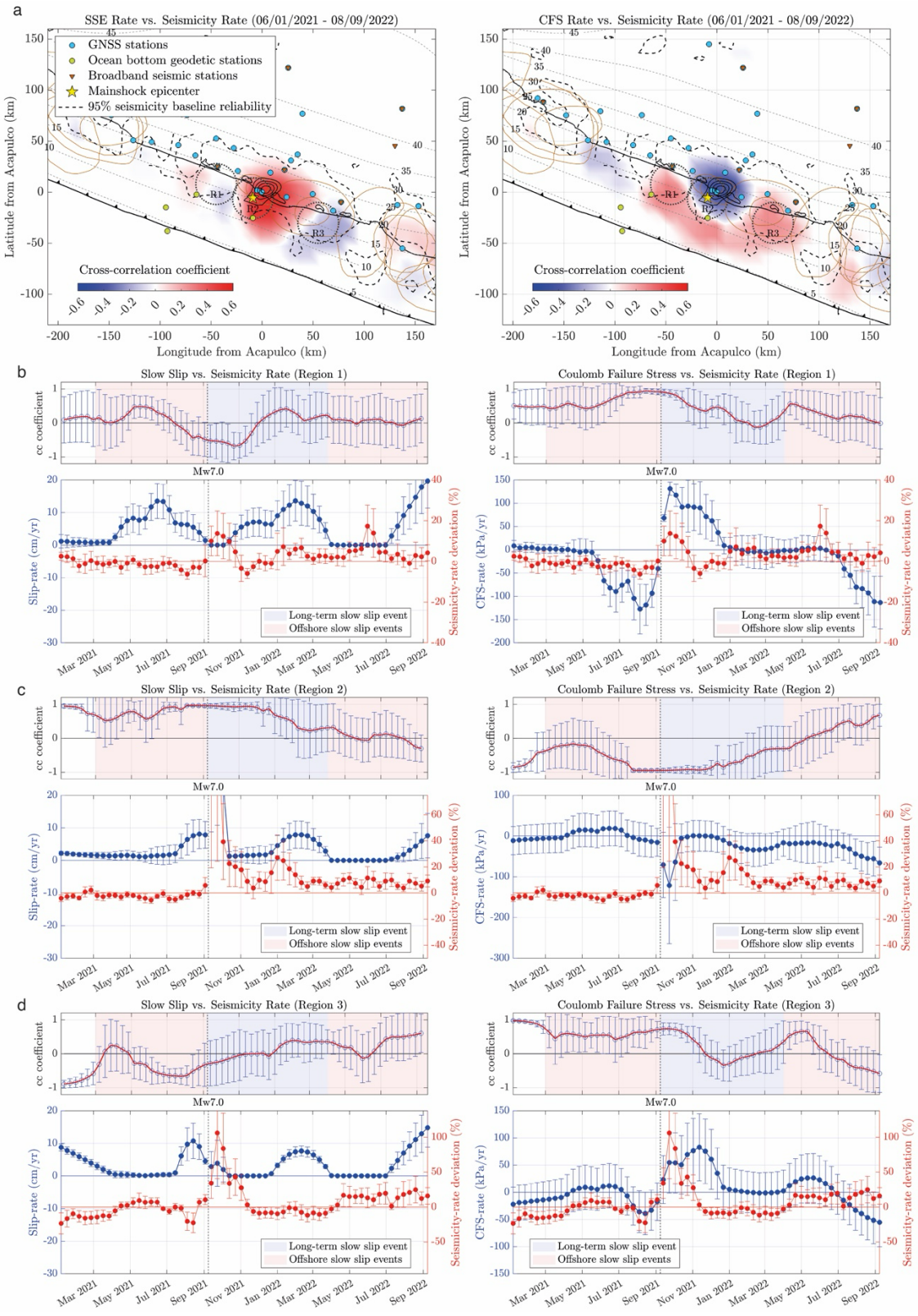

Fig. S24. Correlation analysis between the seismicity rate and both, slip rate (left column) and Coulomb failure stress (CFS, right column) at the plate interface. (a) Average over 1.3 years (see heading dates) around the 2021 Acapulco earthquake of the cross-correlation coefficient (cc)

between the seismicity rate and both, slip rate and CFS. (b-d) Comparison of seismicity rate deviation from baseline and both, slip rate and CFS (bottom panels) in the three 20-km radius regions shown in panel a. Upper panels show cc as a function of time, estimated from wavelet decomposition of time series (Cooper & Cowan, 2008).

Fetch Unit Attribute	Value
Legs aperture (L)	1.0 m
Unit high (h)	0.615 m
Glass sphere mass	47 Kg
Glass sphere buoyancy	-588.6 Nw
Tripod mass	60 Kg
Tripod foot surface	0.108 m^2
Tripod buoyancy (assumed 10%)	-58.9 Nw
Glass sphere net weight (in water)	-127.5 Nw
Tripod net weight (in water)	529.7 Nw
Fetch Unit net weight (in water) (W)	402.2 Nw

Table S1. Physical attributes of one Fetch Unit after Sonardyne Fetch Transponder User Manual, 2020. See Figs. 5 and S10.

Tiltmeter	Observed (μrad/yr)		Model (μrad/yr)		Amplification Factor (A_t)
	P_l	P_{lp}	P_l	P_{lp}	
OBT4	-15.00	-39.23	0.240	-0.048	1275.3
OBT5	544.14	-20.22	0.390	-0.173	1275.3
OBT7	-405.84	-105.45	-0.494^{+}	0.0	848.9
OBT8	2333.99	73.62	0.393	-0.101	5756.8

Table S2. Observed (before amplification correction) and theoretical inter-SSE tilt rates along the plate convergence (P_l) and its perpendicular direction (P_{lp}). Amplification factors correspond to the quotient of the observed and theoretical tilts except for OBT4, where we assumed the same factor as for OBT5 (see main text). $^{+}$Theoretical estimate at OBT7 (Cocos plate) was done independently by Kosotglodov et al. (2024). The other predictions correspond to the inter-SSE coupling inversion shown in Fig. 6.

Movie S1.

Slow slip evolution at the plate interface every 10 days from the interpolation of the joint inversions of onshore GNSS and offshore OBP and tilt data for the 10 windows shown in Fig. S18.

Movie S2.

Deviations of the seismicity rate from the baseline as a function of time for steps of 10 days. Green contours depict the slow slip evolution (1 cm increments) in the plate interface, while red stars show the repeating earthquakes occurred $\pm$10 days around the current window.